The Pennsylvania State University
The Graduate School
College of Engineering

FLOW AND SEDIMENT TRANSPORT IN NATURE-BASED SOLUTIONS FOR RIVER RESTORATION

A Dissertation in
Civil Engineering
by
Seyedeh Azadeh Mousavi Darzikolaei

Submitted in Partial Fulfillment
of the Requirements
for the Degree of

Doctor of Philosophy

December 2024

The dissertation of Seyedeh Azadeh Mousavi Darzikolaei was reviewed and approved by the following:

Xiaofeng Liu
Associate Professor of Civil and Environmental Engineering
Dissertation Advisor
Chair of Committee

Roberto Fernández
Assistant Professor of Civil and Environmental Engineering

Xiang Yang
Assistant Professor of Mechanical Engineering

Anastasia Piliouras
Assistant Professor of Geosciences

Abstract

This dissertation investigates the hydrodynamic and sediment transport processes around nature-based river restoration structures, with a focus on engineered log jams (ELJs) and large woody debris (LWDs). Although adding wood to rivers is a popular practice to mimic Nature, most designs have been based on experience rather than a thorough understanding of their impact on flow dynamics and sediment transport.

Scour, a stability-threatening process around in-stream structures, also contributes significantly to their ecological benefits. While it has mostly been studied for solid, simple geometric structures like bridge piers, it is essential to investigate scour around nature-based solutions (NBS) to ensure that river restoration projects achieve their objectives. This research addresses this gap by analyzing the complex interactions between porous, geometrically complex structures and their environment, focusing on both hydrodynamics and morphodynamics.

The primary hypothesis of this work is that the porosity and shape complexity of these structures are key factors controlling sediment transport. This hypothesis is explored through a combination of flume experiments and high-fidelity computational fluid dynamics (CFD) simulations. The aim is to uncover the fundamental physical processes that occur around and within these NBSs and to develop a quantitative framework for predicting sediment transport and scour in river restoration.

Understanding the mechanisms of scour requires a thorough investigation of turbulent flow dynamics, bathymetric features, wall shear stress, and precise quantification of these factors. By quantifying these physical processes around complex porous in-stream structures, appropriate equations for predicting maximum scour depth and its temporal evolution are developed.

This work is organized into four main parts. First, flume experiments were conducted to study the flow and sediment transport around engineered log jams (ELJs) with varying porosities and placements. These experiments provided detailed measurements of flow patterns, scour depth, and sediment transport, which were used to derive new equations for estimating scour depth. Specifically, modifications were made to existing solid structure equations to account for the effect of porosity. The experiments also introduced two definitions of porosity, i.e., surface and volumetric porosities, in a accurate general formula for equilibrium scour depth. The findings were validated against real-world river restoration projects, ensuring their practical relevance.

The second part of this work focuses on high-fidelity computational fluid dynamics (CFD) simulations to investigate the coupled flow and sediment transport processes around ELJs. The simulations emphasized the quantification of flow characteristics, particularly

turbulent flow patterns and bleeding flow through porous structures. Using the immersed boundary method, the model provided detailed insights into flow contraction, vortex formation, and velocity profiles. These simulations helped reveal how porosity alters the hydrodynamic behavior around the structures, offering a more thorough understanding of the differences between porous and solid structures.

The third part extends the CFD simulations to emphasize the quantification of wall shear stress, scour depth, and sediment transport rate around porous and solid ELJs. These simulations enabled the development of a semi-theoretical model for predicting the temporal evolution of scour depth, incorporating porosity as a key factor. The model integrates physical processes such as bed shear stress distribution and sediment transport dynamics, offering a more generalized and accurate prediction tool than previous models purely based on empirical data fitting.

The final part focuses on experiments and simulations of large wood structures with porous rootwads, capturing the flow and sediment transport around these complex geometries. The experiments were conducted to shed light on the differences in flow and equilibrium bathymetric patterns around a log with a rootwad and a single cylindrical log. Previous studies often simplified LWDs to simplified shapes like cylinders or blocks, missing their true complexity. Hence, this research also examines how much geometric detail is needed for accurate simulations of in-stream structures, comparing fully resolved, solid, and porous rootwad models to assess their effects on flow dynamics, sediment transport, and the temporal evolution of these processes

Table of Contents

List of Figures

List of Tables

Acknowledgments

First and foremost, I would like to thank my supervisor, Dr. Xiaofeng Liu for giving me the opportunity to work on this project, as well as for his mentorship, guidance, and support throughout these years. I express my deepest gratitude to him for his invaluable contributions during my PhD. His expertise and ideas have greatly expanded my scientific understanding and enhanced my practical skills in hydraulic modeling and analysis. I am truly thankful for his involvement, patience, encouragement, and the opportunities and flexibility he provided.

I am deeply grateful to my PhD committee members, Dr. Anastasia Piliouras, Dr. Xiang Yang, and Dr. Roberto Fernández, for their valuable feedback and support. I learned from each interaction with them, and their expertise and insights greatly improved my work.

I would also like to thank the researchers at Turner-Fairbank Highway Research Center at FHWA and Genex Systems for the internship opportunities to work on a national-scale project. Special thanks to Drs. Kornel Kerenyi and Hoayin Shan for providing me with the opportunity and their guidance.

I am thankful to Dr. Farshad Rajabipour, Dr. Shihui Shen, Dr. Xiaofeng Liu, and other collaborators on a side project for offering me valuable perspectives and insights on other areas of civil engineering.

I am grateful to my lab and group members at Penn State: Hassan, Yalan, Bing, Xi-Yuan, Fikri, Yilan, and Alejandro. I would like to extend my thanks to Dr. Hassan Ismail for his guidance in using the flume and conducting experiments at the hydraulics lab. A special thank you to Yalan Song for sharing her CFD modeling expertise and for being a supportive presence. I also want to thank my WRE friends as well as others from the Sackett Building and EcoRe Building. I would like to thank the WRE and Environmental professors for creating a supportive, collaborative, and friendly environment.

I am grateful to the faculty of the Civil Engineering department, as well as the administrative and IT staff, for their invaluable support throughout my PhD journey. I also appreciate the ICDS HPC resources, which enabled me to carry out my numerical simulations. Additionally, I extend my thanks to the CITEL lab team for their assistance in building my lab models.

I would also like to thank American Society of Civil Engineers (ASCE) for selecting me as the J. Waldo Fellowship recipient, which allowed me to conduct my research on LWD applications. This recognition encouraged me to explore my passion for nature,

physics, and hydraulics.

I am grateful to the National Science Foundation for supporting this work through Award #1935243.

A heartfelt thanks to everyone I've met along the way, whose encouragement, willingness to share knowledge, and support helped me keep moving forward.

Last but not least, I would like to thank my Family: I would like to thank my husband, Mohammad Moeini, for his unwavering support and patience throughout my PhD journey. I am grateful to him for standing by me through the hard times, celebrating every achievement with me, encouraging me every step of the way, and believing in me.

I am deeply grateful to my parents and brothers for their emotional support, teaching me resilience, responsibility, and a passion for learning. My heartfelt thanks also go to my grandparents for their kindness and wisdom, and to my in-laws for their constant kindness and positivity throughout this journey.

Chapter 1 Introduction

1.1 Motivations and Methodology

1.1.1 Background and Motivations

Nature-based in-stream structures are integral to river restoration practices. These structures are designed to restore rivers' natural functionalities. The physical and ecological benefits provided by the large wood structures have made them a preferred choice in nature-based solutions (NBS) [Wohl et al., 2019, Shields Jr and Nunnally, 1984, USBR and ERDC, 2016]. Naturally formed examples include large woody debris (LWD), which can be composed of fallen trees, logs, stumps, root wads, and branches. Engineered structures, such as engineered log jams (ELJs), mimic natural formations such as LWD. Despite the popularity of using large woods in river restoration practices, there are still knowledge gaps on how they work, what restoration goals they can achieve, how to ensure their longevity, and how to maximize their benefits [Bernhardt et al., 2005, Doyle et al., 2007, Lepori et al., 2005].

Understanding erosion around in-stream structures is crucial, as it can undermine structural stability and lead to significant repair costs, as seen in cases of bridge failures [Coleman et al., 2003]. Scour, one of the most critical consequences of sediment transport around in-stream structures, can be classified into several major types: general scour, contraction scour, and local scour [Wang et al., 2017, Richardson and Richardson, 2008]. The latter two are closely associated with three-dimensional turbulent flow features. Therefore, when studying erosion, it is essential to consider the interaction between sediment transport and flow dynamics.

The complexity and porosity of LWDs and ELJs lead to unique physical changes in rivers and streams processes, influencing both flow dynamics and erosion. These changes,

in turn, affect various aspects of riverine ecosystems. The resulting hydrodynamics alterations, such as turbulence and flow acceleration around these structures, impact fish swimming abilities, energy expenditure, habitat selection, and foraging behavior [Tullos and Walter, 2015, Gorman and Karr, 1978, Palmer et al., 2010]. Additionally, they cause flow obstruction and scour pool formation, which are crucial for habitat diversity. The deeper water in scour regions, characterized by lower temperatures and reduced velocities, creates favorable conditions for many aquatic species [Abbe et al., 2003].

The main flow features around a solid structure have been comprehensively investigated. These features include several distinct phenomena, such as flow acceleration along the sides of the structure, known as contraction velocity, downward flow in the upstream region, referred to as downflow, and sweeping flow, which varies depending on the structure's submergence level. Flow can also recirculate in the wake region, with shear layers forming along the sides. Each of these flow features can result in vortical structures, such as horseshoe vortices and wake eddies. These flow dynamics introduce turbulence and shear stress on the bed, leading to erosion when they exceed a critical threshold. The erosion pattern is affected by the specific flow formations, which influence the depth, shape, and distribution of scour and deposition [Melville and Dongol, 1992, Arneson et al., 2012b, Khosronejad et al., 2012, Wang et al., 2017].

The key question in this thesis work is: how do these aforementioned flow features change when structures like engineered log jams (ELJs) and large woody debris (LWDs) are porous and geometrically complex? This porosity allows part of the flow to pass through the structure, rather than being re-directed around it. Studies have shown that even adding simple surface openings to hollow piers, which allow flow to enter the structure, significantly reduces local sediment transport and the maximum scour depth around the structure [Yang et al., 2021]. How would these effects evolve with more complex geometries, such as LWDs with varying roughness elements and complex geometry and internal structures? What would be the outcome of the flow interaction with irregular surfaces and shapes? Would this interaction introduce additional turbulence and flow separation in multiple directions, leading to more complex changes in sediment transport and scour patterns?

Porosity is a common characteristic of nature-based river restoration structures made from large wood or other natural materials, such as vegetation. Numerous studies have been conducted to understand flow and sediment transport around vegetation. However, in most of these studies, porosity was fixed in the vertical direction, which differs from the complex formation of large wood structures. Porosity plays a crucial role in vegetation

flows, primarily due to the bleeding flow through pore spaces, which influences the flow field, turbulence, shear stress, and ultimately the bathymetry. Previous vegetation flow studies showed that interstitial flow through pore spaces creates diverse hydraulic conditions, helps trap and decay pollutants, and reduces geomorphic impacts on fluvial systems [Chen et al., 2012, Aberle and Järvelä, 2013, Nepf, 2012, Zong and Nepf, 2012].

Although some studies have explored the effects of logjams and woody debris on flow and sediment transport through physical and numerical models [Gallisdorfer et al., 2014], no general guideline exists for quantifying river responses, such as scour depth, while accounting for porosity. Often, the scour is estimated using the Federal Highway Administration's Hydraulic Engineering Circular-18 (FHWA HEC-18) [Arneson et al., 2012b], which is designed for solid piers and does not account for porosity. The lack of a standardized approach leads to significant uncertainties in engineering practice. Since, current designs often rely on simplified models that fail to capture the complex hydraulic and bathymetric features of natural in-stream structures.

As the riverbed evolves, so do the processes driving its evolution [Schalko and Nepf, 2024], and a fixed bed does not represent this dynamic process. Some studies have attempted to understand sediment transport by focusing solely on flow dynamics [Schalko et al., 2021b, Koken and Constantinescu, 2014]. These studies are useful for understanding the initiation of sediment transport processes, but they do not fully address the evolution and equilibrium conditions. Thus there is a lack of research that quantitatively investigates the concurrent interplay between flow and sediment.

Another area that requires more attention is the realistic representation of nature-based solutions (NBS) structures. Most previous studies have focused on simplified cylindrical solid shapes [Schalko et al., 2021b, Wilcox et al., 2006], which do not capture the full complexity of natural structures. For example, researches have indicated that the rootwad of a fallen tree plays a significant role in altering both flow and sediment dynamics. In riparian environments, fallen trees along the bank can contribute to both bank erosion and bank protection, depending on the circumstances. In general, the rootwad increases flow blockage, creates local scour underneath, and may also shield the bank. However, the turbulent flow and sediment transport around LWD with a rootwad have not been thoroughly investigated [Zhang et al., 2020c,b, Ravazzolo et al., 2022].

1.1.2 Flume Experiments

Flume experiments around in-stream structures with erodible beds are highly valuable in understanding key flow features, such as reduced velocity regions, turbulent zones, shear

layer extents, and downstream recirculation. Additionally, they help capture bathymetric details at equilibrium, including the maximum scour dimensions, the shape of scour holes, and deposition bars. Capturing these features also provides valuable data for validating numerical models. While computational models can be cost-effective with proper validation, they have not been thoroughly tested for accuracy around complex woody structures in rivers. Therefore, comparing CFD models with ground truth data from controlled experiments is essential. Advanced flow measurement techniques, such as Acoustic Doppler Velocimeters (ADVs) [Nikora and Goring, 1998], have been used to measure three-dimensional (3D) flow velocities in turbulent flows, providing key data on mean velocity, Reynolds stresses, shear stresses, and turbulent kinetic energy in applications of open channel flow [Ferro, 2003, García et al., 2005, Duan et al., 2009, Acharya, 2011, Papanicolaou et al., 2001].

To validate coupled flow and sediment transport around in-stream structures at equilibrium condition, flume experiments must be well-structured and run long enough to capture the equilibrium scour depth, as bathymetry evolution is a very slow process. Velocity measurements and bathymetric features should be recorded at equilibrium for effective CFD validation. Equilibrium condition is defined as the time when changes in sediment transport become negligible. Data collected from experiments that reach equilibrium is also essential for developing useful scour depth equations.

However, few experimental studies have explored a variety of conditions for complex in-stream NBSs that include erodible bed. In the case of porous ELJs, Ismail et al. [2021] compared solid and porous ELJs made of stacked dowels, finding significant differences in flow and bathymetry. They developed a correction factor to relate the scour depth of porous structures to that of solid ones. However, further research is needed to account for the range of porosities found in natural ELJs and large woody debris (LWDs). Additionally, porous rootwads, often present in large wood structures, have yet to be studied.

One of the key challenges in flume experiments is capturing accurate velocity data near an evolving bed without interfering with the erosion process. In addition, conducting point measurements like Acoustic Doppler Velocimeters (ADV) is time-consuming, and it becomes particularly difficult to measure and visualize the flow field inside and very close to porous restoration structures. However, these near-bed and near-structure information are critical for understanding the underlying processes and are essential for developing more accurate scour estimation equations. They play a key role in calculating wall shear stress, a driving factor in the erosion process. Utilizing computational modeling

extensively validated with laboratory experiments can help us investigate the effects of internal flow through porous structures on flow and sediment transport around complex shapes. This approach overcomes the limitations of relying solely on engineering experience to assess flow and sediment transport in nature-based solutions (NBS) for river restoration.

1.1.3 Computational Modeling Studies

Modeling approaches vary significantly in their ability to capture the complexity of flow. One-dimensional (1D) models, such as the PHABSIM habitat assessment model [Waddle, 2001], simplify hydraulics but cannot capture localized flow features. In contrast, two-dimensional (2D) models, such as the one in He et al. [2009], attempted to model the effect of in-stream structures on channel morphology by including porosity as a resistance force in the porous zone. Fluvial processes around in-stream woody structure and ELJs are mostly modeled in two-dimensions (2D) in previous studies [Bennett et al., 2008, L'Hommedieu et al., 2020]. Nevertheless, such models are not able to capture details in 3D since they are depth-averaged and assume hydrostatic pressure distribution. Another significant assumption in these 2D models is that the vertical flow velocity is negligible, which is not true near structures. As a result, the value of these models for capturing complex 3D flows around in-stream structures is limited.

Scour is a three-dimensional process even around simple cylindrical piles and piers and is even more complex around complex woody materials. It is imperative to use a 3D model to compute scour because vertical fluid motion is very prominent near structures and is a primary contributor to the local scour. Three-dimensional models, such as that in Smith et al. [2011], examined the hydrodynamics around complex LWD structures but did not consider morphological changes.

The widespread application of 3D high-resolution computational modeling in hydraulic engineering has been made possible by advancements in computing power and algorithms. These models are particularly suited for problems involving detailed local flows, such as flow and scour around LWDs and ELJs. By coupling flow and sediment transport, these methods offer valuable insights into flow and erosion dynamics that are difficult to capture through experiments and field measurements.

In 3D computational fluid dynamics (CFD) models, the governing Navier-Stokes (N-S) equations for flow are commonly solved with different numerical methods. For practical purposes, the turbulence is usually captured with the Reynolds-averaged N-S equations (RANS) or large eddy simulations (LES) approaches. With RANS, no turbulent eddies

are resolved. Instead, all are modeled. With LES, eddies greater than the local grid scale are resolved [Kang and Sotiropoulos, 2015a], which can give more detailed flow features and dynamics. However, while LES offers greater accuracy in modeling turbulent flow, its high computational cost, combined with the long and slow nature of processes like scour, makes it impractical. For this reason, RANS is often preferred for practical applications involving erodible beds due to its efficiency in handling complex flows over extended periods.

Extensive numerical studies have been done on formation or suppression of von Karman vortex street around porous in-stream structures such as porous rectangular cylinder, porous disks, and square porous pile at low to moderate Reynolds numbers [Jue, 2004, Ledda et al., 2018]. For instance, a study of flow around porous disks showed that the vortex street occurs close to the structures if the disk's permeability is low. If the porosity is intermediate, the recirculation zone occurs further down the disk, whereas in the case of highly porous disks there is no recirculation zone [Cummins et al., 2017]. However, the range of Reynolds number in such studies on porous structures are at low to moderate values which is different than the highly turbulent flows in rivers and streams.

Many previous studies have simplified the geometry of LWDs and ELJs as simple cylinders or solid blocks, as shown in works by Allen and Smith [2012], Lai and Tullos [2014], and Reichl et al. [2005]. Numerical studies on groynes, which often lack vertical variation in geometry, revealed three-dimensional flow structures in both emergent and submerged configurations, with submerged cases showing more complex vortical systems in and around the embayment [McCoy et al., 2006, 2007, 2008]. In the case of groynes, the importance of submergence on flow behavior was well observed. However, the case of ELJs and LWDs is more complex, as they often exhibit submergence variations. For instance, the addition of a rootwad to a submerged log introduces an emergent element, further complicating the flow dynamics. These emergent elements are often porous as well, adding another layer of complexity.

Research into flow around porous structures in rivers is very limited. Koken and Constantinescu [2014], for instance, investigated flow structures inside and around a rectangular array of cylinders using eddy-resolving numerical simulations to examine coherent structures' role in sediment entrainment. However, their study focused solely on hydrodynamics and did not explore the morphological changes. In the study of cross vanes and similar structures, there are also examples of computational research only focused on hydrodynamics [Kang et al., 2011, Kang and Sotiropoulos, 2015a, 2012, 2015b]. In the literature, coupled hydrodynamic and morphodynamic simulations have

been conducted in the application of other scenarios, such as large dunes in meandering streams and J-hook and rock vanes [Khosronejad et al., 2011, 2018, 2015], emphasizing on the importance of integrated approaches to develop effective design guidelines for rock vane structures.

For a 3D model, to accurately calculate sediment transport, it must produce smooth and accurate wall shear stress (WSS) and account for the dynamic interaction between the structure and the erodible bed, which causes dynamic burial or exposure of the structure. Some previous scour models using moving mesh techniques are limited to simple structures and are inadequate for complex structures like LWDs and ELJs [Roulund et al., 2005, Olsen and Kjellesvig, 1998, Liu and García, 2008, Escauriaza and Sotiropoulos, 2011, Jacobsen and Fredsoe, 2014, Baykal et al., 2017]. Similarly, models that only allow vertical bed movement are also insufficient [Escauriaza and Sotiropoulos, 2011, Khosronejad et al., 2012]. A suitable model must dynamically cut and slice the structure geometry through the bed. Efforts have been made to use advanced algorithms such as the immersed boundary method for flow and sediment transport around solid structures in river and coastal regions [Jasak et al., 2007, Liu and García, 2008, **?**]. Their improvements provide smoother wall shear stress calculations and introduce a realistic sand slide algorithm that couples flow and sediment transport computations, effectively addressing the aforementioned challenges.

In this research a high-fidelity 3D model is used to investigate the effects of porosity and geometric complexity on flow and sediment transport. This work utilizes an unstructured mesh and an immersed boundary method which produces smooth wall shear to capture the erosion processes around and within ELJs and LWDs with root wads.

The research goal is to reveal the flow and transport processes around and within porous in-stream structures inspired by nature. Experiments were conducted, and advanced computer models were used to examine the physical processes of flow and scour around complex restoration structures made of large wood in highly turbulent river flows.

The first focus of this research is ono turbulent flow, which behaves uniquely in the presence of porous structures. To determine the wake zone and flow acceleration zone around ELJs and LWDs, the velocity and turbulence were measured and analyzed experimentally and numerically. Based on the results, we identified areas of high turbulence, flow separation, and large wake regions with low velocity, all of which depend on porosity. These flow features and regions are related to sediment transport and the resulting bathymetric features.

The second focus of the research is on sediment dynamics. Scour patterns and scour

depth were analyzed. For practical applications, scour depth is a key for design. Proper scour depth equations were proposed through a comprehensive parametric study using the experimental data. The proposed formula is tested against a rare set of field measurement data on the South Fork of the Nooksack River, Washington. Temporal scour depth equations were also proposed using dimensional analysis of experimental data.

Additionally, a semi-theoretical temporal scour depth equation was proposed based on the physics of the problem and numerical results. The relationship between scour depth and shear decay around porous structures was captured. For the first time, equations estimating the temporal evolution of scour depth around porous in-stream structures were introduced. These equations were derived from dimensional analysis of experimental data, along with an additional equation based on the physics and numerical results. The resulted model can be used to assist practitioners in design and assessment of in-stream porous structures.

To achieve the research goal, both flume experiments and computational modeling were conducted. First, flume tests were conducted to study the physical processes. Two series of experiments were conducted in the flume: the first for ELJs and the second for LWDs. In all cases, flow was in a clear-water regime, considering two types of structures (single ELJs and LWDs) and two different placements of structures, either on the side or in the center of the flume, with different porosities and shape complexities.

The second part of the research involves modeling flow and sediment transport. An existing 3D scour model, was used [Song et al., 2022b]. For scour simulations, the RANS $k-\omega$ turbulence model was adopted due to its computational affordability. Overall six simulations were conducted. Two simulations were performed for a porous ELJ and a solid structure. Additionally, four simulations were performed for the LWD application, involving a fully resolved single log, a log with a porous rootwad, and two simplified representations of the rootwad. In one case, the porous rootwad is modeled using a porosity model approach, while in the other, it is represented as a solid cylindrical block. Results were analyzed in depth.

1.2 Research Questions and Objectives

The goal of this study is to develop reliable methods for understanding and estimating the physical processes around nature-based solutions for river restoration. Porosity, turbulent flow and erosion introduce significant complexities that affect hydraulics and restoration practices. Current design methodologies are not well-suited for LWDs and ELJs. This

work aims to address the following scientific questions:

1. What are the impacts of porosity and shape complexity on hydrodynamics and sediment transport around in-stream structures?
2. How much geometric detail should be resolved in computational models of ELJs and LWDs?
3. How can existing equations for solid structures be adapted and improved for application to porous structures?

Addressing the research questions is achieved through the following specific objectives:

1. To quantify the effect of porosity in porous in-stream structures on flow and its impact on morphodynamics:
    - Conduct flume experiments in a hydraulic flume for ELJ and LWD models.
    - Use CFD simulations on both solid and porous structures, validated by experimental flow and bathymetric data.
2. To quantify the sediment transport:
    - Analyze flume experiments to provide equilibrium bathymetry and maximum scour and deposition data at specific observation times.
    - Validate and analyze 3D scour numerical models to capture the full dynamic evolution of the bed.
3. To develop a general equation for estimating maximum scour depth considering porosity:
    - Develop a scale-independent equation for predicting maximum scour depth through dimensional analysis, using experimental and field data considering two types of porosity: bulk (volumetric) porosity and surface porosity.
    - Conduct dimensional and analytical analysis into the relationship between shear decay and scour depth leveraging numerical data to estimate temporal scour rate
4. To assess the impact of geometric simplification on physical processes:

- Conduct hydraulic flume experiments on in-stream structures, comparing simplified logs with porous rootwads on an erodible bed.
- Perform CFD simulations using three approaches to represent the rootwad: fully resolving geometric details, using a porosity model, and modeling as a solid block.
- Evaluate the accuracy of the porosity model and solid block in simulating both flow and sediment transport by comparing them with the fully resolved case and experiment result.

1.3 Dissertation Organization

This dissertation is organized as follows:

- **Chapter 2: Experimental Study on ELJs and Improving Predictive Formulas**

  This chapter details the flume experiments conducted on engineered log jams (ELJs), examining the effects of porosity on mean velocity, turbulence, morphology, and bathymetric features. A correction factor for predicting maximum scour depth, based on porosity, is presented. It also includes a dimensional analysis of temporal scour depth evolution around ELJs.

- **Chapter 3: Computational Modeling of Coupled Flow and Sediment Transport Around ELJs**

  This chapter focuses on computational modeling of coupled flow and sediment transport around ELJs, with an emphasis on methodology, model validation and the analysis of flow structures.

- **Chapter 4: Utilizing CFD Modeling in Scour Prediction**

  This chapter builds on the sediment transport modeling, emphasizing model accuracy and presenting new equations that link shear decay, scour depth, and sediment transport rate. It also introduces a physics-based predictive formula for temporal scour depth that incorporates the effects of porosity.

- **Chapter 5: Flume and CFD Analysis of Porous Rootwads in LWD Applications**

This chapter presents a flume and CFD analysis of the impact of porous rootwads on scour in LWD applications. It includes a comparison of different modeling approaches for representing rootwads.

- **Chapter 6: Summary, Conclusions, and Future Work**

  This chapter provides a summary of the contributions of the research, key conclusions, and suggestions for future work.

Chapter 2
Erosion and Deposition around Porous Engineered Log Jams: Flume Experiments and Improved Predictive Formulas

2.1 Introduction and Literature Review

2.1.1 Overview

Human activities have significantly altered the physical and biological functionalities of rivers and streams on Earth [Bernhardt et al., 2005, Vitousek et al., 1997]. Actions such as removing trees and debris from rivers for flood control [Harmon et al., 1986, Collins et al., 2002, Veatch, 1906, Triska, 1984] have resulted in significant changes to river morphology, the loss of aquatic biodiversity, and the degradation of riparian habitats [Graf, 2001]. To mitigate the negative effects of wood removal on ecosystems and geomorphology, the use of nature-based solutions is gaining popularity in river restoration projects owing to their ecological benefits and cost-effectiveness [Wohl et al., 2019, Shields Jr and Nunnally, 1984, USBR and ERDC, 2016].

Both natural formations, such as large woody debris (LWDs), and engineered solutions, such as engineered log jams (ELJs), offer significant promise for river restoration. Illustrations of different types of Nature-Based Solutions (NBSs) can be found in the Supplemental Materials. A major advantage of ELJs and LWDs in river restoration practices is that they create diverse hydraulic conditions and deep scour pools, which are important for aquatic habitat [Abbe et al., 2003]. ELJs, in particular, have great

potential for river restoration because they are multifunctional. They provide both in-stream engineering benefits, such as stream stabilization [Suaznabar et al., 2021], as well as ecological benefits, such as restoring fish habitat [Brooks et al., 2006].

2.1.2 Background, Knowledge Gaps and Objectives

A key characteristic of LWDs and ELJs is their porosity, leading to complex river responses compared to solid structures. Researches in [Spreitzer et al., 2020a] and [Spreitzer et al., 2020b] on large wood accumulations, employing Structure-from-Motion (SfM) photogrammetry, has demonstrated the feasibility of quantifying porosity in NBSs comprising wooden materials. Their work, which focused on the characterization of accumulation shapes, sizes, and porosities, paves the way for future investigations into how these porosity characteristics influence the physics of flow and sediment transport. In the context of LWDs, [Spreitzer et al., 2021] explored the impact of wood accumulations near piers on hydraulics and sediment transport patterns, providing insights into how spanwise large-wood accumulations influence river dynamics. In the application of ELJs that partially obstuct flow, [Ismail et al., 2021] has reported some exploratory flume work on the effects of porosity on flow and sediment transport around ELJs. This paper reports further research with additional flume experiments to expand the parameter space and improve predictive formulas to better capture the distribution of porosity on the ELJ surface and within the whole volume.

Porous river restoration structures bear some resemblance to vegetation. Studies on turbulent flow in vegetation patches show the importance of porosity on the wake zone length scale as it depends on the spacing of individual stems. The main cause of such dependence is the bleeding flow through pore spaces that affect the flow field, turbulence, shear stress, and consequently the bathymetry [Yagci et al., 2017, Follett and Nepf, 2012, Kim et al., 2015, Waters and Curran, 2016, Chen et al., 2012, Aberle and Järvelä, 2013, Nepf, 2012, Zong and Nepf, 2012]. Studies on vegetation are of paramount importance and have been extensively researched, shedding light on sediment transport and flow dynamics around them. Ismail et al. [2021] highlighted the unique hydrodynamics around porous ELJs compared to cylinder array-like vegetation [Manners et al., 2007, Abbe and Brooks, 2011]. Thus, given the apparent differences in porosity distribution and geometry between vegetation and ELJs, findings from vegetation flow studies cannot be directly extrapolated to ELJs.

The scour of bed materials around in-stream structures plays an important role for creating deep pools and affecting the stability of in-stream structures [USBR and ERDC,

2016]. Hence, understanding the relationship between flow and sediment transport is essential for predicting river responses and ensuring the success of river restoration projects. Erodible bed will evolve as a result of sediment transport induced by the presence of these structures and flow alterations. Flow acceleration, deceleration, and turbulence can entrain or deposit sediment [Cherry and Beschta, 1989, Abbe and Montgomery, 1996, Dixon, 2016, Daniels and Rhoads, 2003]. For instance, Kollmann et al. [1999] noted that LWDs accumulating on gravel bars significantly affect scour and deposition patterns, leading to the formation of pioneer islands.

This study is built upon previous works, yet with very clear distinctions. To show this, a summary of representative hydraulics and sediment transport studies, focusing solely on the presence of large wood in-stream structures, is provided in Table 2.1. An extensive compilation of literature on the physical modeling of large wood (LW) through 2011 can also be found in Gallisdorfer et al. [2014]. For instance, investigations have been carried out on the flow surrounding a single log [Schalko et al., 2021b] or ELJs [Bennett et al., 2015] placed on a fixed bed. While studies on flow provide valuable insights, it is crucial to place ELJs on erodible beds to examine their morphological impact.

Furthermore, other studies on wood barriers and porous piles shows the importance of porosity in flow and sediment transport. The blockage ratio in channels, influenced by wood leaky barriers, significantly affects flood attenuation and backwater rise [Muhawenimana et al., 2021]. A study on square hollow piles revealed that increased surface porosity reduced sediment transport and scour depth [Yang et al., 2021]. Other research has taken a closer look at the morphodynamic aspects of LWDs. For example, Wallerstein et al. [2001] utilized a hydraulic model to assess the effects of large woody debris (LWD) on a sand bed, and Schalko et al. [2019a] examined the local scouring induced by spanwise LW accumulations. The latter research recommends a specific scour equation for scenarios involving spanwise LW accumulations like those found in fully blocked river cross sections. However, they did not recommend its use for situations of partial channel blockage, such as bridge pier scour. Consequently, their equation is not suitable for partial ELJ scenarios, as studied in this research.

ELJs, with their distinct geometric complexity characterized by large anchored key pieces and internally racked wood that partially obstructs flow, differ from vegetation and spanwise LWDs [Addy and Wilkinson, 2016, Abbe, 2006, Xu and Liu, 2017, Manners et al., 2007, Abbe and Brooks, 2011, Ismail et al., 2021]. This is the main differentiation point between this work and most previous researches.

Although the design of ELJs in this study is idealized, it holds real-world values.

It aligns with the designs of apex ELJs, bar apex ELJs, and bank-attached deflector jam configurations, as evidenced by Abbe et al. [2018], Addy and Wilkinson [2016], Brooks et al. [2006], and Bennett et al. [2015]. The ELJs utilized in this study are also similar to those applied in practical scenarios for fish habitats, such as Fish Hotels and Pennsylvania Porcupine Cribs [Norris et al., 2021, Clark-Kolaks, 2015]. Their design improves the habitat by offering hiding space for smaller fish from their predators, a feature that distinguishes it from LWD with uniform porosity.

Currently, no comprehensive guidelines exists for assessing river responses to the introduction of ELJs, which can lead to uncertainties in engineering applications. Often, scour equations for nonporous piers or abutments are used when dealing with these porous structures. The effects of porosity are either only considered in the calculation of effective blockage area or not considered at all. Ismail et al. [2021] reported the recommended equations in HEC-18 (Hydraulic Engineering Circular No. 18) for solid pier scour and in NCHRP 24-20 (National Cooperative Highway Research Program) for abutment scour under clear-water conditions [Arneson et al., 2012a] are inadequate for estimating scour depths for porous structures.

The primary aim of this study is to further examine the turbulent flow unique to the presence of porous structures and to predict areas of sediment transport. We seek to identify areas of high turbulence, flow separation, and the wake regions with low velocity. The second focus is the sediment dynamics. Scour pattern and scour depth are analyzed. For practical purpose, an improved scour depth equation is proposed through a comprehensive parametric study. In ELJs, two types of porosity exist: volumetric porosity, and surface or frontal porosity. We show that it is necessary to consider both surface and volumetric porosities. Existing scour depth formulas for solid structures are amended to include the effects of porosity. To address the reliance on specific idealized ELJ configurations and placements mentioned in this paper, we utilized data from other literature to develop a more generalized scour estimation method. The proposed formula is tested against a rare set of field measurement data on the South Fork of the Nooksack River, Washington.

In this study, we performed flume experiments on porous ELJ structures within a clear-water scour regime. These structures were positioned either on the side or at the center of the flume. As presented in Table 2.1, there are limited studies on the impacts of porous ELJs on an erodible bed, considering both hydraulics and sediment transport. In this study, we examine ELJs, incorporating two distinct porosity values, thereby extending the scope of porosity ranges addressed in prior research with side and

Table 2.1. Summary of literature on hydrodynamic and morphodynamic interactions with woody river restoration structures

Reference	Structure Type	Phenomena Investigated	Erodible Bed	Porosity	$d_s = f(\underbrace{\text{porosity}^*}_{\text{our focus}}, \ldots)$	Scour time history
Wallerstein et al. [2001]	Partial and SW LWD	Drag and Morphology	Yes	-	-	No
Gallisdorfer et al. [2014]	Partial side ELJs	Drag	Yes	$\phi_v \approx 0.68$ and 0.77	-	No
Bennett et al. [2015]	Partial Side ELJ	Flow and Drag	No	$\phi_v \approx 0.68$ and 0.77	-	No
Gallisdorfer et al. [2016]	Partial Side ELJs	Morphology	Yes	$\phi_v \approx 0.68$ and 0.77	-	No
Schalko et al. [2019a]	SW LWD Accum.	Morphology	Yes	$\phi_v = 0.75$	$f(\phi_v, ...)$	No
Schalko et al. [2019b]	SW LWD Accum.	Backwater rise	Yes	$\phi_v = 0.75$	-	No
Schalko et al. [2021b]	Single log	Flow	No	-		
Muhawenimana et al. [2021]	SW Leaky Barrier	Backwater rise	No	$\phi_s = 0.4$ - 0.8 ($\phi_v = 0.25$ - 0.75)	-	No
Spreitzer et al. [2021]	SW LW Accum. at piers	flow and Morphology	Yes	$\phi_v = 0.65$	-	No
Schalko et al. [2021b]	Single log	Flow	No	-		
Ismail et al. [2021]	Side and center partial ELJs	flow and Morphology	Yes	$\phi_s = 0.29$ ($\phi_v = 0.72$)	$f(\phi_s, ...)$	No
Müller et al. [2021]	SW ELJ	Flow	No	$\phi_v = 0.41$ and 0.70	-	No
Müller et al. [2022]	SW ELJ	Flow	No	$\phi_v = 0.41$-0.70	-	No
This study	Side and center partial ELJ	flow and Morphology	Yes	$\phi_s = 0.15$ and 0.35 ($\phi_v = 0.45$ and 0.85)	$f(\phi_s, \phi_v, ...)$	Yes

V_s : Solid volume, ϕ_s : surface porosity, ϕ_v: Volumetric porosity Accum. : Accumulation, SW: Spanwise, d_s: scour depth
*Solid structures are not included in the porosity column

center placements. We delve deeper into the analysis, including maximum scour depth prediction and ELJs scour time history, which has no existing data in the context of ELJs. Moreover, for the first time, we consider the impact of both volumetric and surface porosities on scour depth.

The rest of the paper is structured as follows. The flume experiment details are introduced in Methodology section. This is followed by presenting the results of mean flow velocity and turbulent kinetic energy. Afterward, the findings on bathymetry are discussed. The discussion then extends to the relationship between bathymetry and flow features. Subsequent sections address the estimation of scour depth and its temporal evolution. Finally, the paper concludes by testing the proposed scour equation with field data.

2.2 Methodology

2.2.1 Laboratory Flume and Experiments

The experiments were conducted in a recirculating hydraulic flume with the dimensions of 15.24 m long, 1.52 m wide and 0.91 m deep (Figure 2.1). The flume bottom was set to be close to horizontal ($S_0 = 0.00075$). The flume is equipped with a pump capable of generating a maximum flow rate of 240 l/s. A reservoir and a flow straightener are located upstream of the flume to guide the incoming flow to the test section. Side walls of the flume are made of glass for visualization. The flume is equipped with an instrument carriage that allows for horizontal, lateral, and vertical measurements.

The experiments were conducted using square column structures designed to mimic idealized engineered log jams (ELJs). These experimental flume ELJs were constructed with a side length of 0.305 m. The ELJs were made from the stacks of wooden dowels with a diameter of 0.0254 m (Figure 2.1). To fix the position of the testing structures, two wooden plates on the top and bottom of the stacked dowels and four vertical dowels at the four corners were used. The vertical dowels were 0.8 m long with a diameter of 0.0254 m. All ELJs were emergent and their height was greater than the flow depth. The x axis is along the streamwise direction with $x = 0$ defined at the upstream edge of ELJs. The y axis is along the spanwise direction and $y = 0$ is defined at the center of the flume.

In experiments, two different placements of ELJs were tested: along the wall (side) and in the middle of the flume (center). The volumetric porosity, ϕ_v, of ELJs was calculated as the ratio of void volume ($V_{Total} - V_{Dowels}$) to the total volume (V_{Total}).

Here, V_{Dowels} is the volume of dowels. The surface porosity, ϕ_s, was calculated as the projected frontal porous area ($A_{Total} - A_{Blocked}$) to total frontal area (A_{Total}) of structures (Figure 2.2). Here, $A_{Blocked}$ is the frontal area blocked by dowels.

Building upon the work of Ismail et al. [2021], who reported four cases using the same flume and setup, this study conducted four additional tests with ELJ's surface porosities at $\phi_s = 0.15$ and 0.35 , across two placement locations (side and middle). Hence, we have conducted our analysis on a more comprehensive dataset with surface porosities ϕ_s of 0 (solid), 0.15, 0.29, and 0.35, with their respective volumetric porosities (ϕ_v) of 0, 0.45, 0.72, and 0.85. According to Manners and Doyle [2008], the porosity estimates for wood jams, taking into account their evolution stages (material infilling) in river streams, vary between $\phi_v = 0.43$ and 0.88. Livers et al. [2020] have also assessed the volumetric porosity for field cases. They found it spans from 0.1 to 0.9 across various types of stream jams, ranging from small in-channel structures to large island apex formations.

The flume bed was covered with poorly graded medium sand. The sand depth is 0.305 m. The sediment geometric mean, D_g is 0.94 mm and the gradation coefficient σ_g is 1.27. Cobblestone transition zones were placed upstream and downstream of the erodible bed to ensure a gradual transition from the rigid flume bed to the erodible bed. The structures were partially buried in the sand at a depth of 0.305 m from the rigid bed and located 3.35 m downstream of the transition section. The sand bed was extended to 3.85 m downstream of ELJs to ensure that the dynamics of flow and sediment in the wake region was fully captured. Before each experiment, a scraper was used to level the sand bed and the flume was slowly filled with water to a depth of 0.305 m above the sand bed.

The flow discharge was designed such that scour around ELJs was in the clear-water scour regime, i.e., the background shear stress away from ELJs was smaller than the critical value. For the sediment used in this work, the target mean velocity and flow depth were set at $U = 0.26$ m/s and $H = 0.305$ m, respectively, with the control of variable speed pump. The real mean velocities for each experiment slightly deviated from the target value. The mean incoming velocities are determined at 25 points upstream of the structure, where the flow is fully developed and unaffected by the structure. Discharge for each cell around these points is computed by multiplying its velocity with its area. The average velocity is then derived by dividing the total discharge by the flume cross-sectional area for each experiment. The measured mean velocities with a Nortek Vectrino Plus Acoustic Doppler velocimeter (ADV) and other test conditions of experiments are presented in Table 2.2. The Reynolds number and the Froude number

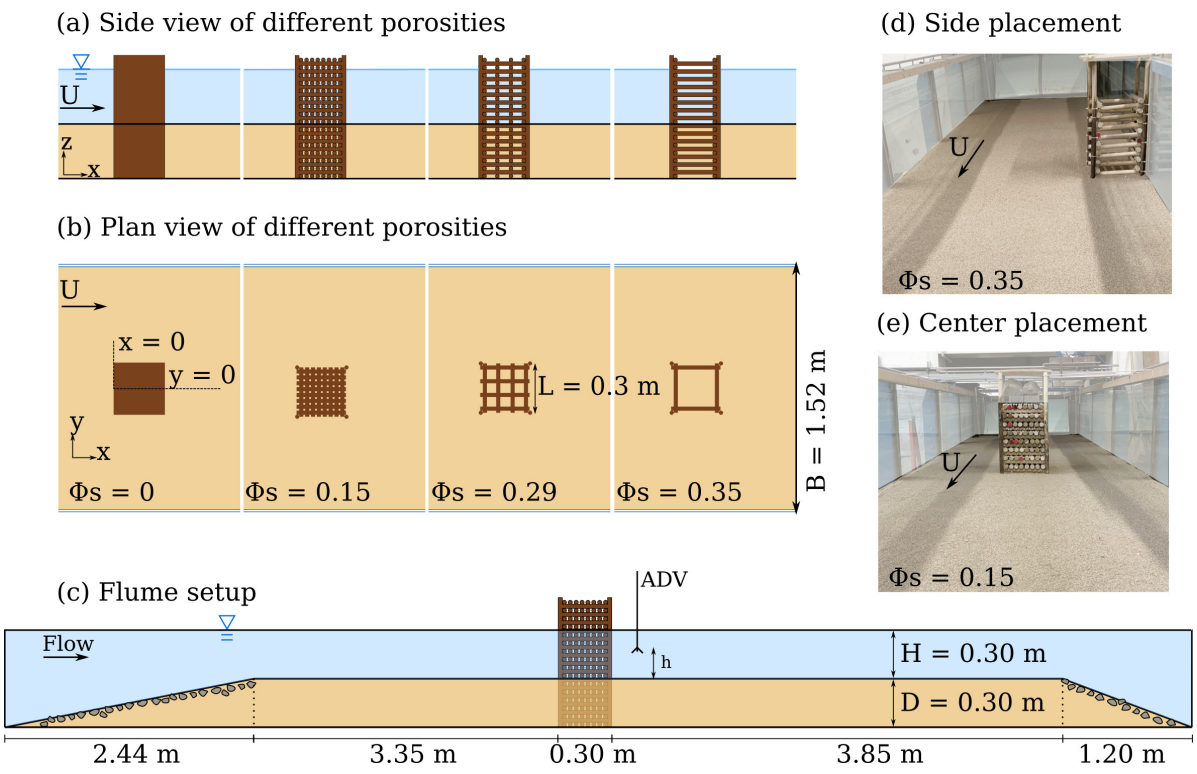

Figure 2.1. Experiment setup and initial flume condition

for the target flow condition are $Re_D = UD/\nu = 7.9 \times 10^5$ and $Fr_H = U/\sqrt{gH} = 0.15$, respectively. Here, D is the length scale of ELJs which is their side length, ν is the kinematic viscosity, and g is the gravitational acceleration. The mean velocity and the water depth for clear-water scour were determined through the combination of the Chezy equation and trial-and-error, such that the Shields number is less than the critical Shields number. The critical Shields number for the sand used is estimated to be $\theta_c = 0.0171$ [Brownlie, 1981, Parker et al., 2003]. The Shields number is defined by Shields [1936] as

$$\theta = \frac{{u_*}^2}{RgD_g} \tag{2.1}$$

where u_* is the shear velocity, R is the submerged specific gravity of sediment, and D_g is the grain size.

The inlet velocity profile along the vertical direction z was measured with the ADV in a cross section located at 1 m upstream of the ELJs. The profile was fitted to the log-law with the form of

$$\frac{u}{u_*} = 2.5 \ln\left(\frac{30z}{k_s}\right) \tag{2.2}$$

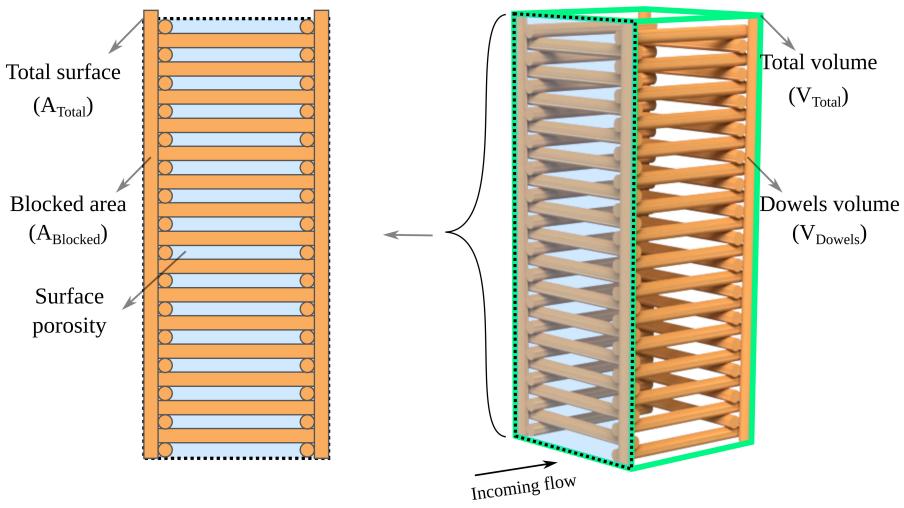

Figure 2.2. Surface and bulk porosity definitions

which provided the the Nikuradse equivalent sand roughness, k_s, and the friction velocity, u_* Roulund et al. [2005]. To reduce the length of this paper, the fitted inlet velocity profile is shown in the Supplemental Information. The fitted k_s has a value of 0.005 m and u_* has a value of 0.015 m/s. k_s is 5 times the value of D_{50}, which falls within the reasonable range of $ks = 1$ to 5 times D_{50} (or D_{65}, and D_{90}) as suggested by the literature [Sumer et al., 2002, Camenen et al., 2009, Julien, 2010]. As a confirmation, the Shields parameter calculated with Eq. 2.1 has a value of $\theta = 0.015$, which is smaller than the critical value to ensure the clear-water scour regime.

2.2.2 Measurements and Data Processing

After the flume was filled with water to the desired depth, each test was then started by gradually increasing the flow to the targeted discharge. Local scour around ELJs started immediately. Depending on the porosity of ELJs, the time to reach scour equilibrium varied in a relatively wide range (45 to 125 hours; see Table 2.2). In general, the increase of porosity in ELJs will increase the time to equilibrium.

Tests continued until the bed morphology reached a state of equilibrium, where no further significant changes were detected in the erodible bed. During the experiments, we periodically measured the maximum scour depths using a measuring tape affixed to the engineered ELJ, aligning these measurements with the time elapsed since the experiment began. Furthermore, we employed photographs to document the exposed dowels to the flow (which were initially buried), enabling us to confirm the maximum scour depth and location at specific intervals. Upon reaching this scour equilibrium,

velocity measurements were taken with an Acoustic Doppler Velocimeter (ADV) both upstream and downstream of ELJs. These measurements capture the effects that changes in the erodible bed, such as scour and deposition. Data quality assurance was achieved by adjusting the ADV measurement properties. Based on recommendations from García et al. [2005], signal-to-noise ratio was adjusted to be above 20 dB and the signal correlation was greater than 70%. Sampling frequency is defined as $F = f_a L/U_c$, where f_a is the sampling rate, and L and U_c are the integral length (flow depth) and velocity scales (free stream velocity), respectively. F was set to be greater than 20 in order to prevent errors associated with filtering. In order to satisfy the $F > 20$ requirement, a frequency of 40 Hz and a measurement duration of 60 s were used. The velocity raw data were post-processed and de-spiked for analysing the velocity and turbulence using techniques described in Goring and Nikora [2002]. The time-averaged mean velocity and the fluctuating velocity components for each point measurement were calculated in the x, y and z directions, and the turbulent kinetic energy (TKE) was calculated as

$$TKE = k_t = 0.5(\overline{u'^2} + \overline{v'^2} + \overline{w'^2}) \tag{2.3}$$

where u', v', and w' are the deviations of velocity components from the respective means.

Velocity point measurements were made on four horizontal planes located at 0.02, 0.05, 0.08, and 0.15 m from the initial flat bed. The depths of these planes correspond to z/L values of 0.07, 0.16, 0.26, and 0.49, respectively. The horizontal range of the measurement section is defined as follows. In the streamwise direction, x/L is from -0.5 to 4 (x/L = -0.5 to 13 for Cases 3, 7 and 8). In the spanwise direction, y/L is from -1.5 to 1.5 for center placements and y/L is from 0.5 to 2.25 for side placements (y/L = -0.25 to 2.25 for Cases 7 and 8). Hence, for the middle placement cases, the velocity measurement grid extended L distance on both sides of ELJs. For side placement cases, the velocity measurement grid extended at least $2L$ distance into the middle of the flume. After velocity measurement was completed, the pump was turned off and the flume was slowly drained. An Artec Eva 3D scanner was used to scan the final bathymetry.

2.3 Results and Analysis

2.3.1 Mean Flow Field

Explaining the morphological patterns around ELJs requires an understanding of the flow field. For solid structures such as bridge piers, the flow structure and scour are

Table 2.2. Summary of test conditions of eight experiments

Case number	Case 1*	Case 2*	Case 3	Case 4	Case 5*	Case 6*	Case 7	Case 8
Structure type	Solid	Solid	Porous	Porous	Porous	Porous	Porous	Porous
Location	Side	Middle	Side	Middle	Side	Middle	Side	Middle
A_{Total} (m^2)	0.09	0.09	0.09	0.09	0.09	0.09	0.09	0.09
$A_{Blocked}$ (m^2)	0.09	0.09	0.08	0.08	0.07	0.07	0.06	0.06
ϕ_s	0	0	0.15	0.15	0.29	0.29	0.35	0.35
ϕ_v	0	0	0.45	0.45	0.72	0.72	0.85	0.85
H	0.30	0.30	0.30	0.30	0.30	0.30	0.30	0.30
$U_{ave,\,in}(m/s)$	0.25	0.26	0.26	0.25	0.26	0.27	0.26	0.25
$Q_{in}\,(m^3/s)$	0.11	0.12	0.12	0.17	0.12	0.12	0.12	0.12
Fr_H	0.14	0.15	0.15	0.14	0.15	0.15	0.15	0.14
Re_d	75335	80215	79605	76250	79300	81740	78995	76250

* Ismail et al. [2021]

well understood. For example, the major flow features are the downward flow toward the bed in the upstream region, the horseshoe vortex around the structure, and the wake downstream. Subject to these flow features, sediment particles may be picked up and carried downstream, resulting in scour [Melville and Coleman, 2000, Garcia, 2008]. With porosity, these major flow features are altered, which has implications for sediment transport. The schematic diagram of flow alteration around a porous ELJ compared to solid model is shown in Figure 2.3. In this section, detailed analysis is made on the flow features.

Approaching flow deceleration

Contours of mean streamwise velocity on a horizontal plane at half water depth, $z = H/2$, are shown in Figure 2.4. For all cases, the flow decelerates in the upstream region of ELJ. The degree of deceleration depends on porosity and the placement of ELJs. To quantify, the streamwise and spanwise velocity profiles at $z = H/2$ are shown in Figure 2.5. As porosity increases, the velocity deceleration upstream decreases. Flow deceleration also depends on the placement of ELJs in the flume. For instance, the flow deceleration in upsteam of ELJs is more pronounced for side placement cases compared to center placements. For the solid cases, at x/L = -0.25, the streamwise velocity in the upstream region drops to $0.75U$ and $0.5U$ for center and side placements, respectively. For porous structures, the upstream velocity drops less to $0.9U$ for center placement

with $\phi_s = 0.29$ and $0.75U$ for side placement with $\phi_s = 0.35$. Difference in approaching flow deceleration stems from a higher stagnation pressure for solid cases and increased bleeding flow through highly porous ELJs.

Shear layers

Shear layers form due to the velocity difference between the wake and the side regions of ELJs. The strength and extent of shear layers determine the turbulence and the capability of the flow to carry sediment. The bleeding flow through porous ELJs reduces the strength of shear layers through two mechanisms. The first is the increase of downstream velocity in the wake area and thus smaller velocity difference. The second is the reduction in blockage effect. Part of the incoming flow passes directly through the porous structure and thus reduces the amount of flow going along the sides of ELJs. This essentially slows down the flow in the side regions of ELJs.

The increase of porosity decreases the strength of shear layers. For the solid cases, the flow separation and shear are more prominent than their porous counterparts. For porous cases, the shear layer is closer to the ELJ structures than the solid cases. This can be observed by the streamwise velocity contours in Figure 2.4 and lateral velocity profiles in Figure 2.5 (b) and (c). For the solid, center placement case, the accelerated velocity contour line of $\overline{u}/U = 1.1$ begins at $y/L > 1$ and $0 < x/L < 2$. For comparison, for most porous ELJs such as Case 8, this contour line starts at x/L =0.5 and extends downstream instead of laterally. The spatial extent of the flow can be used to explain the spatial variation of the scour morphology, such as the width of the scour hole.

In reality, the porosity of ELJs may evolve with time. The porosity usually decreases as debris and small wood clog ELJ's interstitial space. The results in this work implies that the hydrodynamics and morphodynamics will evolve over time too. Newly installed ELJs with larger porosity will induce less flow obstruction and shear. However, old ELJs with decreased porosity will impart more flow obstruction and much stronger shear layers should be observed. Understanding the dynamic evolution of ELJ's porosity helps better design and ecosystem service evaluation.

Wake and recirculation zone

Downstream of ELJs, wake vortices are a key feature that contributes to sediment transport. Within the wake zone, a recirculation zone may exist if the porosity is not high enough. A signature of a recirculation zone is the negative streamwise velocity, i.e., $\overline{u} < 0$. Figure 2.4 shows that the area with negative streamwise velocity is larger in the solid

cases than the porous cases. For ELJs placed in the center, the recirculation zone is closer to the solid structure and starts at x/L=2 and continues to about $x/L = 3$ (Figure 2.4 (a)). In contrast, for porous ELJs with $\phi_s = 0.15$, 0.29, and 0.35, the negative streamwise velocity is negligible indicating the absence of a recirculation zone. However, downstream of porous ELJs, there exist wake zones characterized by a significantly reduced velocity magnitude. The same observations are made for ELJs placed along the side of the flume, which is shown in longitudinal velocity profiles in Figure 2.5 (c).

As depicted in Figure 2.4, the wake and recirculation zone is more extensive for center placements compared to side placements. For example, downstream of the side solid case, there is a negative velocity value of $\overline{u}/U = -0.1$, which is lower than the corresponding value of $\overline{u}/U = -0.4$ downstream of the center solid case.

In contrast to the solid cases, the velocity reduction in wake zone for most porous ELJs placed in the center is low and nearly constant, which can be observed in the longitudinal velocity profiles in Figure 2.5 (a). Velocity variation in the longitudinal direction for the solid case continues to x/L=4, which changes by about 50% from x/L=3.5 to 4, whereas for the porous case with $\phi_s = 0.35$ the velocity change is less than 10%. Similarly, for ELJs placed along the side (Figure 2.5 (c)), for Case 3 with ϕ_s=0.15, the velocity variation continues to $x/L = 8$. For Case 7 with ϕ_s=0.35, the velocity is almost constant after $x/L > 4$.

Differences in the wake and recirculation zone can also be observed in the spanwise direction. Figure 2.5 (b) and (d) show the lateral profiles of the mean streamwise velocity at $x/L = 2$. The general trend in profiles for the solid and porous cases is similar. For porous cases, however, the profiles have more positive values because the bleeding flow through ELJs reduce or eliminate recirculation. The lateral extent of the wake where there is a velocity reduction compared to the streamwise velocity is greater for the solid cases than the porous cases. For ELJs placed at the center, the wake width is $y/L > 3$ for the solid case, $2 < y/L < 3$ for Case 4 ($\phi_s = 0.15$), $y/L < 2$ for Case 6 ($\phi_s = 0.29$), and $y/L < 1.5$ for Case 8 ($\phi_s = 0.35$). When ELJs are placed along the side, they are within the boundary layer of the flume's side way. Thus, a lower velocity reduction is observed in both lateral and longitudinal profiles. For the solid Case 1, the extent of lateral velocity reduction is at $y/L = 1.75$. For porous cases, the same extent is about $y/L = 1.5$. For the most porous ELJ (Case 7), velocity recovers to the approaching flow within a shorter distance from the trailing edge of the ELJs. The implication is that for more porous cases and side placement, the scour and deposition will be closer to ELJs and less drastic.

2.3.2 Turbulent Flow Field

Turbulence is investigated from the point of view of identifying the peak position and magnitude in this section. This will help us to understand how porous ELJs result in different bathymetric changes. TKE (k_t) contours are shown in Figure 2.6. As porosity increases, turbulence in the wake of the ELJs decreases, and its peak position happens at further distances downstream. Peak k_t is about five times larger for solid than the porous case with $\phi_s = 0.35$. For ELJs at the center of flume, the x coordinates of $k_t = 0.5U^2$ contour line for solid case is $x/l < 2$, while for the case of $\phi_s = 0.15$ it is $x/l > 2$. The same trend is true for two more porous ELJs. For example, the position of $k_t = 0.3U^2$ starts at $x/l = 2.75$ for $\phi_s = 0.29$, and $x/l = 3$ for $\phi_s = 0.35$. When compared to porous cases, the magnitude of peak k_t, as well as the area of higher k_t in the contours, are larger for solid cases. The same trend holds true for structures placed to the side, however the highest k_t value is generally lower than center cases. For side ELJs, the $k_t = 0.5U^2$ contour line for the solid case is located at $x/L = 2.5$ while for $\phi_s = 0.15$ it is located at a larger distance ($x/L > 3$). For two more porous structures, Cases 5 and 7 with $\phi_s = 0.29$ and $\phi_s = 0.35$ respectively, the peak of the k_t contour line is about $0.1U^2$, which happens on the side and downstream of the ELJs (Figure 2.6). For the TKE contours, it is also clear that the wake for side-placed ELJs is narrower than that for the center-placed ELJs.

Figure 2.7 shows the longitudinal and transverse profiles of normalized TKE. The longitudinal profile of TKE shows that the peak for $\phi_s = 0.15$ occurs around $x/L = 4$, and $x/L = 2$ for $\phi_s = 0.35$. As porosity decreases, the distance from the upstream edge of the ELJs to the peak turbulence increases.

Shear layers and high TKE variations at the sides and downstream of the ELJs cause scouring to extend from upstream to downstream. Figure 2.7 (b) and (d) show the transverse profiles of TKE at $x/L = 2$. In general, these profiles have similar trends. TKE increases downstream in the wake and decreases outside. However, the magnitude and position of high and low values of TKE on the profiles depend on the porosity. In both center and side channel placements of ELJs, TKE magnitude decreases as porosity increases. This is because the bleeding flow suppresses the turbulence shear and TKE production.

2.3.3 Scour hole morphology

Porosity and structure placement have great influence on the equilibrium scour hole morphology. As an example, Figure 2.8 shows photos of the equilibrium scour holes for

two porosities of $\phi_s = 0.15$ and 0.35 ($\phi_v = 0.45$ and 0.85) and two placements (side and center). They correspond to Cases 3, 4, 7, and 8. The equilibrium bathymetries of all cases are shown in Figure 2.9 where the scour and deposition are normalized by the length scale L of ELJs. The position of ELJs are shown with square patches. Qualitatively, Figure 2.9 and Figure 2.8 show that as porosity changes, scour and deposition differ drastically in both shape and magnitude. In general, solid cases exhibit more profound morphological changes than porous cases for both side and center placements of ELJs.

The scour hole morphology can be quantified by maximum scour depth ($d_{s,max}$), the height of downstream bar (z_p), and the horizontal and lateral extents (l_s, l_p,and w_s; see Figure 2.10 for their definitions) at the equilibrium. The maximum scour depth, observed on the upstream side of the structure at equilibrium, initially formed at the structure's upstream edge and gradually extended towards its middle during the experiment. The measured scour hole morphological metrics are listed in Table 2.3.

Scour hole size and depth decrease as porosity increases for both side and center placements of ELJs. For center-placed cases, the maximum scour depth is about $0.96L$ for the solid case ($\phi_s = 0$), $0.72L$ for Case 4 ($\phi_s = 0.15$), $0.68L$ for Case 6 ($\phi_s = 0.29$), and $0.5L$ for Case 8 ($\phi_s = 0.35$). Thus, scour depth decreases substantially, almost by 50%, from the solid case to the most porous case. As discussed in the previous section, a shallower scour hole is consistent with the weaker flow deflection towards the bed in the upstream of ELJs (Figure 2.5) caused by bleeding flow through logs and less stagnation.

The extent of scour in the spanwise direction, i.e., the width of scour hole (w_s), is about $4L$ for the solid case ($\phi_s = 0$), $3.8L$ for Case 4 ($\phi_s = 0.15$), $3L$ for Case 6 ($\phi_s = 0.29$), and $2.9L$ for Case 8 ($\phi_s = 0.35$). This is consistent with the shear layer and lateral velocity deflection analysis presented in Section 2.3.1. Furthermore, with increasing porosity, the streamwise extents of scour hole (l_s and l_p) decrease. For instance for the center-placed ELJ with $\phi_s = 0.15$, the longitudinal extent of scour l_s is about $4.1L$, while it is about $3L$ for $\phi_s = 0.35$. In contrast to low porosity ELJs (Figure 2.9 (a) and (c)), for higher porosity cases with $\phi_s = 0.29$ and $\phi_s = 0.35$ (Figure 2.9 (e) and (h)), scour do not extend downstream as much, which can be observed in experiment photos in Figure 2.8.

As the porosity increases, the return flow intensity behind ELJs and wake extent decrease. Indeed, the return flow area is a good indicator for sediment deposition as seen Figure 2.9. The streamwise location of the deposition peak is closer to the ELJ and its scour hole as the porosity increases.

Porosity of ELJs also affected the scour and deposition shapes. For less porous ELJs, the scour hole downstream of the structure converged to the centerline and formed a

Table 2.3. Summary of test conditions and results for the eight experimental cases

	Case 1*	Case 2*	Case 3	Case 4	Case 5*	Case 6*	Case 7	Case 8
Structure	Solid	Solid	Porous	Porous	Porous	Porous	Porous	Porous
Location	Side	Middle	Side	Middle	Side	Middle	Side	Middle
ϕ_s	0	0	0.15	0.15	0.29	0.29	0.35	0.35
ϕ_v	0	0	0.45	0.45	0.72	0.72	0.85	0.85
$d_{s,max}/L$	0.92	0.96	0.76	0.72	0.42	0.68	0.4	0.5
l_s/L	> 5	> 5	5.2	4.1	2.5	4	3.3	3
w_s/L	4	3	3.5	3.8	2.5	3	2	2.9
z_p/L	0.33	0.35	0.56	0.42	0.1	0.12	0.06	0.3
l_p/L	6.81	6.34	7.17	4.88	2.19	3.90	1.73	3

* Ismail et al. [2021]

horseshoe shape (Figure 2.9 (a) and (c)). This was not observed in the study of [Follett and Nepf, 2012] for solid and dense circular vegetation patches. The results suggest that the scour hole morphology is affected by the shape of the structures (square vs. circular).

For the center placement of ELJs, the solid case and the case with $\phi_s = 0.15$ have similar morphological patterns, where the deposition bar resembles a triangular wedge. For the cases with $\phi_s = 0.29$ and $\phi_s = 0.35$, the deposition bar consists of two elongated hills separated by an open triangular region in which neither erosion nor deposition have taken place. The difference between the two groups is caused by whether the flow in the wake has enough strength to push sediment toward the middle.

Comparing the bathymetry of side-placement cases with center-placement cases, it is clear that the patterns are similar. If the side wall serves as a mirror, the morphological pattern of the side-placement cases is half of those for center-placement cases. In addition, the magnitudes of scour depth and deposition are also comparable.

2.3.4 Overlapping of flow and bathymetric features

The location and magnitude of significant bathymetric features correspond well with the flow features such as the flow structure, velocity, and TKE (see Figures 2.4 and 2.6). For example, for Case 3 with ϕ_s =0.15 and a side placement, the lowest velocity and highest TKE happen at about $x = 4L$, after which the velocity and TKE recover back to the incoming flow condition at about x=7 L. This corresponds well with the depositional footprint from $4L$ to $7L$ in Figure 2.9 (c). For Case 5 with a center placement, the lowest velocity and the highest TKE are from about $2L$ to $3L$, which is also consistent with the peak deposition that happens at about $2.19L$ (see Figure 2.9 and Table 2.3). Similar

observation can be made for the spanwise extent of bed morphology, which again shows the strong correlation between flow and bathymetric features.

The depositional bar downstream is directly related to the wake and recirculation zone behind ELJs. Comparing the mean flow field shown in Section 2.3.1 and the bathymetry contours in Figure 2.9, it is clear that the recirculation zones have almost the same footprint as the depositional bars for all cases. It is also found that as porosity increases, the correlation among the width of wake and shear layer and bathymetric changes weakens. Nevertheless, the deposition peak occurred at the lowest reduced velocity and the highest TKE downstream. The spatial distribution of velocity and turbulence contains valuable information for sediment movement around ELJs.

2.3.5 Scour depth prediction

We propose a new formula for porosity correction for scour depth prediction which involves both surface and volumetric porosities. Ismail et al. [2021] proposed a simple linear correction to the clear-water scour formula in HEC-18 and the correction is a linear function of ELJ's surface porosity. However, with the extended dataset from this work and the literature, we found it is beneficial to include the effect of volumetric porosity. The reason is that ELJs have different designs in practice and wood members are not evenly distributed within the structures. In a scenario where an ELJ lacks internal wood or materials, its surface porosity serves as the control for passing and blocking flow. In general, surface porosity, ϕ_s, can be interpreted as a gate through which incoming flow enters the porous structures. On the other hand, the volumetric porosity, ϕ_v, characterizes the bulk behaviour of passing fluid and momentum extraction. Thus, it is the combination of both porosities that determines the overall flow and sediment transport around ELJs.

A scour depth correction coefficient due to porosity is defined as

$$s_c = \frac{d_{p,s}}{d_{s,s}} = f(\phi_s, \phi_v) \tag{2.4}$$

where $d_{p,s}$ is the scour depth of a porous structure. $d_{s,s}$ is the scour depth of the corresponding solid structure, which is calculated with empirical scour depth equations under clear-water conditions recommended in HEC-18 for center-placement cases and in the NCHRP 24-20 Report of abutment scour for side-placement cases [Arneson et al., 2012a].

Our goal is the functional form for the scour depth correction coefficient $s_c = f(\phi_s, \phi_v)$.

Our proposed functional form is based on the observed trend from the experimental data and a simple asymptotic analysis. Figure 2.11 (a) shows the contour plot of s_c as a function of both ϕ_s and ϕ_v. Here, s_c was calculated based on Eqn. 2.4. The contour plot includes not only data from this work, but also data for various other porous structures/features in the literature. The extra data include the finite patch of cylinders mimicking aquatic vegetation patches [Yagci et al., 2017, Follett and Nepf, 2012, Kim et al., 2015, Waters and Curran, 2016], porous monopiles Yang et al. [2021], ELJs and dolotimber structures [Ismail et al., 2021, Merook, 2018, Suaznabar et al., 2021] and porous paired deflectors [Kim et al., 2016]. All these cases share the same porous nature. While we recognize the geometric differences between our square ELJ and in-stream structures from existing literature, we have adapted our equivalent solid scour depth calculations to suit each specific scenario. Consequently, differences arising from geometry difference are not contributing to the prediction of scour coefficient. This approach also accommodates varying erodible bed materials, further standardizing our findings across different scenarios.

In Figure 2.11 (a), to plot the contour of s_c, the asymptotic values for $\phi_s = 0$ (the vertical axis) and ϕ_v=0 (the horizontal axis) were also used. When $\phi_s = 0$ or ϕ_v=0, either the surface or the whole volume is impervious. Thus, the structure acts like a solid and s_c should have a value of 1.0. At the origin where both ϕ_s and ϕ_v have a value of 0, the structure is a solid (both inside and out), s_c has a value of 1.0. The other asymptotic behavior is as ϕ_s and ϕ_v both approach 1.0, i.e., toward the upper right corner point, the whole porous structure disappears (no solid) and s_c should have a value of 0. Along the diagonal line from the origin to the upper right corner point, the porosity inside and out is uniform, i.e., $\phi_s = \phi_v$, and the porosity correction coefficient s_c gradually transitions from 1 to 0. Ismail et al. [2021] used a linear function for this transition.

The contour lines in Figure 2.11 (a) are L-shaped with significant nonlinearity near the origin and gradually become linear close to the upper right corner. This behavior can be described by a production function of ϕ_s and ϕ_v as

$$s_c = 1 - a{\phi_s}^b{\phi_v}^c \tag{2.5}$$

This functional form satisfies the asymptotic behaviors described above for $\phi_s = 0$ and $\phi_v = 0$. A non-linear least squares method was used to fit the data and find the coefficient in Eq. 2.5. Since at the upper right corner point $\phi_s = \phi_v$ =1, and $s_c = 0$, a has to be 1. Setting $a = 1$, curve fitting resulted in the values $b = 0.62$, and $c = 1.0$.

For comparison, the contours of the fitted function in Eq. 2.5 are plotted in Figure 2.11 (b). It can be observed that fitted equation captures the trend shown in Figure 2.11 (a). In practice, Eq. 2.5 can be directly used to estimate the porosity correction coefficient for porous structures.

Our new porosity correction coefficient in Eq. 2.5 improves the predictive performance in comparison with the simple linear correction proposed in Ismail et al. [2021], which has the form of

$$s_c = 1 - \phi \tag{2.6}$$

where ϕ is the overall porosity. In this formula, it is assumed that the surface and volumetric porosities are the same, i.e., $\phi = \phi_s = \phi_v$. With this assumption, our new formula in Eq. 2.5 can be simplified as

$$s_c = 1 - a\phi^{b+c} = 1 - \phi^{1.62} \tag{2.7}$$

It is clear that the major difference between the two is the power to the porosity ϕ. Our new data suggested a non-linear power law instead of a linear law. Our new formula is also more general because it can consider the disparity in surface and volumetric porosities. The better performance can be appreciated in Figure 2.11 (c) where the measured s_c of all data points and estimated s_c using our new formula are plotted together. The root mean squares error (RMSE) is 0.09 and the R^2 has a high value of 0.93.

2.3.6 Temporal scaling analysis of scour

The temporal evolution of the scour hole around ELJs is also of great importance to the design and evaluation of such in-stream structures. Using a similar approach as described in Song et al. [2022a], we conduct a simple scaling analysis and introduce a novel function to describe the evolution of scour depth. Previously, temporal scour evolution has also been studied by Melville and Chiew [1999], Oliveto and Hager [2002] and Yang et al. [2020] for bridge piers. A comparison with and appraisal of Melville and Chiew [1999] will be provided.

The scour depth $d_s(t)$ can be made dimensionless with the maximum scour depth $d_{s,max}$, where t denotes time. The dimensionless scour depth can be written as a functional relationship as follows:

$$\frac{\mathrm{d_s}(t)}{\mathrm{d_{s,max}}} = f\left(\frac{u_*}{u_{*c}}, \frac{H}{L}, \frac{L}{d}, \frac{t}{t_e} \; or \; \frac{t}{t_0}, \phi_v, \phi_\mathrm{s}\right) \tag{2.8}$$

where $u*$ is the bed shear velocity and u_{*c} is the critical bed shear velocity, d is sediment diameter, L is the object length scale, t_0 is baseline time scale and t_e is the equilibrium time scale for scour. Let sediment size be D, then since $L/D > 50$, the effect of bed sediment can be neglected [Melville and Coleman, 2000]. The effect of porosity (ϕ_v and ϕ_s) is already embedded in the maximum scour depth $d_{s,max}$. All other parameters are the same for all cases and known except the time scale, t_0.

According to Song et al. [2022a] baseline time scale can be calculated as $t_0 = L^2/q$. In which q is the bedload transport and L is the length scale of the object. There are many empirical bedload transport formulas. In this work, the one proposed in Engelund and Fredsøe [1976] was used:

$$\frac{q}{\sqrt{RgD^3}} = 18.74\,(\theta - \theta_c)\left(\theta^{1/2} - 0.7\theta_c^{1/2}\right) \tag{2.9}$$

where the submerged specific gravity of sediment is $R = (s - 1) = 1.65$ for the sand used. q is the bed load transport which is dependent on applied shear velocity u_* through $\theta = (u_*^2)/(RgD)$. Applied shear velocity due to contraction velocity along sides of porous ELJs is calculated to estimate the bed load transport. Here, the contraction flow is the main scour driver. Contraction velocity itself depends on the surface porosity (ϕ_s), and blockage of the structures $(1 - \phi_s)L$ and width of flume (b), which can be calculated as $U_{contraction} = [Ub]/[b - (1 - \phi_s)L)]$. Having contraction velocity, the applied shear velocity can be estimated as [Song et al., 2022a, Chen et al., 2019]:

$$\frac{U_{contraction}}{u_*} = 5.75 \log\left(\frac{12.2H}{k_s}\right) \tag{2.10}$$

With θ_c previously calculated as 0.0171 in the methodology section and the contraction θ already determined, q can now be calculated. The value of t_0 for ϕ_s values of 0.35 and 0.15 are 0.60 hours and 0.50 hours, respectively. Figure 2.12 shows the nondimensionalized scour depth of ELJs with surface porosity of $\phi_s = 0.15$ and $\phi_s = 0.35$ of side and center placement plotted versus the dimensionless time, t/t_0.

The scour data of all four cases in this study is then fitted to the saturation growth curve in Eq. 2.11. Figure 2.12 displays the fitted equation, where the value of a represents the normalized scour depth at equilibrium which is $s_c = a = 1.02$. When the dimensionless time is equal to b, the normalized scour depth will be half of the equilibrium value, or $s_c = 0.5$ at $t/t_0 = b = 29.49$. The fitted line in Figure 2.12-a closely matches the measurement data.

$$\frac{\mathrm{d}_s}{\mathrm{d}_{\mathrm{s,\ max}}} = \frac{at/t_0}{b + t/t_0} \tag{2.11}$$

To demonstrate the significance of using our proposed formula to estimate the temporal evolution of scour depth in porous structures, we compared it to the formula presented by Melville and Chiew [1999] for solid circular piers. To ensure the comparability of our time scale with Melville and Chiew [1999]'s formula, the equilibrium time scale was estimated using Eq.2.11. In calculating the equilibrium time scale, it is assumed that the scour depth is 95 percent of the maximum scour depth $d_{s,\max}$. By substituting the scour depth ratio and the fitted coefficients a and b, the equilibrium time, t_e, for ELJs with porosity (ϕ_s) values of 0.35 and 0.15 are calculated as 263.89 hours and 220.33 hours, respectively. Following a similar methodology as in a previous analysis, we normalized the scour depth data and time, this time with respect to the equilibrium time t_e, and fitted them to a saturation growth curve. The obtained results are presented in Figure 2.12-b. Our findings suggest that our proposed formula is more suitable for accurately predicting the scour depth of porous squared ELJs, while the equations designed for solid structures fail to provide an accurate estimate for these structures. Additionally, our proposed formula provides a more accurate prediction of the initial scour depth than the equation proposed by Melville and Chiew [1999]. Moreover, the equation proposed by Melville and Chiew [1999] has a limitation that it is not applicable for times greater than the equilibrium time scale, and it predicts decreasing scour depth for large time values, which is physically unrealistic.

2.4 Real World Case Demonstration

The results of the previous sections are based on small-scale experiments. To ensure relevance and applicability at field scale, a "reality check" with real-world data is essential. In this section, we test the proposed scour equation in previous section with a real world case.

The field site is located on the South Fork Nooksack River in the Cascades Range in Washington State. Over the course of several years, bathymetric and flow data have been collected at this site. In the 2000s, ELJs were constructed to direct flow into side and chute channels to increase overall channel complexity and salmon spawning opportunities. Around these structures, significant morphological changes have been observed and measured since the installation of ELJs in this reach. Structure-from-motion (SfM) and

acoustic surveys were combined to measure the detailed topography and underwater bathymetry of the restoration site.

Table 2.4 provides detailed hydraulics, sediment, and ELJ data. A hydraulic data measurement of channel flow from field measurements in 2018 is used to estimate the scour coefficient here. For that measurement, the upstream flow rate was 35.34 m^3/s and the upstream flow depth was 0.6 m. According to the sediment size distributions, D_{50} is about 20 mm. At ELJ #8, the maximum flow depth was 2.5 meters. This resulted in a maximum measured scour depth of 1.9 meters in the upstream side of the ELJ.

ELJ #8 extends 3.7 meters into the channel and its length along the channel is 9.1 meters. On the left bank of the main channel, ELJ #8 was constructed using 40 logs (see Supplemental Information). For the construction of ELJs, about 30 m^3 of smaller wood pieces (slash) were used to fill the voids of the structure, which was about 30 % of the total volume. According to the preliminary design documents of the ELJ #8 [Tribe, 2015], the surface and volumetric porosities are calculated (Table 2.4). In the design of the ELJ#8 some of the logs had rootwad. In the calculation of porosity, we simplified these logs to cylindrical logs without rootwad. Using the equations in NCHRP 24-20 for abutment scour under clear-water conditions [Arneson et al., 2012a], the solid scour depth is calculated as 2.5 meters. Hence, using Eq 2.4, the scour depth coefficient is 0.76, which is consistent with the estimated scour depth coefficient of 0.75 using Eq 2.5.

Table 2.4. Summary of the field ELJ case

Variables	Values
Flow rate Q (m^3/s)	35.34
Water depth H (m)	0.6
D_{50} (m)	0.02
ELJ position (-)	side
ELJ length D (m)	9.1
ELJ width L (m)	3.7
ϕ_s (-)	0.33
ϕ_v (-)	0.47
$d_{p,s}$ (m)	1.9
$d_{s,s}$ (NCHRP 24-20) (m)	2.51
Measured s_c (-)	0.76
Estimated s_c (-)	0.75

2.5 Discussion

This study focuses on ELJs that partially obstruct flow, with minimal impact on water surface levels, in contrast to full-channel spanning LWDs that were the focus of numerous previous studies (Table 2.1).

Our tests reveal that flow features around in-stream structures are crucial for understanding the extent of scour and the locations of peak deposition through the analysis of shear layers, lateral velocity deflection, and peak TKE areas. By collecting data at the equilibrium state of an erodible bed, we account for new types of vortices occurring within the scour hole or resulting from the deposition bars, which lead to further sediment removal. This work offers insights into equilibrium flow dynamics not addressed in previous studies on flat bed (Table 2.1).

Comparing the bathymetric features of ELJs with those from vegetation patch studies reveals different scour patterns. Thus, finding a generalized solution for predicting physical features such as scour for various shapes of porous structures presents a challenge. A key observation is that ELJs and other porous structures with identical volumetric porosities may not exhibit the same surface porosities, and vice versa. Typically, patches of cylindrical dowels, as documented in the literature, display surface porosities greater than 0.5, positioning them closer to the right corner of the $\phi_v - \phi_s$ graph (refer to Figure 2.11). In contrast, ELJs are located on the left side of $\phi_s = 0.5$, with a spectrum of volumetric porosities.

Our analysis emphasizes the importance of both surface and volumetric porosities in influencing flow interaction and structure behavior, revealing a nonlinear relationship between porosity and scour depth. This observation challenges current recommendations [USBR et al., 2016] for predicting scour around ELJs, which typically overestimate scour depth by not accounting for porosity.

There are some limitations in the current research. Our analysis assumes constant porosity, which may not always reflect reality. In the real world, porosity may decrease due to material accumulation in scenarios of high wood supply and transport. The volumetric porosities in our experiments ranged from 0.45 to 0.85. Research by Manners and Doyle [2008] suggests that porosity estimates for wood jams vary between 0.43 and 0.88 during their evolutionary stages in river streams, confirming the relevance of our selected values in the field.

More research should be conducted to investigate the effects of changing porosity on flow and scour. Manners and Doyle [2008] showed that changes in porosity within

naturally formed jams vary with the stages of jam formation. Initially, the stabilization of a key piece does not significantly alter porosity. For example, the jams studied by Wallerstein et al. [2001] falls into this initial stage. Manners et al. [2007] reported that a jam filled with small gravels and branches will not become completely full but will instead achieve a stable porosity, which is the case for fully accumulated jams. Manners and Doyle [2008] further observed that once a jam reaches a stable porosity value, the flow is diverted around the jam, leading to only minor changes in porosity and volume.

Our ELJs, already stabilized with key members, may attract medium-sized or smaller materials, thus altering the porosity based on their initial state. The flow contraction and diversion around Cases 1 to 4 resulted in ELJs with the lowest porosity values, exhibiting behavior similar to natural jams with complete accumulation or older ELJs. Conversely, Cases 5 to 8, characterized by higher bleeding flow through the structure and lower flow contraction, exhibit similarities with natural jams that are partially formed. They are comparable to newly installed ELJs with larger porosity that contain only key logs and may lead to further debris accumulation. For the field case application discussed in this paper, the ELJ serves as an example of a fully accumulated jam, as it was initially filled with small materials such as twigs and gravel. Furthermore, considering that the timescale of porosity changes substantially exceeds that of bathymetric changes, it is reasonable to consider the initially designed porosity as stable and the primary factor influencing bathymetry.

Given the insights from the discussion and acknowledging porosity as a dynamic variable, we recommend that researchers and practitioners apply the proposed correction factor for a minimum scour depth estimate and use existing guidelines for solid structures for a maximum scour estimate. This approach enables informed decisions by providing a range of scour depth for planning and design.

2.6 Conclusions

This study examines flow and morphological features around porous ELJs that partially obstruct flow. The bleeding flow through porous ELJs results in reduced contraction velocity and turbulence production. As a result of these flow alterations, bathymetric features around highly porous ELJs become less prominent. Scour is reduced and more localized to the structure. Porosity also influences the shape of bathymetric features. Depending on the porosity, the reattachment of shear layers downstream of structures can cause the scour to elongate downstream, extending through the centerline of the flow

or towards the side wall of the channel. Consequently, the depositional bar in the wake of ELJs may take the shape of either an open or closed triangular wedge. This comparative analysis of surface and volumetric porosities of ELJs, alongside morphological features, provides insights for erodible bed alteration in river restoration and nature-based solution (NBS) applications.

Current guidelines for predicting scour depth around these NBS are based on principles designed for solid structures and often overpredict scour depth due to neglecting porosity. This study conducted experiments and analyzed structures with a wide range of porosities, leading to an improved scour depth prediction. A scour depth correction coefficient, derived from experimental data and literature, adjusts for surface and volumetric porosities through regression analysis. This new formula significantly improves prediction accuracy over previous methods and its applicability has been confirmed with a field case. Therefore, for practical applications, the findings of this research emphasize the importance of calculating and collecting both surface and volumetric porosity of in-stream NBS for river restoration. Additionally, a simple scale analysis captures the temporal evolution of scour, aiding in understanding the flow-ELJ-sediment system dynamics.

(a) Flow characteristics past a solid obstruction

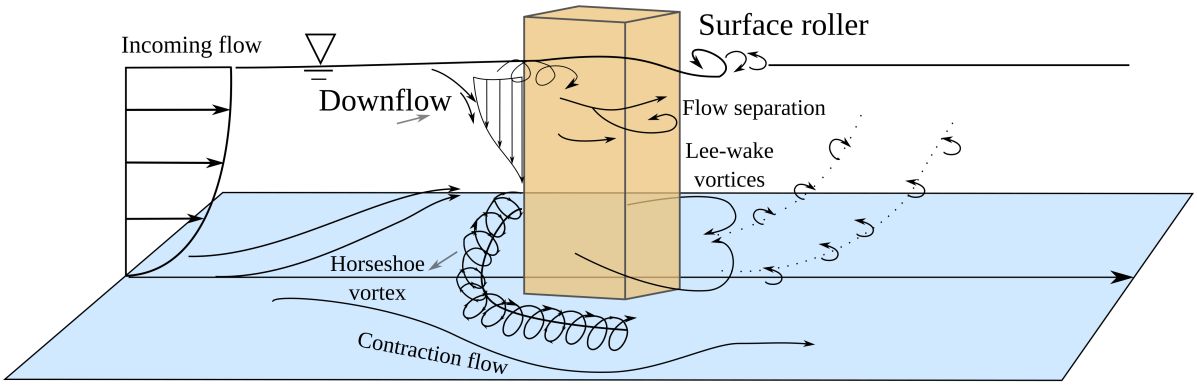

(b) Flow characteristics past a porous ELJ

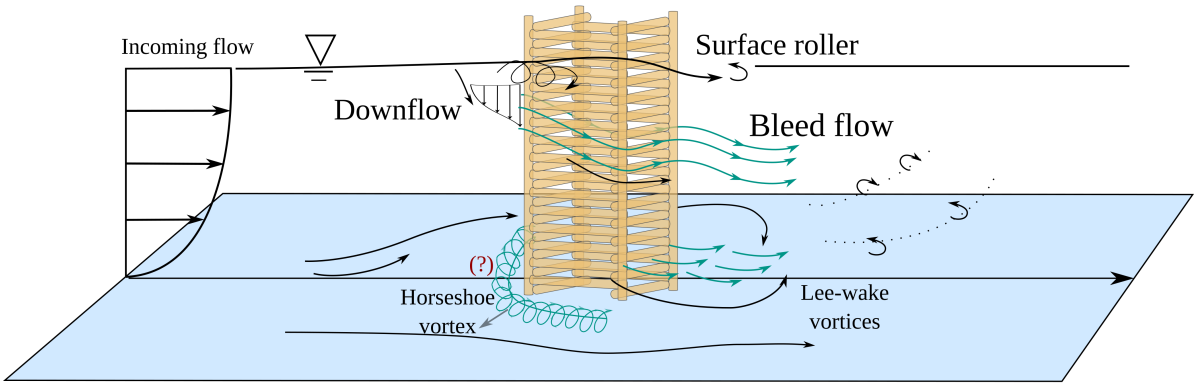

(c) Plan view of flow around ELJ models

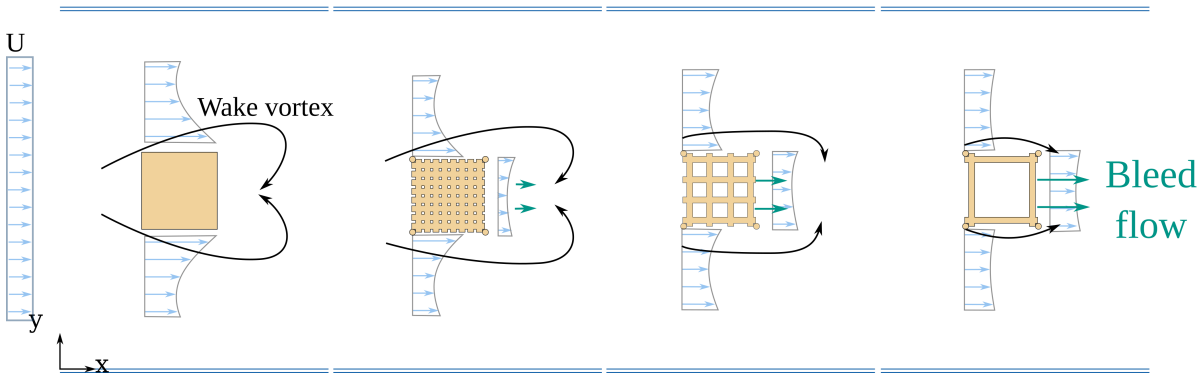

Figure 2.3. Conceptual flow characteristics past (a) solid, adapted from Lai et al. 2022, and (b) porous obstructions, (c) plan view of flow around ELJs with different porosities

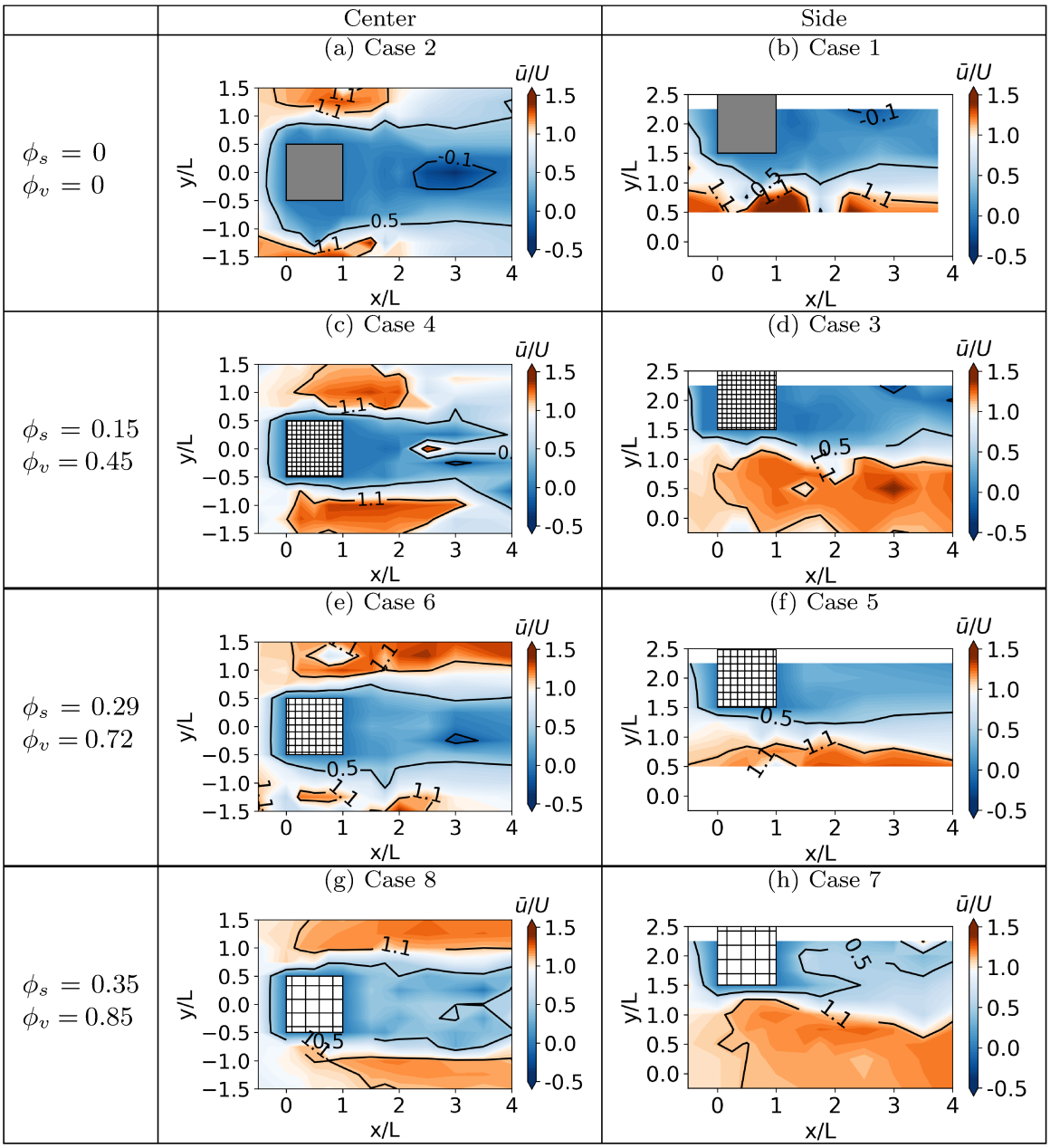

Figure 2.4. Normalized streamwise velocity contour around ELJs. Plots in a, b, e, and f are generated using Ismail et al. 2021 data.

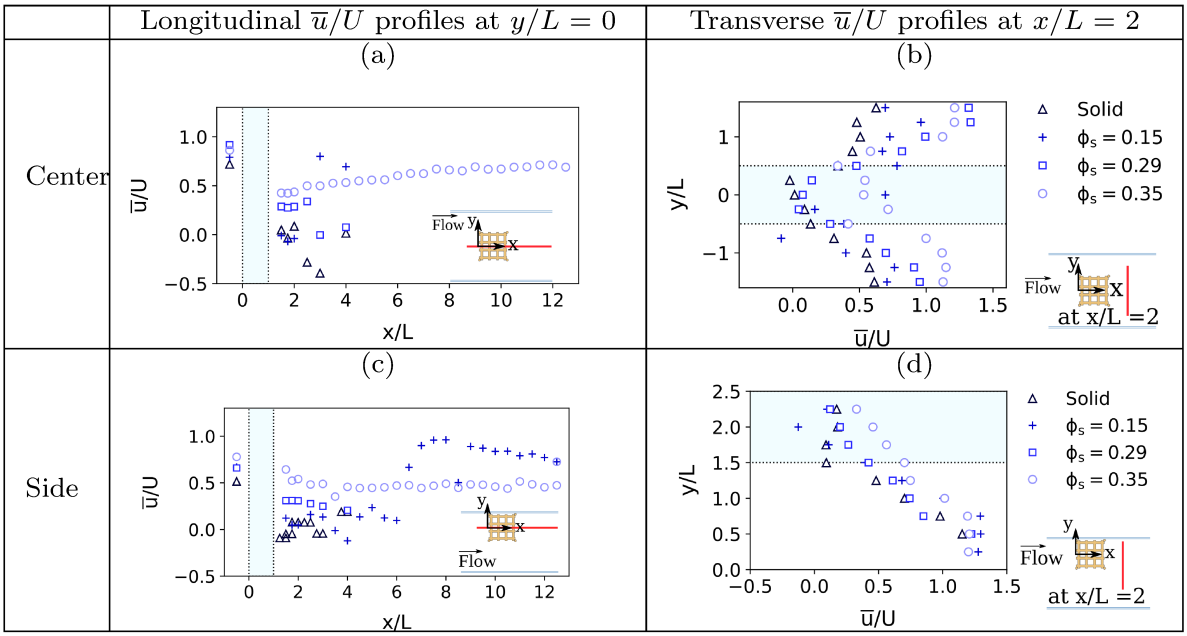

Figure 2.5. Mean streamwise velocity profiles. Solid and $\phi_s = 0.29$ data source: Ismail et al. 2021

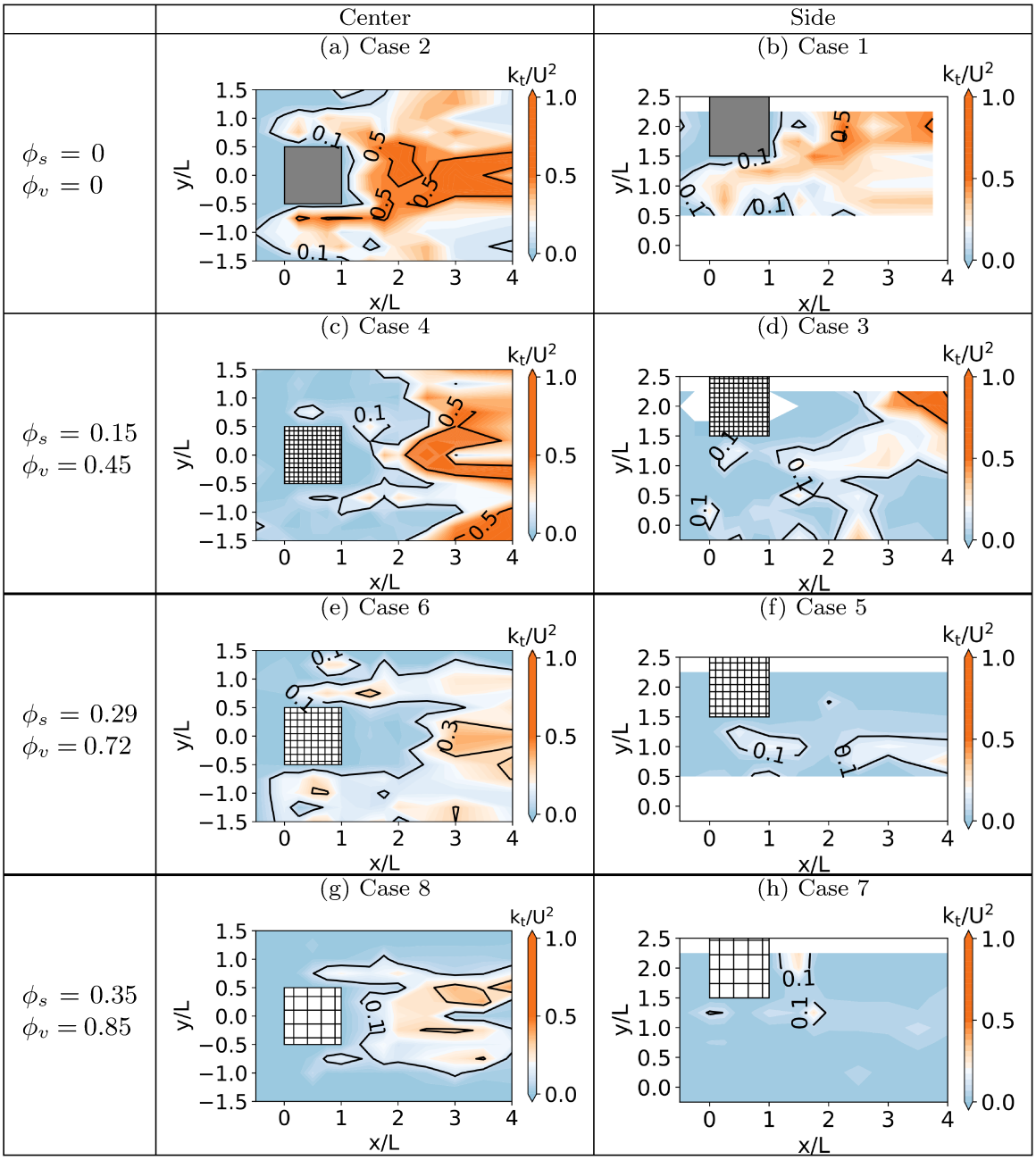

Figure 2.6. Contour of normalized turbulent kinetic energy. Plots in a, b, e and f are generated using Ismail et al. 2021 data.

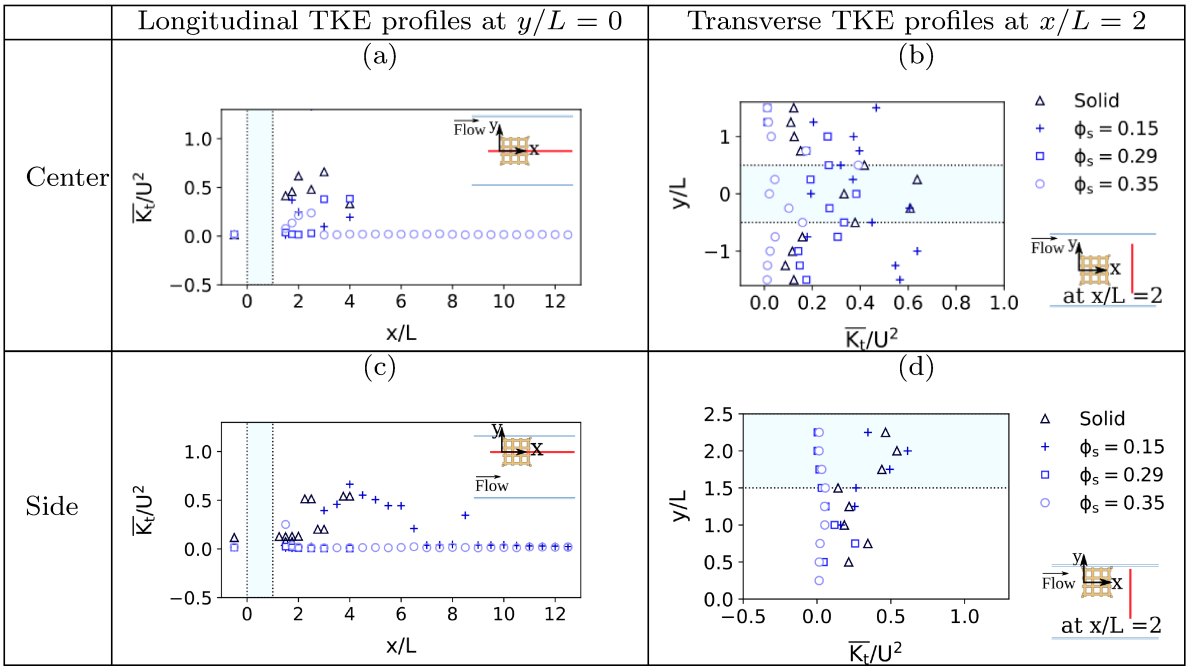

Figure 2.7. Turbulent kinetic energy profiles in longitudinal and transverse directions. Solid and $\phi_s = 0.29$ data source: Ismail et al. 2021

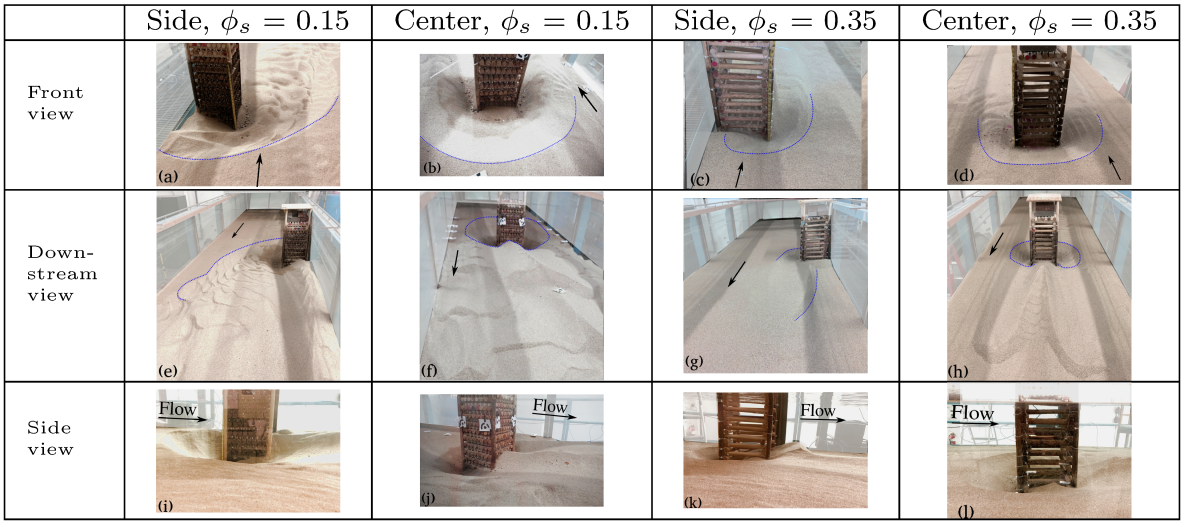

Figure 2.8. Equilibrium scour features of Case 3 (a), (e) and (i), Case 4 (b), (f) and (j), case 7 (c), (g) and (k) and Case 8 (d), (h) and (l). First row shows front view of ELJs, second shows the back view of the ELJs, and third row shows the side view of ELJs.

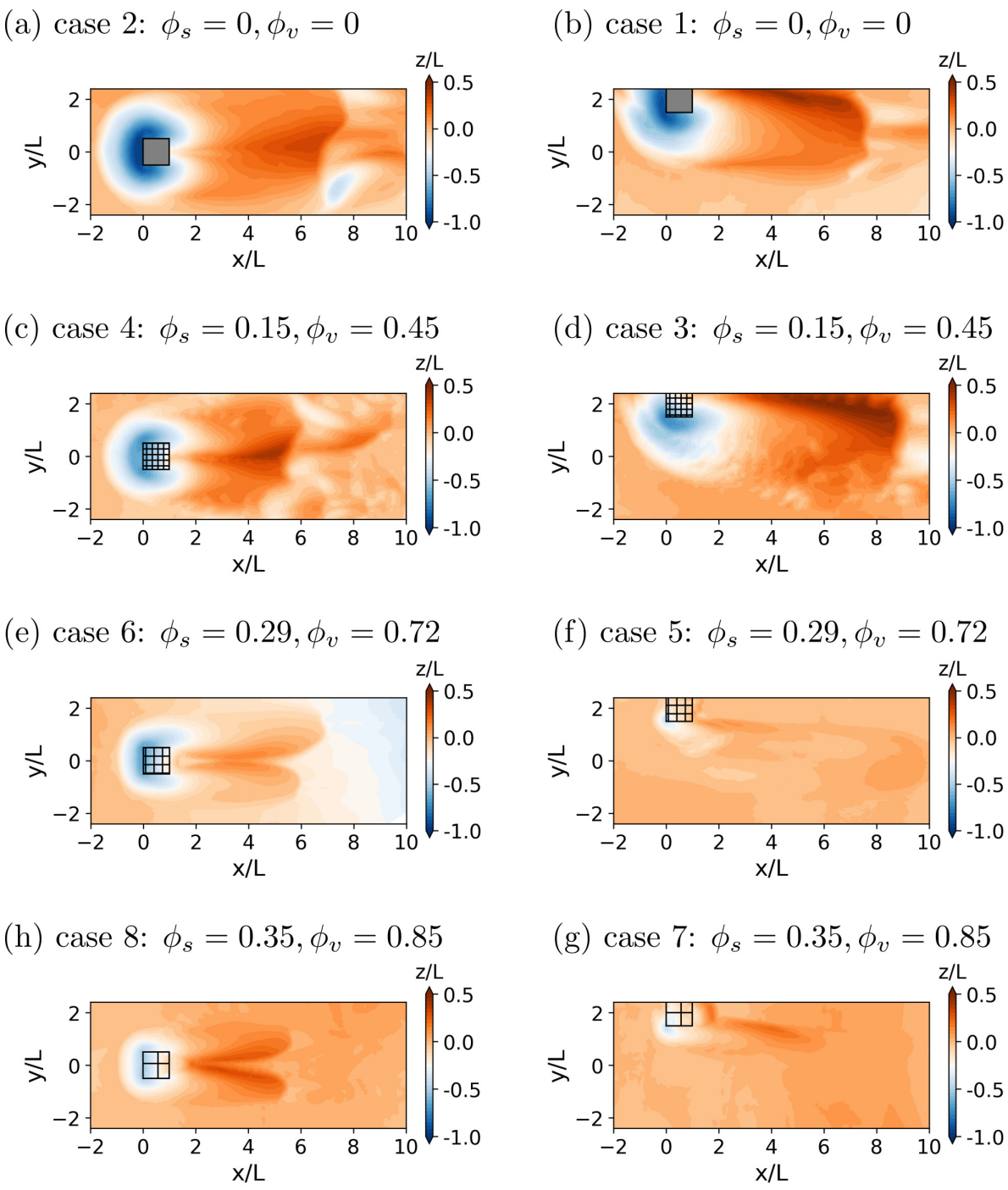

Figure 2.9. Equilibrium bathymetry contours for all cases. Solid and $\phi_s = 0.29$ data source: Ismail et al. 2021

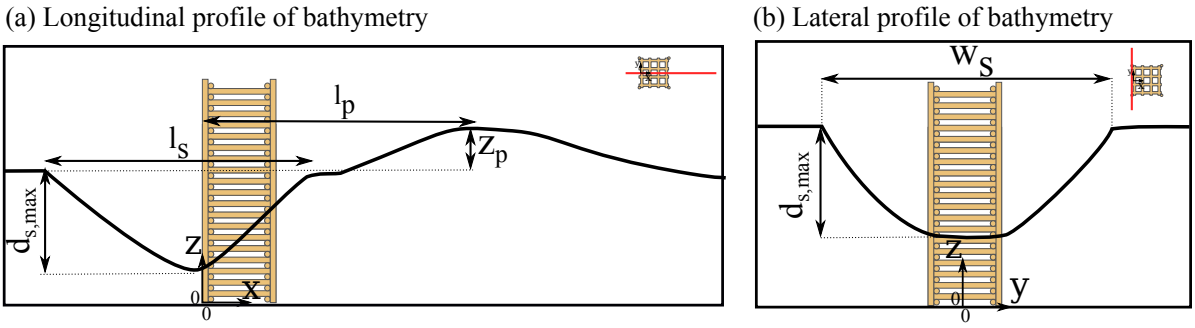

Figure 2.10. Schematic diagram of bathymetric features

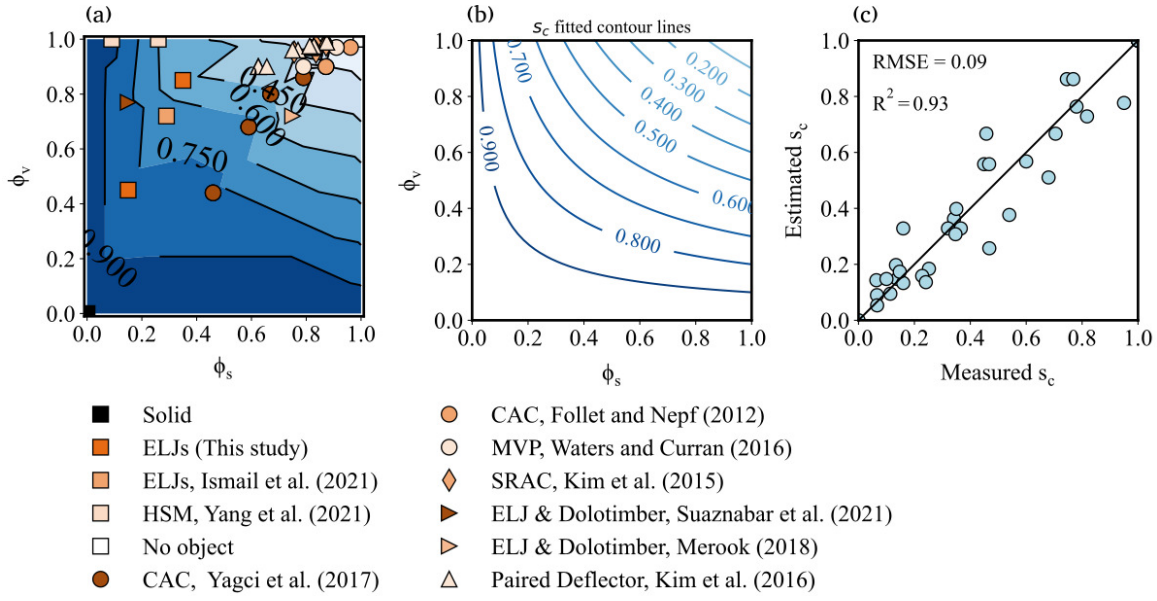

Figure 2.11. (a) Contour of scour depth correction coefficient s_c. Data are compiled from different sources. ELJs: engineered log jams, CAC: circular array of cylinder, MVP: model vegetation patches, SHM: hollow square monopile and SRAC: side rectangular array of cylinders. (b) Contour of proposed scour depth correction coefficient $s_c = 1 - {\phi_s}^{0.62}{\phi_v}^{1.00}$. (c) Comparison between measured and predicted scour depth correction coefficients.

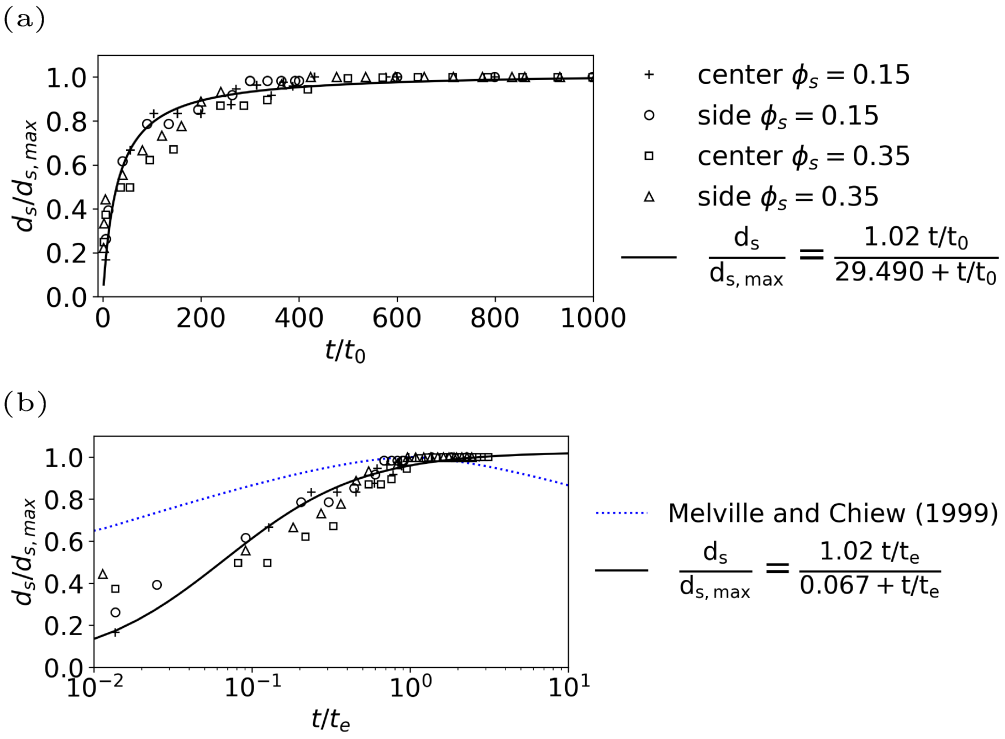

Figure 2.12. Temporal development of normalized scour depth and saturation growth curve fitted line

Chapter 3
Computational Modeling of Flow and Scour around Porous and Solid Hydraulic Structures: Part 1 - Hydrodynamics

3.1 Introduction

Turbulent flow and scour around in-stream structures are crucial to the stability and longevity of these structures. Many in-stream structures, such as the Nature-Based Solutions (NBSs) for river restoration, are porous [Shields Jr and Nunnally, 1984, Brooks et al., 2006, Abbe et al., 2003]. The porosity of these structures makes the flow and sediment transport unique and more complex. The majority of previous studies were focused on solid in-stream structures or simply ignored the porosity effects. A prominent example is scour around bridge piers [Melville and Raudkivi, 1977, Melville, 1997, Kothyari et al., 1992, Ettema et al., 2011, Roulund et al., 2002]. Even in limited studies where porosity was considered, great simplification was used. For example, the geometry of NBSs such as large woody debris (LWD) and engineered log jams (ELJs) was simplified as simple cylinders or solid blocks [Allen and Smith, 2012, Lai and Tullos, 2014, Reichl et al., 2005].

The key flow features around solid structures include upstream downflow, lateral shear layers and lee-wake vortices on the sides and downstream, and horseshoe vortices near the bed [Song et al., 2022b, Ettema et al., 2011, Garcia, 2008, Melville and Coleman, 2000]. It is not clear how porosity changes these flow features. It is possible that new flow

features unique to porous structures may emerge. One main goal of this research is to investigate the shared and unique flow features for solid and porous in-stream structures.

Previously, flume experiments have been performed to understand turbulent flow and bathymetric responses around porous structures such as ELJs on an erodible bed [Mousavi Darzikolaei et al., 2024, Ismail et al., 2021]. These studies mainly provided insights on the equilibrium state, such as the velocity, turbulence, and scour patterns when the system reached final steady state. One major limitation of these flume studies is that it is extremely difficult to capture the temporal evolution of the system, such as the flow, bed shear stress and sediment movement at every stage of scour development.

Computational model provide detailed insights into flow near structures and beds that are difficult to obtain through experiments and field measurements [Ettema et al., 2017]. Advances in computing power and algorithms have made three-dimensional (3D) high-resolution computational modeling feasible in hydraulic engineering practices [Zhou et al., 2020, Lai et al., 2022]. These models are suited for addressing problems that involve detailed local flow and sediment transport processes, such as flow and scour around large woody debris (LWD) and engineered log jams (ELJs) [Xu and Liu, 2017]. However, due to the complexity of the problem, previous studies have either focused solely on turbulent flow or simplified the physics of the problem.

One limitation of previous numerical studies is that fluvial processes around in-stream woody structures and ELJs have often been modeled in two dimensions (2D) [Bennett et al., 2008, L'Hommedieu et al., 2020, Altmann et al., 2024]. Such models are depth-averaged and assume hydrostatic vertical pressure distribution, which cannot capture the details in three dimensions (3D). Scour is a three-dimensional process, especially around structures [Ismail et al., 2021, Mousavi Darzikolaei et al., 2024, Song et al., 2022a, Beheshti and Ataie-Ashtiani, 2010]. Therefore, a 3D model is imperative to compute scour accurately.

Many previous 3D numerical modeling researches have focused on understanding the flow around structures on a fixed flat bed or a bed with equilibrium scour [Koken and Constantinescu, 2014, McCoy et al., 2007, Constantinescu et al., 2009, Kang and Sotiropoulos, 2015a, Xu and Liu, 2017]. These studies provided limited information about the mechanisms of erosion initiation and offered no insights into the evolution of bathymetric features and the corresponding flow characteristics. Therefore, our second research objective is to understand the spatial and temporal development of flow features such as coherent flow structures, wall shear stress, and bathymetric features.

Some relevant numerical studies about porous structures on erodible beds have focused

on vegetation patches [Li et al., 2022]. However, the geometry of these patches differs from in-stream structures used in nature-based solutions for river restoration. While both vegetation patches and these structures share the characteristic of having pore spaces that result in interstitial flow, the internal flow structures are drastically different. Within vegetation patches, the constituent stems are mostly vertical. In contrast, LWDs and ELJs are mostly made of elements stacked both horizontally and vertically. This distinction causes differences in both flow and sediment transport.

To address the knowledge gap and the limitations in previous studies, this work utilized a high-fidelity 3D computational model to study the flow and sediment transport around both solid and porous structures. The key enabler of this study is the immersed boundary (IB) method implemented in the model to capture the evolution of the sediment bed and its interaction with the complex structures [Song et al., 2022a].

In the first part of this study, the focus is on the turbulent flow characteristics unique to porous structures compared to solid ones. Major flow characteristics include velocity field, streamlines, coherent structures, wake zones and flow acceleration areas around ELJs. Flow feature identification helps revealing the underlying mechanisms of sediment transport and the bathymetric features at different stages of scour evolution. The second part of this study focuses on sediment movement drivers and dynamics, specifically the wall shear stress, scour patterns, and scour depth evolution around these structures. Based on the concept of shear decay function, a semi-theoretical model for scour depth evolution was proposed and evaluated.

The rest of this paper is organized as follows. The computer model is described first and then followed by the validation using experimental data from Ismail et al. [2021] and Mousavi Darzikolaei et al. [2024]. Flow field at various stages of morphological evolution is analyzed and compared. The simulated flow field is also depth-averaged and compared to highlight and quantify the limitations of 2D modeling approaches. Coherent flow features are presented to assess the impact of pore spaces in porous structures on flow fields and bathymetry evolution. The percentage of interstitial flow relative to the incoming total flow is computed as a metric for reduced flow blockage due to porosity. This paper is then concluded with a summary.

3.2 Description of the Coupled Hydrodynamic and Sediment Transport Model

An existing 3D scour model, *ibScourFoam*, was adapted and utilized in this work [Song et al., 2022a]. The turbulence was modeled using the $k-\omega$ RANS model, although *ibScourFoam* also provides the large eddy simulation (LES) capabilities. Currently, the use of RANS models is more feasible in this work because scour is a very slow process (in the order of hours to days). RANS models provide a balance between accuracy and computational cost.

A typical 3D scour model such as *ibScourFoam* consists of at least three parts, i.e., hydrodynamic solver, sediment transport solver, and the coupling between the two. The basic idea behind *ibScourFoam* is to model the erodible bed as an immersed boundary within a fixed background mesh. The effect of the bed to the flow is through the special treatment according to turbulent flow within boundary layers. The 3D scour model has been previously used to study other local scour processes with success [Xu and Liu, 2017, Song et al., 2022b,a]. In the following, each of these components of the 3D scour model is briefly described.

3.2.1 Hydrodynamic Solver and Immersed Boundary Method

The governing equations for the hydrodynamics are the unsteady 3D RANS equations, along with the k-ω SST-SAS model for turbulence [Wilcox et al., 1998, Wilcox, 2008, Spalart and Allmaras, 1992]. The continuity and momentum equations for the 3D incompressible flow are shown in Equations 3.1 and 3.2.

$$\frac{\partial \overline{u}_i}{\partial x_i} = 0 \tag{3.1}$$

$$\frac{\partial \overline{u}_i}{\partial t} + \frac{\partial (\overline{u}_i \overline{u}_j)}{\partial x_j} = -\frac{1}{\rho}\frac{\partial \overline{p}}{\partial x_i} + \frac{\partial}{\partial x_j}\left[(\nu + \nu_t)\frac{\partial \overline{u}_i}{\partial x_j}\right] \tag{3.2}$$

where $\overline{u}_i$ represents the Reynolds-averaged velocity component, $\overline{p}$ is the pressure, ν is the kinematic viscosity, and ν_t denotes the turbulent eddy viscosity, which models the turbulent diffusion. t is time, x_i and x_j are special coordinates.

The k-ω SST-SAS model's governing equations are detailed in Equations 3.3 and 3.4. In these equations, k stands for the turbulent kinetic energy, and ω is the specific dissipation rate, which measures the rate at which turbulent kinetic energy (TKE)

dissipates.

$$\frac{\partial k}{\partial t} + \frac{\partial(\overline{u}_j k)}{\partial x_j} = \frac{\partial}{\partial x_j}\left[(\nu + \alpha_k \nu_t)\frac{\partial k}{\partial x_j}\right] + P_k - C_\mu k\omega \tag{3.3}$$

$$\begin{aligned}\frac{\partial \omega}{\partial t} + \frac{\partial(\overline{u}_j \omega)}{\partial x_j} =& \frac{\partial}{\partial x_j}\left[(\nu + \alpha_\omega \nu_t)\frac{\partial \omega}{\partial x_j}\right] + \alpha_\omega \frac{\omega}{k} P_k - \beta\omega^2 \\ &+ \frac{2}{\alpha_{\omega 2}}(1 - F_1)\frac{1}{\omega}\frac{\partial k}{\partial x_j}\frac{\partial \omega}{\partial x_j} + Q_{SAS}\end{aligned} \tag{3.4}$$

Here, $P_k = \nu_t S^2$ is the production term, representing the generation of turbulent kinetic energy from mean flow. The strain rate tensor S_{ij} is given by:

$$S = \sqrt{2 S_{ij} S_{ij}} \tag{3.5}$$

$$S_{ij} = \frac{1}{2}\left(\frac{\partial \overline{u}_i}{\partial x_j} + \frac{\partial \overline{u}_j}{\partial x_i}\right) \tag{3.6}$$

where S is a scalar invariant of the strain rate tensor S_{ij}, indicating the rate of deformation of the fluid element. For brevity, additional terms and coefficients specific to the k-ω SST-SAS model presented in Supplemental Information.

In the IB method, the background mesh conforms to the in-stream structure. The background mesh, which constitutes the computational cells, is classified into three types: fluid cells, immersed boundary cells, and sediment or solid cells. These cells are identified based on their position relative to the immersed boundary (sediment bed). IB cells intersect with the immersed boundary, but their centers fall on the fluid side. Fluid cells are fully located on the fluid side. Solid cells have their centers within sediment. The immersed boundary for the erodible bed is shown in Figure 3.1-a, and the details of the immersed boundary method, including the cell types, are illustrated in Figure 3.1-b.

Flow variables are only solved in the fluid cells. For the IB cells, flow variables are set using a wall model that utilizes the flow information from the fluid cells. The details of this wall model is shown in the Figure 3.1-b. In the wall model, three points are specified: IP, IB, and HP. IB points are at the center of the immersed boundary cells. IP, or image points, are identified in the fluid cells based on an algorithm that calculates their location. The distance of the IP points to the immersed boundary is determined by the smallest size of the IB cells. Specifically, the distance from the immersed boundary to the IP point, d_{IP}, is equal to $3I_{\min}$, meaning the distance is three times the size of the smallest IB cell, $I_{\min}$. HP points are the hit points on the normal line that passes through the image point and intersects the immersed boundary. The flow variables at IP

points are calculated by interpolation from the neighboring cells.

The wall model is based on turbulent velocity profile theory within a boundary layer. In reality, for the velocity profile, the log law applies at a certain distance from the bed. Very close to the bed, i.e., in the viscous sublayer, the velocity profile is different. In the *ibScourFoam* model, to avoid discontinuity that may result from using different wall functions for the laminar sublayer and the log-law layer, the wall model treatment ensures that both the IP point and the IB point fall on the following log law profile using an y^+-based adaptation strategy [Xu and Liu, 2017]:

$$\frac{u}{u_*} = \frac{1}{\kappa} \ln\left(E' \frac{y u_*}{\nu}\right) \tag{3.7}$$

where u is velocity, u_* is the shear velocity, κ is the von Karman constant, y is the distance to the immersed boundary, and E' is a model constant. After the velocity at IP is calculated using the neighboring cells, the wall distance, $y_{ip}^+ = \frac{y_{ip} u^*}{\nu}$, is solved iteratively using the Newton-Raphson method. The shear velocity is calculated based on the definition of wall distance. For more details on the treatment, which is critical for accurate and smooth wall shear distribution, interested readers can refer to Song et al. [2022a].

3.2.2 Sediment Transport Computation

The sediment bed surface is modeled as an immersed boundary, which is in the format of an unstructured triangular mesh. Sediment transport calculation and the updating of bed elevations are carried on the mesh. From the hydrodynamic solver, the flow field and the bed shear stress on the bed surface are available to compute sediment quantities such as bedload flux [Garcia, 2008]. In this work, the bedload transport formula in Engelund and Fredsøe [1976] was used and it has the form shown in Equation 3.8:

$$\frac{q_0}{\sqrt{Rgdd}} = \begin{cases} 18.74(\tau* - \tau*_c)(\tau*^{1/2} - 0.7\tau*_c^{1/2}) & \text{if } \tau* > \tau*_c \\ 0 & \text{if } \tau* \leq \tau*_c \end{cases} \tag{3.8}$$

Here, R represents the submerged specific gravity (=1.65 for natural sand). The variable d denotes the sediment grain size. The Shields number is defined as $\tau* = |\tau|/\rho g \bar{R} d$, where τ is the bed shear stress, ρ is the fluid density, and g is the acceleration due to gravity. The critical Shields number, $\tau*_c$, is calculated using a modified fit of the Shields

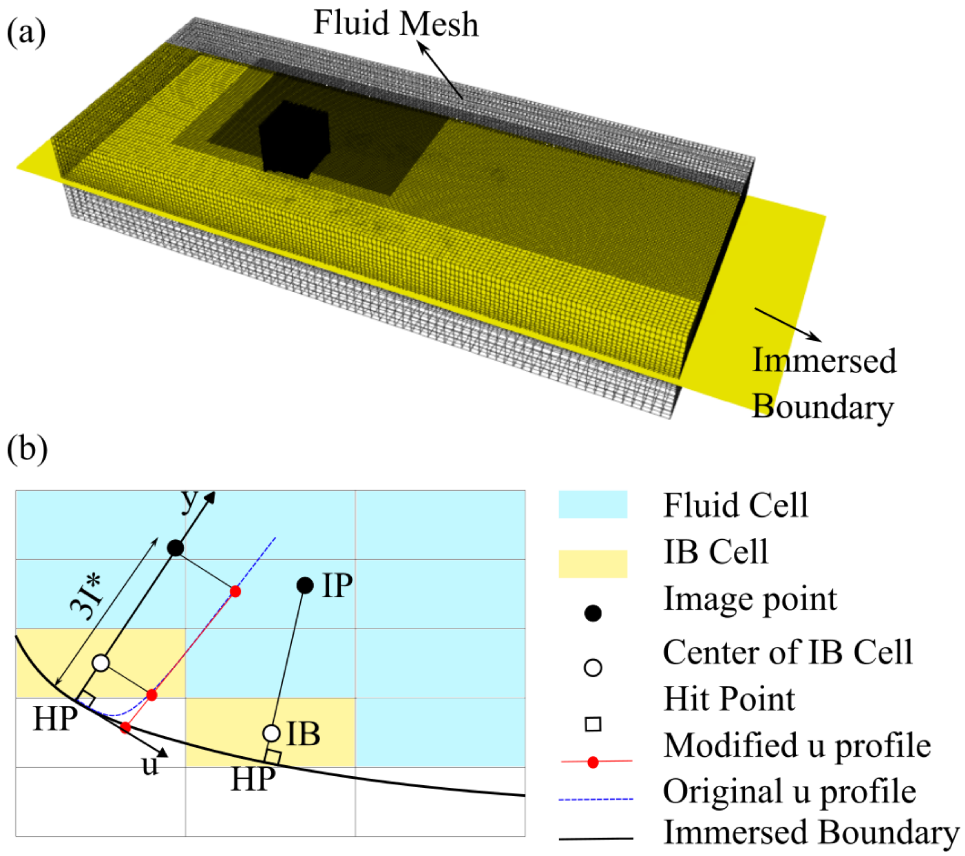

Figure 3.1. Illustration of the immersed boundary method and the treatment of the mobile sediment bed.

diagram from Parker et al. [2003], which has the form of:

$$\tau*_{c0} = 0.5 \times \left(0.22 Re_p^{-0.6} + 0.06 \times 10^{-7.7 Re_p^{-0.6}}\right) \tag{3.9}$$

Where $Re_p = \frac{\sqrt{Rgdd}}{\nu}$. Taking the flow direction and the bed slope into account one can deduce

$$\tau*_c = \tau*_{c0} \left(\cos\beta \sqrt{1 - \frac{\sin^2\phi \tan^2\beta}{\mu_s^2}} - \frac{\cos\phi \sin\beta}{\mu_s}\right) \tag{3.10}$$

where β is the angle of the local slope, ϕ is the angle between the velocity and bed slope, and μ_s is the static friction coefficient.

In this work, only bedload is considered because the cases in simulations and flume experiments are all in the clear-water scour regime. Suspended sediment transport is very minimal in these cases.

The bedload transport results in bed elevation changes, which can be described by

the Exner equation [Exner, 1925]:

$$(1-n)\frac{\partial z_b}{\partial t} = -\nabla \cdot \left(q_0 \frac{\tau}{|\tau|} \right) \tag{3.11}$$

where z_b is the bed elevation, n is bed porosity and τ is the wall or bed shear stress [Brørs, 1999]. Exner equation is a mathematical description of mass conservation for sediment in bed. It may result in unphysical local bed slope which may exceed the angle of repose. In reality, when the angle of repose is exceed, sediment particles will slide down in an avalanche fashion. To account for this physical process, a sand slide model is employed. Sand slide is a diffusion-like process to smear out excessively steep local bed terrain. Thus, the diffusion flux is bounded by the exceedance of local bed angle over the angle of repose. Specifically, the diffusivity for sand slide flux is capped at zero when the bed angle is less than the angle of repose. Mathematically, the formula for the diffusivity K is

$$K = \begin{cases} K_0, & \text{if } |\nabla z_b| \geq \tan(\phi_0) \\ 0, & \text{otherwise} \end{cases} \tag{3.12}$$

where K_0 is a base diffusivity which can be tuned to ensure numerical efficiency and stability. It is set to a value that is neither too small, to avoid excessively long sand slide computations, nor too large, to prevent overcorrection. ϕ_0 is the angle of repose. Once the sand slide diffusivity is determined, the sand slide process is then governed by a generic unsteady diffusion equation [Roering et al., 1999, Song et al., 2020]:

$$\frac{\partial z_b}{\partial t} = K \nabla^2 z_b \tag{3.13}$$

The solution of this equation updates the bed elevation due to sand slide until the bed angle throughout the entire domain is less than or equal to the angle of repose. The sand slide process is incorporated into the scour simulation after solving the Exner equation. More details about the sand slide model can be found in Song et al. [2020].

3.2.3 Coupling Flow Computation and Sediment transport

The *ibScourFoam* model is capable of switching between flow-only mode and coupling mode with sediment transport. Each simulation can be initialized with the flow-only mode for a specified period of time to allow the flow to fully develop, after which the sediment transport mode can be activated. It is well recognized that the time scale for

sediment transport and morphology (t_m) is much lager than that for the hydrodynamics (t_h). To take advantage of this fact, scour models usually use a morphological factor to accelerate the simulation. The morphological factor α is defined as the ratio between t_m and t_h, i.e., $\alpha = t_m/t_h$.

The *ibScourFoam* was developed the open source platform OpenFOAM version 5.x [OpenCFD, 2014]. It is a computational platform for solving generic partial differential equations using the finite volume method. The details of the numerics are omitted to reduce the length of the main text. However, key information about the discretization schemes for the important terms in the governing equations is provided in Table 3.1. In general, second-order accuracy schemes were used in this work. When numerical stability issues arose, certain degree of blending with first-order schemes was adopted. Details about this numerical schemes shown in the table can be found in the User Manual of OpenFOAM [OpenCFD, 2014].

Scheme Type	**Discretisation Scheme**
Time scheme	Implicit backward
Gradient scheme	Gauss linear
Divergence schemes	General: Gauss upwind
	Momentum flux: Gauss linearUpwind
	Turbulent kinetic energy flux: Gauss upwind
	Dissipation rate flux: Gauss upwind
	Scalar field flux: Gauss upwind
	Viscous stress tensor flux: Gauss linear
Laplacian scheme	Gauss linear corrected
Interpolation scheme	linear
Surface normal gradient scheme	corrected for mesh non-orthogonalities

Table 3.1. Discretisation schemes used in the simulations.

3.3 Numerical Simulation Cases

Simulations were conducted on two types of structures: solid and porous. The computational domain is shown in Figure 4.1. The solid case was based on the experiment in Ismail et al. [2021] and the porous case was based on experiments in Mousavi Darzikolaei et al. [2024]. The cases are distinguished by the porous characteristics using both the volumetric and surface porosities. The volumetric porosity ϕ_v, defined as the ratio of the pore space volume to the total volume of the structure, is 0 for the solid structure and 0.85 for the porous structure. Similarly, the surface porosity ϕ_s, defined as the ratio of

the frontal porous area to the total frontal area, is 0 for the solid structure and 0.35 for the porous structure.

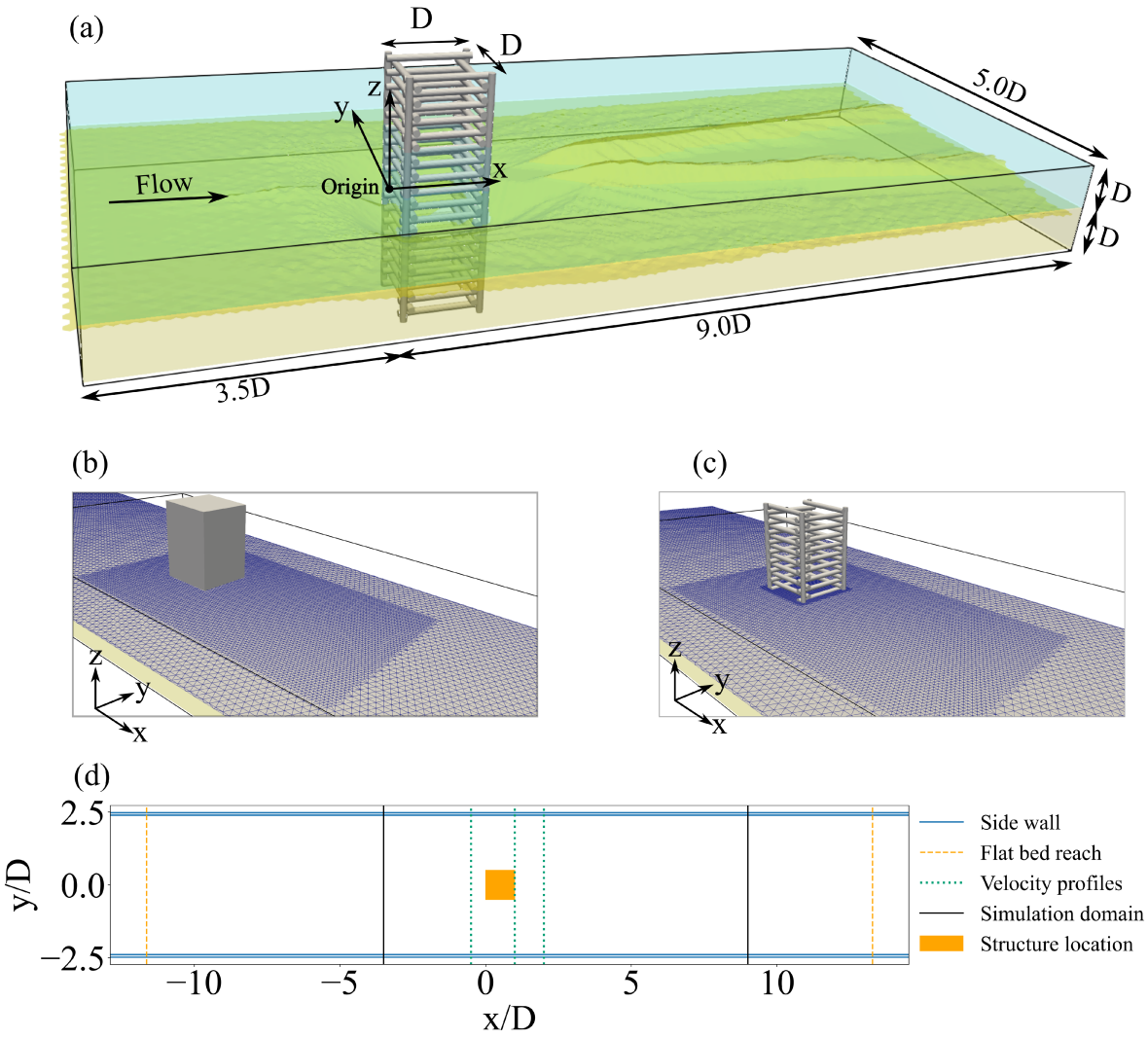

Figure 3.2. Computational domain: (a) overview of the domain. x, y, and z are streamwise, spanwise, and vertical directions. $x = 0$ is on the upstream edge of structure, $y = 0$ is in the middle of channel width, and $z = 0$ is on the initial flat surface., (b) domain for the solid case, (c) domain for the porous case, and (d) plane view and coordinate system definition.

Both solid and porous structures have a square cross-section with a side length D of 0.305 m, placed at the center of the flume. As in the experiments, the water depth is set at $H = D$, and the simulation domain has a length of $11.5D$ the porous structure case and $12.5D$ for the solid structure case. The width and depth of the domain are $5D$ and $2D$, respectively. The side walls of the simulation domain align with those in

the physical experiments. The length of the simulation domain is sufficient to capture the localized morphological changes observed in the experiments. The main flow and geometric characteristics of the simulation cases are summarized in Table 3.3.

The fluid background mesh contains about 6.3 million cells for the solid structure case and 3.9 million cells for the porous structure case. Near the structures, the mesh is refined with increased refinement around the structures and in areas anticipating scour, especially in the vertical direction. The solid structure case has more prominent scour and that is the reason that it has more cells. The immersed boundary surface mesh contains a number of cells specific to each structure type. Its refinement is designed to be comparable to the horizontal cell size of the fluid domain. The immersed boundary surface mesh contains 101,508 cells for the solid structure case and 99,798 cells for the porous structure case.

The boundary conditions are outlined in Table 3.2. For the inlet, velocity profiles, as well as turbulent kinetic energy (k) and specific dissipation rate (ω), were obtained from a pre-simulation of a channel flow without the structure. This approach ensures that the inlet flow conditions replicate a fully developed flow profile typical of an unobstructed channel. At the outlet, the Neumann boundary condition (named "*zeroGradient*" in OpenFOAM) was imposed on all flow variables except for pressure, which was set to zero, ensuring the smooth exit of the flow from the computational domain. The channel's sides were treated as smooth rigid walls. The top boundary was modeled using a shear-free rigid-lid approximation, representing an open-channel flow with no shear stress at the free surface. Both the solid structure and the porous ELJ were modeled as smooth, rigid walls to accurately represent the interaction between the flow and these structures, ensuring no-slip conditions at their surfaces. The sediment bed was treated as a rough wall, characterized by Nikuradse's equivalent roughness (k_s) of 0.005 m, which was derived from fitting the measured incoming velocity profiles in experiments [Mousavi Darzikolaei et al., 2024].

3.4 Model Validation

The computational model was validated with the experimental data from Ismail et al. [2021] and Mousavi Darzikolaei et al. [2024]. Figure 3.3 shows the spanwise profiles of dimensionless streamwise velocity, $\overline{u}/U$, at mid-depth of the flow for experiments and simulations at three streamwise locations: upstream at x/D = -0.5, the downstream edge of the structure at x/D = 1, and one structure length downstream at x/D =

Boundary Type	Boundary Condition
Inlet	specified values for velocity, k, and ω
Outlet	Neumann (*zeroGradient*) for all variables except pressure ($p = 0$)
Sides	no-slip
Top	slip for velocity, *zeroGradient* for k, ω, and p
Structure	no-slip for velocity, wall function for k, wall function for ω, *zeroGradient* for p (treated as walls)
Sediment bed	rough wall with Nikuradse's equivalent roughness (k_s) of 0.005 m

Table 3.2. Boundary conditions applied in the simulation. The details of the boundary conditions can be found in the User Manual of OpenFOAM [OpenCFD, 2014].

Parameter	Solid Case	Porous Case
Mean flow velocity **U** (m/s)	0.26	0.26
Water depth H (m)	0.305	0.305
Length scale D (m)	0.305	0.305
Surface porosity ϕ_s (m)	0	0.35
Volumetric porosity ϕ_v (m)	0	0.85
Domain size (length × width × height)	24.3D × 17D × 2H	25D × 14D × 2H
Total number of cells	6.3 million	3.9 million
Bed Nikuradse's equivalent roughness k_s (m)	0.005	0.005
Median grain size D_{50} (mm)	0.67	0.67
Critical Shields number $\tau*_c$	0.017	0.017

Table 3.3. Summary of computational modeling setups for solid and porous cases.

2. The locations of the three profiles and the overall coordinate system definition are shown in Figure 4.1. All velocity profiles shown are at scour equilibrium. It is important to note that the flow field from the computational modeling was not obtained from a fixed bed hydrodynamic simulation as done in many previous researches [Lazzarin et al., 2024, Koken and Constantinescu, 2021]. Instead, the flow field and the sediment scour co-evolved in the simulations until equilibrium, which is significantly more difficult to achieve good validation results.

The velocity profile comparison shows moderately good agreement between simulations and experiments. The computer model captures the main velocity profile features and the overall agreement is satisfactory. The profiles show a reduction in velocity upstream and acceleration on the sides. They also show that the downstream velocity profiles recover to its undisturbed shape faster for the porous case compared to the solid case.

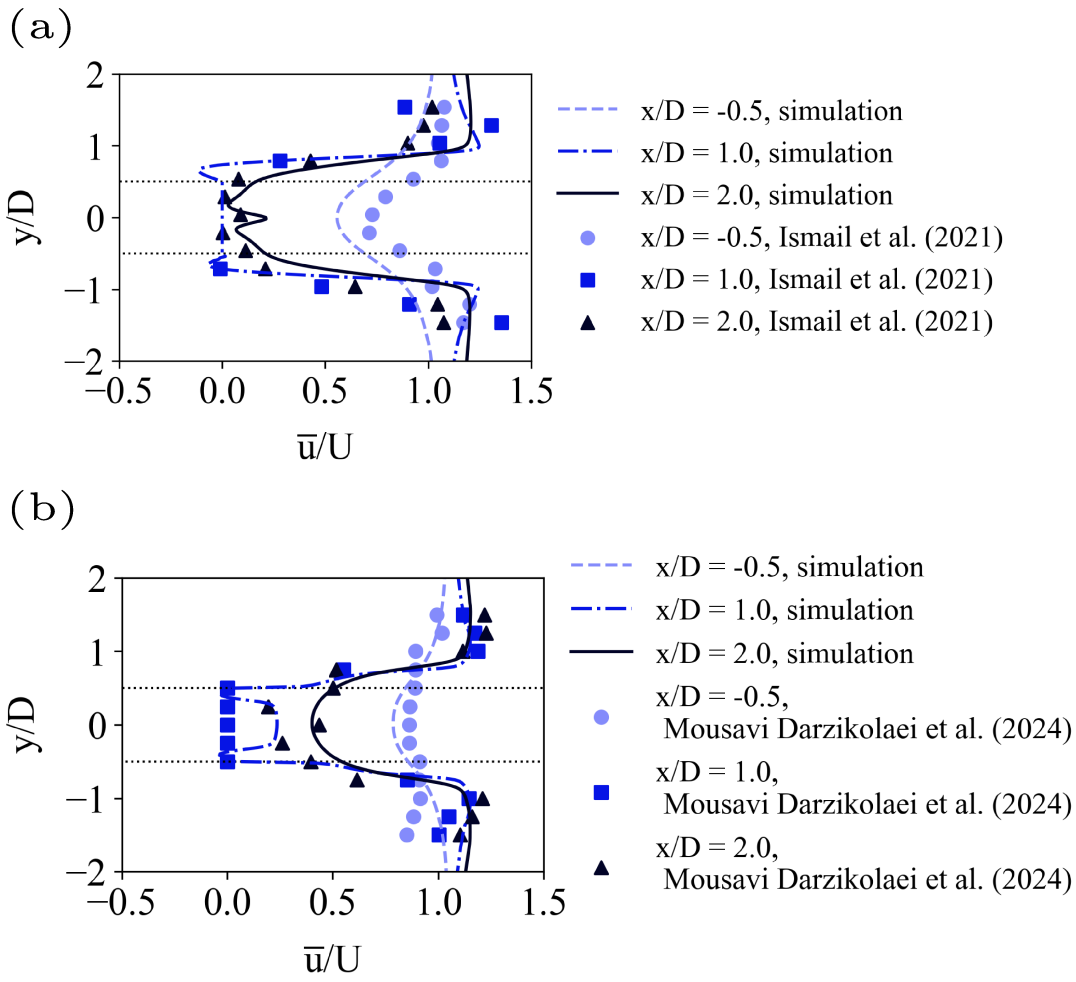

Figure 3.3. Streamwise velocity profile comparison. The velocity profile coordinates are specified in Figure 4.1.

The inflection point in the velocity profiles in the wake region is at $y/D = \pm 1$ for the solid case and $y/D = \pm 0.75$ for the porous case. The matching between simulation and experiment is better for the porous case compared to the solid case. This is largely due to less obstruction and therefore less turbulence in the porous case. In the porous case, turbulent structures and vortices are mostly smaller and more localized near the structure. Many of the vortices are shed behind each individual logs in ELJs. In contrast, the turbulence and vortices are larger and stronger around the solid structure. Additionally, for the solid case, the velocity profile upstream matches with the experiment better than downstream. Part of the reason is that the flow is severely blocked by the solid structure and the shear is stronger, which may be difficult to capture with the k-ω RANS model currently used.

3.5 Simulation Results

3.5.1 Three-Dimensional Coherent Structures

The observation is further illustrated by the Q-criterion vortices depicted in Figure 3.4 Hunt et al. [1988]. The Q-criterion is defined on the length scale of the structures. Figure 3.4 reveals the distinct flow dynamics around solid and porous structures. For the solid structure, horseshoe vortices form upstream and within the scour hole due to flow stagnation at the front face and separation at the edges. These vortices wrap around the base, inducing significant scour due to increased turbulence and flow acceleration. Conversely, the porous structure allows bleeding flow to penetrate, reducing the strength of the horseshoe vortices. However, smaller vortices can be seen at the upstream edge of the scour hole for the porous structure, located on the flat bed very close to the bed.

Downstream of the solid structure, large wake vortices are present, extending to elevations further from the bed and contributing to sediment transport away from the structure, deepening the scour hole and extending it downstream (Figures 3.4 a and c). In contrast, the porous structure disrupts the formation of large wake vortices, resulting in a more dispersed and smoother reattachment of flow to the downstream bed (Figures 3.4 b and d). This leads to reduced turbulence intensity and smaller, less coherent vortices close to the bed.

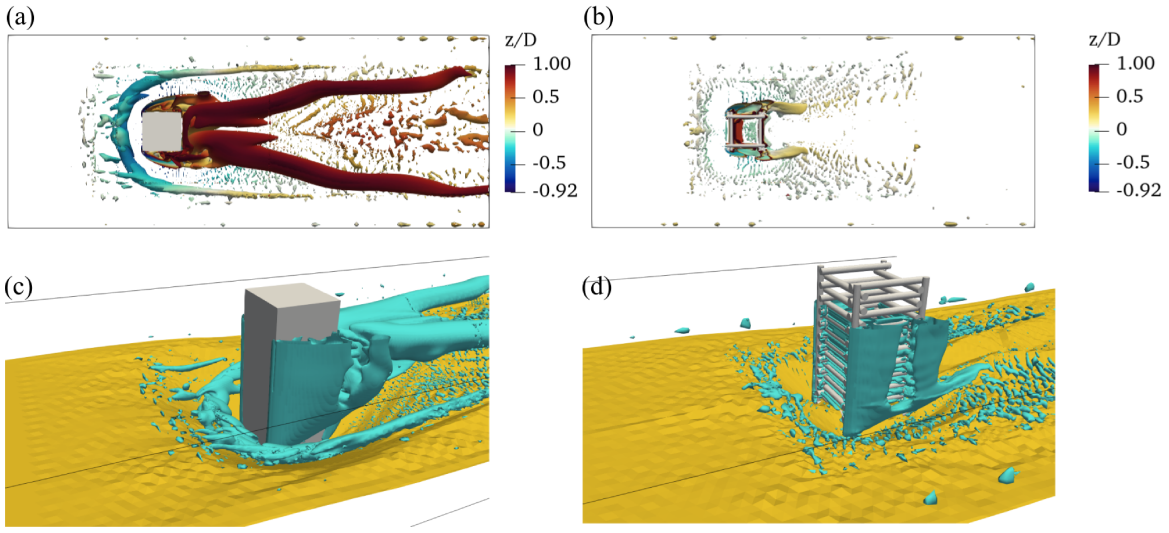

Figure 3.4. Vortical structures shown with Q = D (0.305 m) at equilibrium

3.5.2 Streamlines and Velocity Distributions on Horizontal Planes

Figure 3.5 displays the streamlines on the horizontal planes at mid-depth, illustrating both the initial stage and the equilibrium condition of the erodible bed. For the solid structure on the flat bed (initial stage), two counter-rotating vortices are observed in a relatively large recirculation region downstream of the pier, with reattachment occurring at $x/D = 5.5$. At the equilibrium stage, the vortices are pushed back closer to the structure, and the shear layers reattach around $x/D = 3$. Examining the porous structure, there are no wake vortices downstream of the structure. However, two counter-rotating vortices occur close to the front edge of the ELJs. These vortices are localized to the logs in the upstream and do not interact or reattach with each other. They are smaller than those in the solid case and their sizes scale with the individual logs that generate those voticies. The lateral redirection of flow in the shear layer is also reduced around the porous structure compared to the solid case. The differences can be observed approximately by examining the streamlines. In the solid case, the angle of the streamlines due to shear layer separation starts at about 30 degrees and reduces to 26 degrees at equilibrium. In contrast, in the porous case, the angles are smaller, ranging from 17 to 18 degrees.

These detailed flow features inside and around the porous structure are not visible in experiments due to measurement limitations.

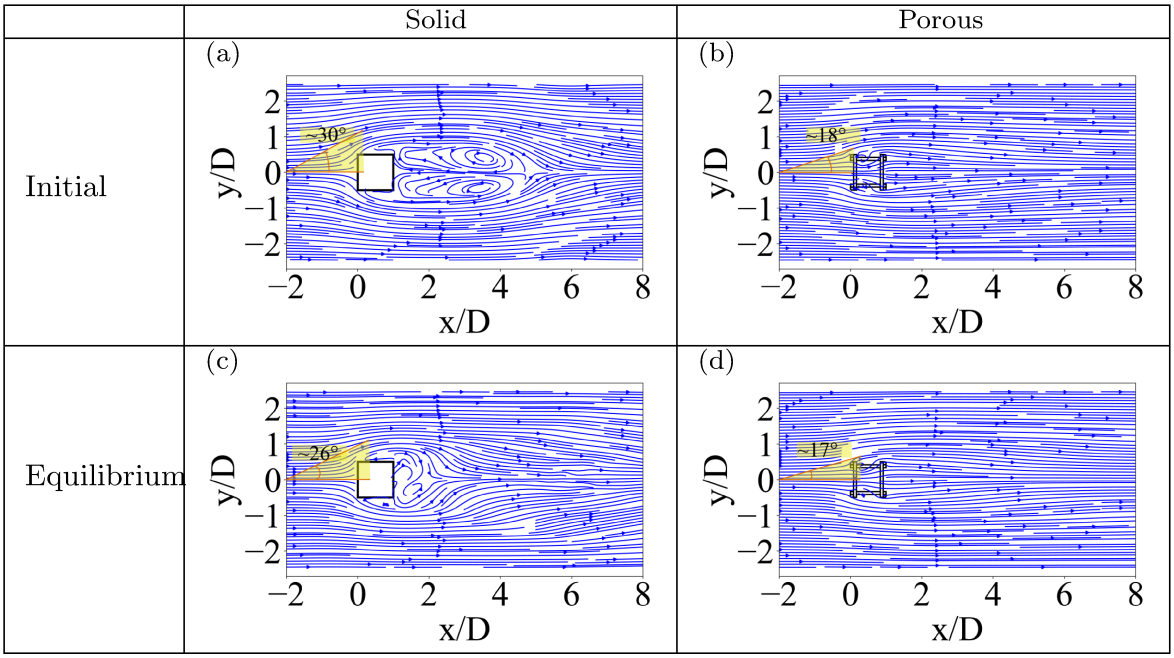

Figure 3.5. Streamlines on the mid-depth horizontal plane.

Figure 3.6 displays streamwise velocity contours at mid-depth and depth-averaged velocities for both the initial and equilibrium stages. The plots for the porous structure are shown in the right column, and those for the solid case are shown in the left column. At the initial stage, the mid-depth flow contours of streamwise velocity resemble the depth-averaged velocity. However, in the equilibrium stage the velocity distribution in the wake region becomes distinctly different specially for the solid case. This highlights the significant influence of bathymetric features on the flow characteristics.

The shear layer and velocity acceleration begin at the front edges of the structures and extend along the sides. At the initial stage, the shear layer is stronger for the solid structure compared to the porous one, and flow deceleration downstream of the structures is more pronounced for the solid structure. At the equilibrium stage, the strength of the shear layer decreases. Approaching the equilibrium stage, the differences between mid-depth and depth-averaged velocity fields become more pronounced, indicating that mid-depth measurements do not fully represent flow features at this stage. This also emphasizes the variation in velocity at different depths.

At equilibrium, the reduced velocity in the upstream is more noticeable when analyzing depth-averaged velocity and considering elevation changes. However, these velocity features are less apparent at mid-depth. Furthermore, the shear layers acceleration moves further from the structure and become less pronounced for at. When comparing the porous and solid flow fields, the size of the negative streamwise velocity region is larger for the solid structure which is in the order of solid structure length scale. In the porous case, the negative streamwise velocity region is localized around the logs, scaling with the individual log diameter in the cross-sectional direction and with the length of the logs in the longitudinal direction. Velocity deceleration extends far downstream for the porous structure compared to the solid, and the reattachment of shear layers is not observed within the domain of simulation for the porous structure. For the solid structure, the accelerated velocity is on the side of the structure in mid-depth contours, while flow acceleration occurs further downstream in the depth-averaged contours. Due to deposition, there is an acceleration in depth-averaged velocity downstream of the solid structure, which is not observed for the porous structure.

3.5.3 Streamlines and Vorticity Analysis on Vertical Planes

Flow field analysis on vertical planes also reveals key information for the hydrodynamics around porous structures. Figure 3.7 shows the streamlines on the vertical planes on the side edge of the structures (denoted as edge slice) and in the middle of the flume

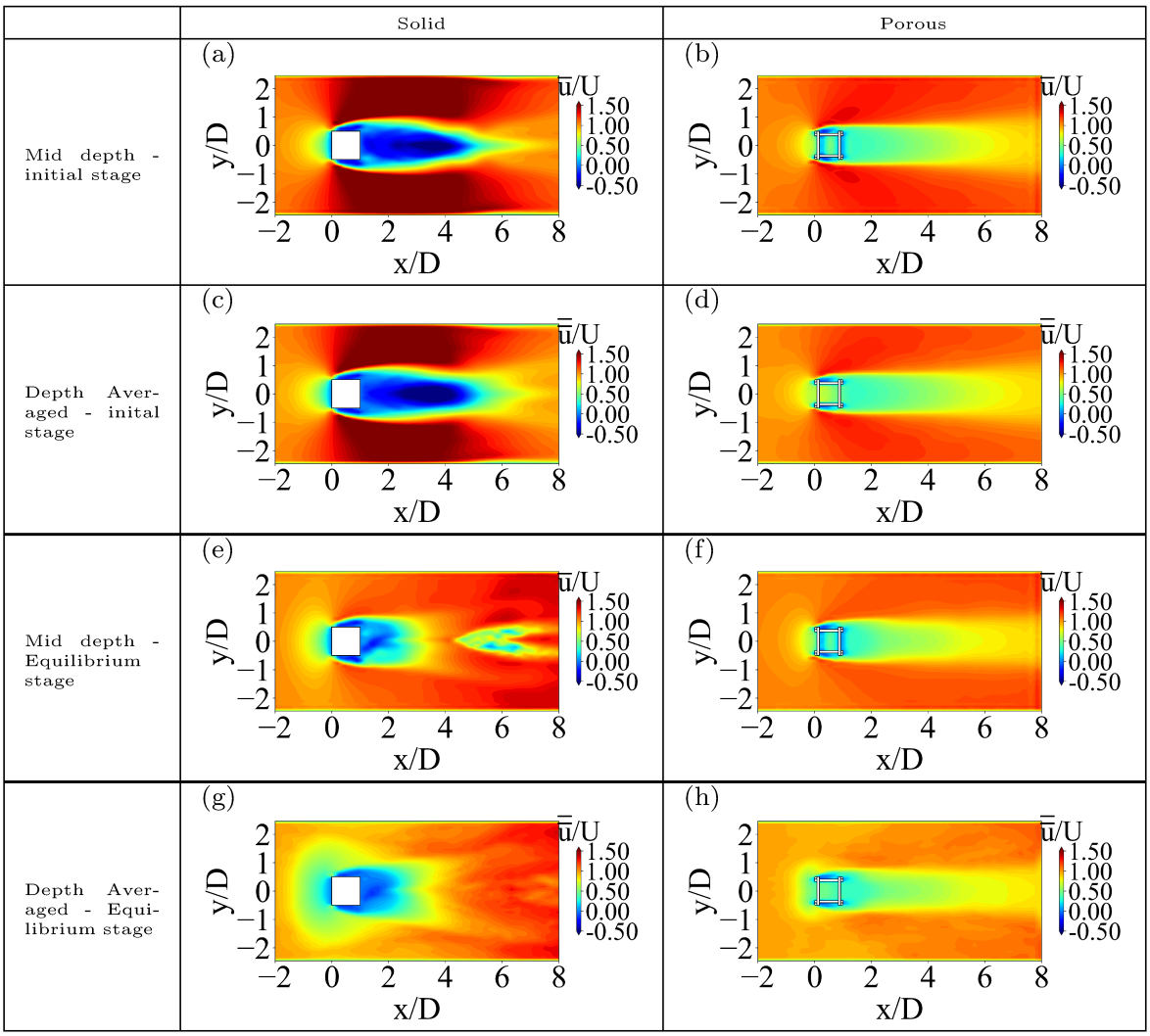

Figure 3.6. Comparison of streamwise velocity between solid and porous structures on the mid-depth plane. The depth-averaged streamwise velocity is also shown.

(denoted as centerline slice). In panels (a) and (b), the streamlines on the edge slice at the initial stage of scour for the solid and porous cases are shown, respectively. At the initial stage for the solid case, horseshoe vortices form around the structure, and a reversed flow is present directly within the wake. In panel (a), which is at $y/D = 0.5$, two flow recirculation zones can be observed: one at $x/D = 1$ and another further downstream at $x/D = 3$. For the porous case in panel (b), the reverse flow only reaches to the mid-length of ELJ and is suppressed before the downstream edge of the structure.

Panels (c) and (d) show the streamlines on the centerline slice, i.e., the vertical symmetry plane. For the solid case, the downflow is more pronounced compared to

that on the edge slice shown in panel (a). This is as expected and has been shown in many previous researches. The flow inflection point, where the reversed flow meets the streamlines in the direction of incoming flow, is observed at $x/D \approx 5.5$ and $z/D = 0.5$. For the porous case, due to the flow through the structure (bleeding flow), negligible downflow or reverse flow in front of or within the structure is observed.

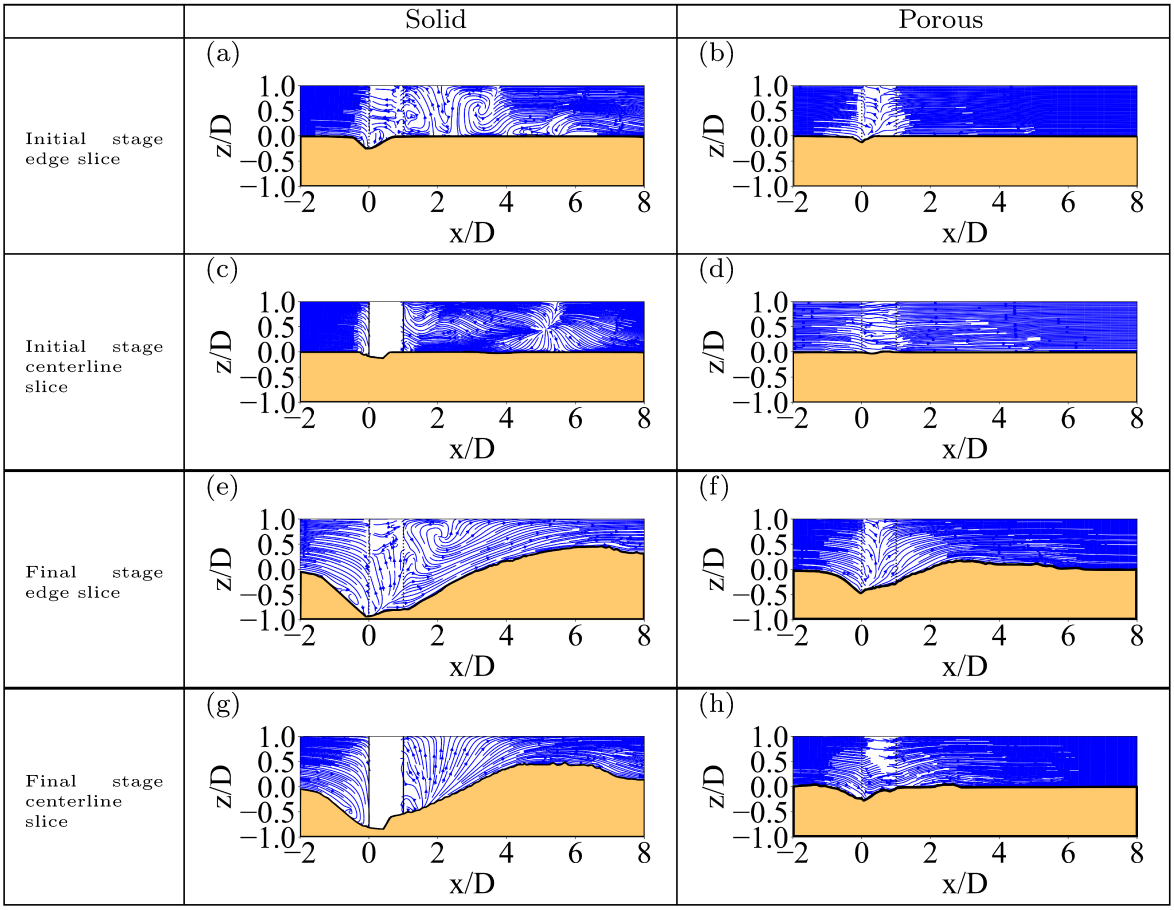

Figure 3.7. Flow streamlines in vertical slices

Panels (e) and (f) depict the streamlines at the equilibrium stage on the edge slices. For the solid case, the downflow recirculation zone size increases compared to the initial stage, resulting in a complete recirculation within the scour hole. At this stage, the strength of the downflow becomes insufficient to transport sediment from the bottom of the scour hole. For the porous case, the downflow is relatively weak. The streamlines move downward as they have more vertical space opened up by the scour hole; the streamlines now follow the contours of the bathymetric features. For instance, the deflection of the upward movement of streamlines in the downstream extends longitudinally from $x/D =$

1.5 at initial stage to $x/D = 2$.

In panels (g) and (h), the streamlines at the equilibrium stage on the centerline slices are shown. For the solid case, the inflection point is disrupted by a deposition peak compared to the initial stage. For the porous case, the bleeding flow through the structure from mid-depth to the top is reduced compared to the initial stage. The flow primarily passes through the bottom of the structure where erosion occurs, and the density of streamlines is higher in the lower depths.

For the porous structure on the edge slice, during both the initial and equilibrium stages, as shown in panels (b) and (f), when the flow encounters the front face of the structure, part of the flow moves downward while another part enters the ELJ. Inside the structure, as the downflow reaches the bed, it then moves upward. Some of this upward flow recirculates upstream, while the rest flows downstream and exits the ELJ. This behavior is distinct from that observed in the solid structure case. In the solid structure case, the absence of bleeding flow causes the entire downflow to recirculate upstream of the solid pier, generating vortices that result in a larger scour depth upstream.

Out-of-plane vorticity distributions on the two vertical planes are plotted in Figure 3.8. These vorticities provide another metric to compare and contrast the hydrodynamics around solid and porous structures at different scour stages.

At the initial stage and along the vertical symmetry plane ($y/D = 0$), the vorticity values are small, even in the upstream regions close to the structures. Negative vorticities, indicating downward and upstream flow in front of the structures, show that initially, it is only noticeable on the edge slice, as seen in panels (c) and (g). However, at the equilibrium stage, as shown in panel (e), vorticity is also visible on the centerline slice. This indicates that initially, the vortices forms at the edge of the structure. As time progresses, it develops along the centerline, suggesting that the scouring process starts at the edges and gradually extends toward the center of both solid and porous structures.

Directly downstream of the solid structure at the initial stage (Figure 3.8-a and c), large wake vortices can be observed. The strength of these vortices increases at the equilibrium stage as sediment deposition downstream of the structure confines the flow (Figure 3.8-e and g). This is in contrast with earlier stages when flow is less confined in the wake .

For the case of the porous structure, one the vertical symmetry plane, the vortices are localized around the lateral logs, dissipating inside the structure and re-emerging near the downstream lateral logs. Also, the vortices shed by the lateral logs are larger and stronger (Figure 3.8-b and f) around the upstream logs of the structure. In contrast,

for the edge slices, the vorticities are larger around the downstream lateral logs and the vortices are almost negligible around lateral logs that are perpendicular to the flow at the upstream of the structure. This is due to the shape complexity of the structure where lateral and longitudinal logs intersect. On the edge slice, there are vorticities close to the erodible bed that causes the initiation of sediment transport in this region. The size of these vortices, which are larger than the scale of individual logs, increases at the equilibrium stage, and more vorticity can be seen closer to the bed. In contrast, for the solid structure, there is a larger gap between the coordinates of the vortex formation and the equilibrium bed.

The comparison between the solid and porous structures in Figure 3.8 clearly demonstrates the influence of eddies shed inside the porous ELJ and the internal flow features on the formation of shear layer vortices. Analyzing the vorticity contours reveals that the vortices and flow dynamics within the ELJ substantially reduce the size of wake vortices, which are prominent in the case of the solid structure. Consequently, the bleeding flow within the porous ELJ impacts both the upstream downflow and the downstream wake-shedding vortices.

By comparing the initial and equilibrium stages of the streamlines and vortices, we highlight the limitations of previous studies that only modeled or conducted experiments without considering erodible beds, and only simulated flow on flat beds to draw conclusions on erosion and sediment transport. These studies are useful for understanding the initiation of sediment motion, the shape and size of vortices, and the flow patterns in the early stages. However, they do not accurately represent the long-term response of river or stream flow, especially as the sediment bed evolves. Thus, they are not informative for predicting long-term erosion and sediment transport dynamics.

3.5.4 Flow Partitioning Analysis

For porous hydraulic structures such as ELJs studied in this work, the main hydrodynamic feature is the bleeding flow through the structure. It is of great interest to quantify the partitioning of flow through and around these structures. Such partitioning is difficult to be computed with the sparse measurement data in flume experiments. However, it is relatively easy to do with computer models. The total flow discharge is made of three partitions, i.e., the flows in the zones of y/D within the ranges of (-2.5, -0.5), (-0.5, 0.5), and (0.5, 2.5). These zones correspond to the left, middle, and right section of the channel. The middle section has the same width of the structures. The flow partition is also calculated at different streamwise locations, i.e., x/D = -0.5, 0, 0.5, and 1. The flow

partitioning results shown in Figure 3.9 are at the scour equilibrium stage.

At x/D = -0.5, which is upstream with a distance of half structure size, the flow partitioning is similar for both solid and porous cases, and about 20% of the flow goes through the middle section. At $x/D = 0$ and 0.5, which are at streamwise locations inside the structures, approximately 10% of the flow goes through the porous structure. The corresponding flow partition at these locations for the solid case is obviously zero. For the ELJ studied in this work, the volumetic porosity is 0.85 and the surface porosity is 0.35. For an ELJ with different porous characteristics, the percentage of bleed flow will be different. Future research should investigate the functional relationship between flow partition and porosity. For the porous structure in this work, only 10% flow goes through. However, it cause significantly different hydrodynamics and morphological response.

3.6 Conclusions

This study successfully used a three-dimensional computational model to simulate the complex interactions of flow and sediment transport around porous and solid hydraulic structures. The results highlight the significant differences in flow dynamics and scour patterns between porous structures, such as Engineered Log Jams (ELJs), and traditional solid structures. The porous nature of ELJs allows for bleeding flow through the structure, leading to reduced flow blockage, modified coherent structure, smaller and more localized vortices, and weakened turbulent wake, which in turn influence sediment transport and the formation of bathymetric features. The model's ability to accurately capture these processes was validated against experimental data, showing good agreement in predicting velocity profiles and scour depth evolution.

The key findings of this research highlight the importance of considering the unique flow features introduced by porous structures in hydraulic engineering designs. The study also emphasizes the limitations of previous research that focused solely on solid structures or used simplified two-dimensional models, which do not fully capture the three-dimensional nature of flow and sediment transport processes. The insights gained from this study can inform the design and implementation of nature-based solutions for river restoration, ensuring the stability and longevity of in-stream structures. Future research should explore the functional relationships between flow partitioning and porosity, as well as the long-term morphological impacts of these structures in varying flow conditions.

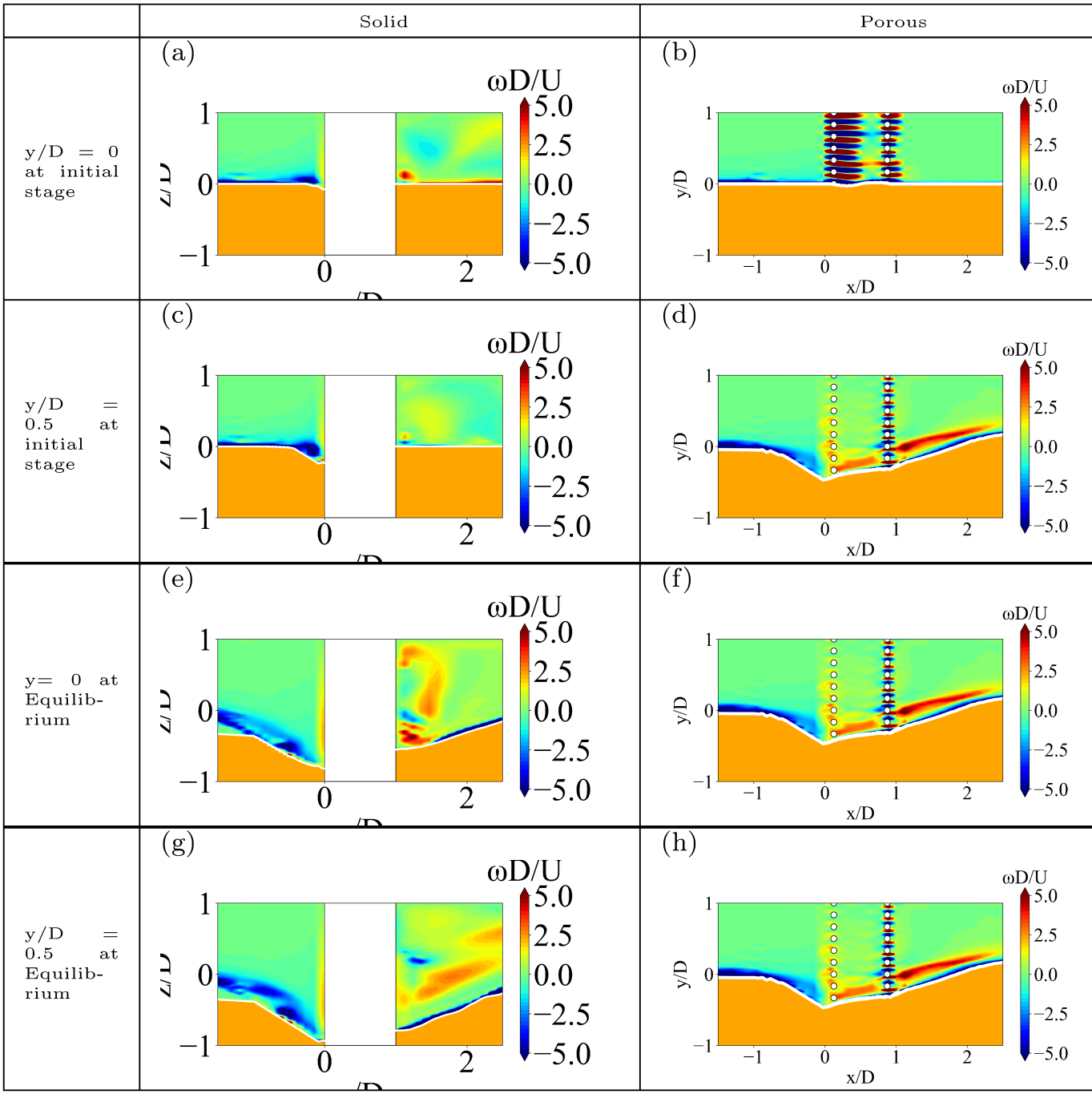

Figure 3.8. Out-of-plane vorticity distributions on vertical planes.

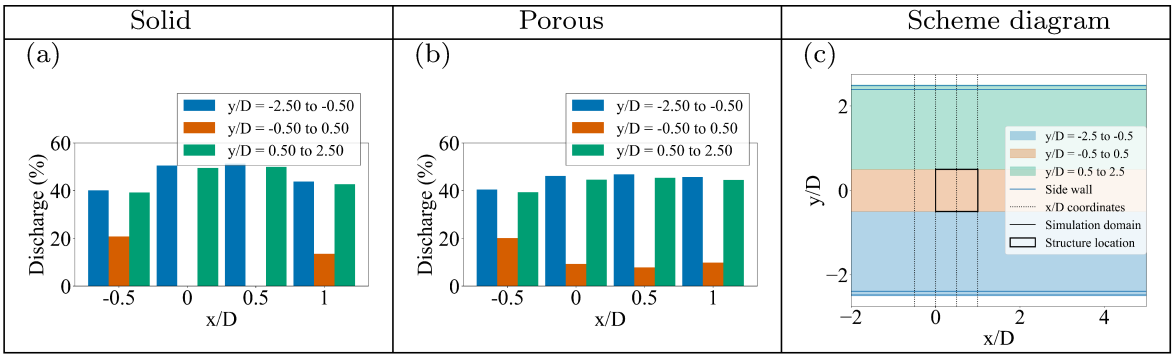

Figure 3.9. Discharge fraction through different regions of the lateral profile, (a) solid case, (b) porous case, and (c) Schematic diagram of the coordinates used for the discharge fraction calculation.

Chapter 4
Computational Model of Flow and Scour around Porous and Solid Hydraulic Structures: Part 2 - Sediment Transport

4.1 Introduction

Turbulent flow and scour around in-stream structures are crucial to the stability and longevity of these structures. In the previous part, the focus is on the flow and turbulence around and through the structures. In this part, the focus is on sediment transport and scour.

Using the high-fidelity 3D computational model *ibScourFoam*, two cases were simulated where a solid structure or a porous structure was placed in the middle of an open channel. The porous structure was an engineering log jam (ELJ) made of small wooden dowels. The key capability of the 3D model is the use of the immersed boundary (IB) method which can capture the evolution of the sediment bed and its interaction with the complex structures [Song et al., 2022c]. For the first time, critical information such as wall shear stress distribution, scour depth, shape, and erosion volume are available for in-depth analysis.

As shown in the previous part, the flow field around porous structures is very unique and different from those around solid structures. The bleeding flow, the flow through the porous structure, changes the coherent structures, wake zones and flow acceleration areas around ELJs. The percentage of the bleeding flow is only about 10% in the total

discharge. However, it create significant impact on both flow and sediment transport. Flow feature identification revealed the underlying mechanisms of sediment transport and the bathymetric features at different stages of scour evolution.

The second part of this study focuses on sediment movement drivers and dynamics, specifically the wall shear stress, scour patterns, and scour depth evolution around these structures. The local scour research community has long recognized that wall shear stress decreases as the scour hole develops. At equilibrium, the scour hole ceases its growth because the wall shear decrease below its critical value for sediment movement. This is the key concept of shear decay function [Melville, 1975], based on which a semi-theoretical model for scour depth evolution was proposed and evaluated in this work.

When an structure such as pier or pile is placed in a stream with an erodible bed, the flow accelerates around the structure, reaching maximum velocity at some location on the side of the structure. Behind the structure, wake vortices form, and the shedding frequency of the wake vortices is influenced by the Reynolds number. Due to the pressure gradient, stagnation downflow occurs upstream of the structure. As this downflow reaches the bed, it curls up and moves around the structure, forming a horseshoe vortex at the base and a surface roller at the free surface. Due to the hydrodynamic forcing on the bed, scour initiation occurs when the shear stress exceeds the critical shear stress, leading to scour on the sides of the structure [Gosselin, 1997, Richardson and Lagasse, 1999, Melville, 1975, Shen et al., 1965, Chiew, 1984]. Scour continues in areas where the shear stress exceeds the critical shear stress.

The temporal prediction of scour depth is crucial for analyzing the stability of river restoration structures and ensuring they remain sustainable and effective in achieving their restoration goals. Most previous studies on single or complex piers have focused on evaluating the maximum scour depth. Since the primary mechanism inducing scour may change at different stages of scour process, mathematical models for predicting the temporal evolution of scour depth is rare even for simple structures [Gosselin, 1997, Richardson and Lagasse, 1999]. It is also difficult to produce such predictive models due to the lack of detailed information such as wall shear stress. One such example is the purely empirical formula proposed in Mousavi Darzikolaei et al. [2024]. With a simple scaling analysis and using flume data, they showed that the scour depth asymptotically reaches equilibrium following a saturation-growth curve. The prediction satisfactorily matches with the experimental data from four idealized porous ELJs when they are placed on the side or the center of a flume. However, the generaliability of their empirical formula still needs proof.

One objective of this work is to use both physics and data to propose a semi-theoretical model for the time history of scour depth prediction that works for both solid and porous cases. Such simple model should be more generalizable because of the physical foundation. Once proved to be superior than pure empirical formulas, it can be used as a preliminary design tool for a wide range of field conditions.

Previous studies on the temporal evolution of scour have related the geometry of scour formation and sediment transport rate for bridge piers. The idea behind the analysis in this work to develop the semi-empirical model is also to use the knowledge of scour hole geometry and simplify it as a basic shape, such as a cone. This assumption has been previously used in studies such as Yanmaz and Altinbilek [1991] and Carstens [1966]. As more sediment is removed from the scour hole, its dimensions extend vertically, laterally, and longitudinally, eventually forming an inverted cone with an axis that coincides with the axis of the cylinder [Gosselin, 1997]. Reviews of other models can be found in Gosselin [1997] and Richardson and Lagasse [1999]. However, none of the previous models considered the porosity of in-stream structures and most of them focused on simple bridge piers.

For example Carstens [1966] developed a methodology that predicts the scour depth as a function of time based on the experimental data in Chabert [1956]. In their model, they defined sediment transport, Q_s, out of hole as a function of sediment number N_s, scour depth, and sediment grain geometry. Since the volume of the scour hole is already known based on its conical shape, it can be expressed as a function of scour depth. This analogy is adopted in the current work with some modifications. Carstens [1966] used the sediment number N_s to estimate the scour depth evolution. The limitation is that in their analysis, the sediment number, which has a similar form as shear stress ($N_s = \frac{v^2}{(s-1)gD_g}$), is considered fixed in time. However, based on the mechanism of scour, the hydrodynamic driving force for sediment motion changes over time as the bed shear decreases with increasing scour depth. In our research, to better capture shear decay, we use the well-known Shields parameter and allows it to change with time.

Shear stress inside scour hole has often been used as the metric for evaluating the amount of sediment moving out of scour hole [Johnson and McCuen, 1991]. However, accurately measuring or calculating shear stress is difficult in an evolving sediment bed compared to the well-established shear stress over a flat bed [Gosselin, 1997]. This is the reason that many previous researches used other flow variables, such as turbulent kinetic energy inside the scour hole [Gosselin, 1997]. Studies from Federal Highway Administration (FHWA) also found that hydraulic erosion capacity decreases as scour

depth increases, allowing for the estimation of erosion capacity based on scour depth [Annandale et al., 2001, Smith and Annandale, 1997]. FHWA uses a method for predicting scour based on hydraulic loads and the erosion resistance of soils. They modeled the shear decay using an exponential formula as $\tau/\tau_a = a\exp(-bV_s/B)$ [Shan et al., 2023]. In order for their model to match with data, they used a safety factor. In the current work, a rational function, instead of an exponential function, is used to better capture the shear stress decay.

Some other studies on the temporal prediction of scour used a different approach for calculating sediment transport, employing pickup functions such as those in LeFeuvre et al. [1970] and Van Rijn [1984]. For instance, Yanmaz and Altinbilek [1991] also assumed the shape of the scour hole to be an inverted right cone. However, for the sediment transport function, they used the pickup function published in LeFeuvre et al. [1970], which defines the rate of bed material removal per unit area per unit time. Their model, however, seemed only applicable within the range of their experimental data.

The rest of this paper is organized as follows. The computational model, simulation case setup, and flow field analysis will not be included because they have been presented in the previous part. Overall, two cases were simulated: one for a solid structure and the other for the porous ELJ structure (Figure 4.1). This part will present the simulated erodible bed and bathymetry, bed profiles, wall shear stress distribution and statistics, and the temporal analysis and modeling for scour development. This paper is then concluded with a summary.

4.2 Results for Sediment Transport

4.2.1 Erodible Bed and Bathymetry

The *ibScourFoam* model produced detailed bed evolution process and the bathymetry at every simulation time step. The resulted dataset, especially for the sediment transport quantities, are very valuable for detailed analysis, which is difficult, if not impossible, to do in flume experiments. The bathymetry contours for solid and porous structures cases at three representative stages of evolution are shown in Figure 4.2. Stage 1, 2, and 3 corresponds to early, middle, and equilibrium stage, respectively. Animations of the scour process can be found in the Supplementary Information. The equilibrium bathymetry from flume experiments are shown in panels (g) and (h).

The simulated evolution of the scour clearly shows the following stages with distinct

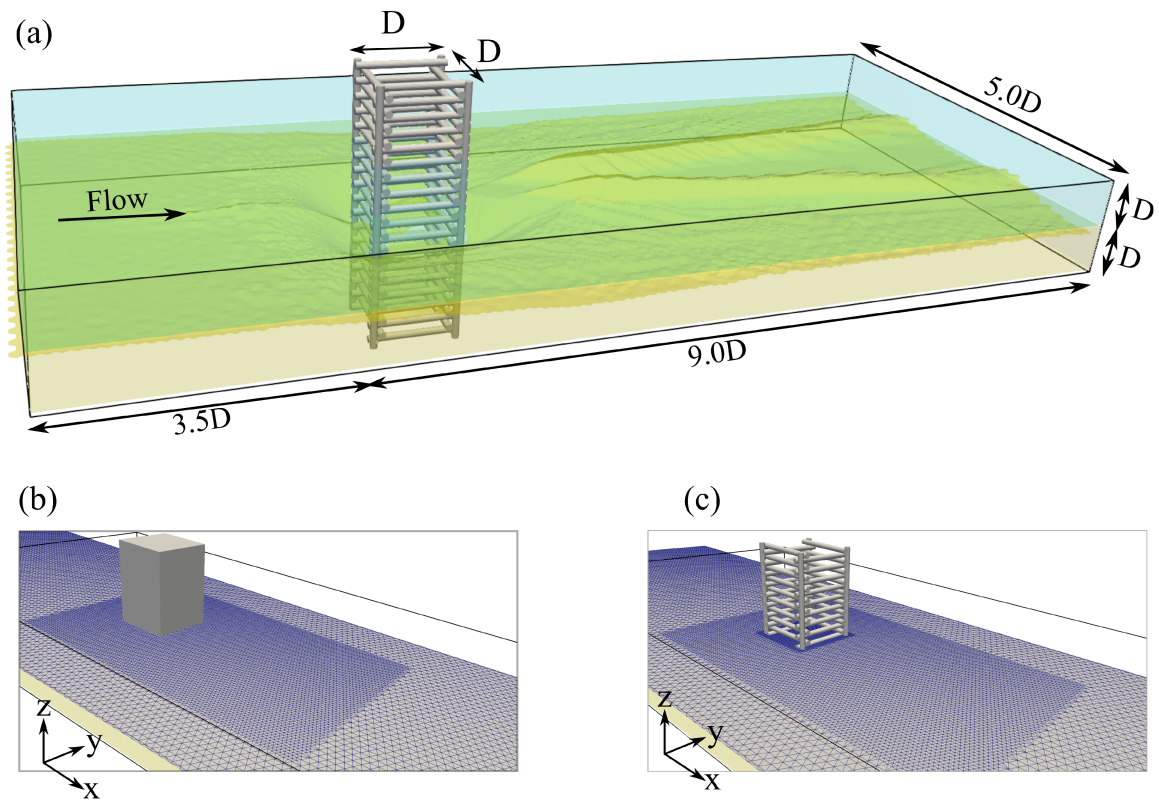

Figure 4.1. Computational domain

sediment transport features: Initially, scour occurs at the edges of both the solid and the porous structures due to flow contraction and the formation of shear layers at the corners of the structures. The depth, width, and length of the scour are larger for the solid pier compared to the porous pier at this initial stage. As the erosion process continues, the scour deepens and elongates downstream, resulting in a larger horseshoe vortex as water flows into the scour hole. In addition to the scour holes, two deposition bars start to form downstream of the scour holes on the sides of the structures. The scour holes extend both downstream along the sides of the structure and upstream towards the centerline of the structure until the two scour holes on both sides merge and form one big hole. Once the two scour holes merge, the horseshoe vortices are enlarged due to the more available space. After the merged scour hole exposes the total length of the sides of the structures, the scour hole moves towards the centerline of the structures in the downstream. Eventually, horse-shoe shaped scour holes are formed around both structures.

For the porous structure case, the bleeding flow through the structure reduces the

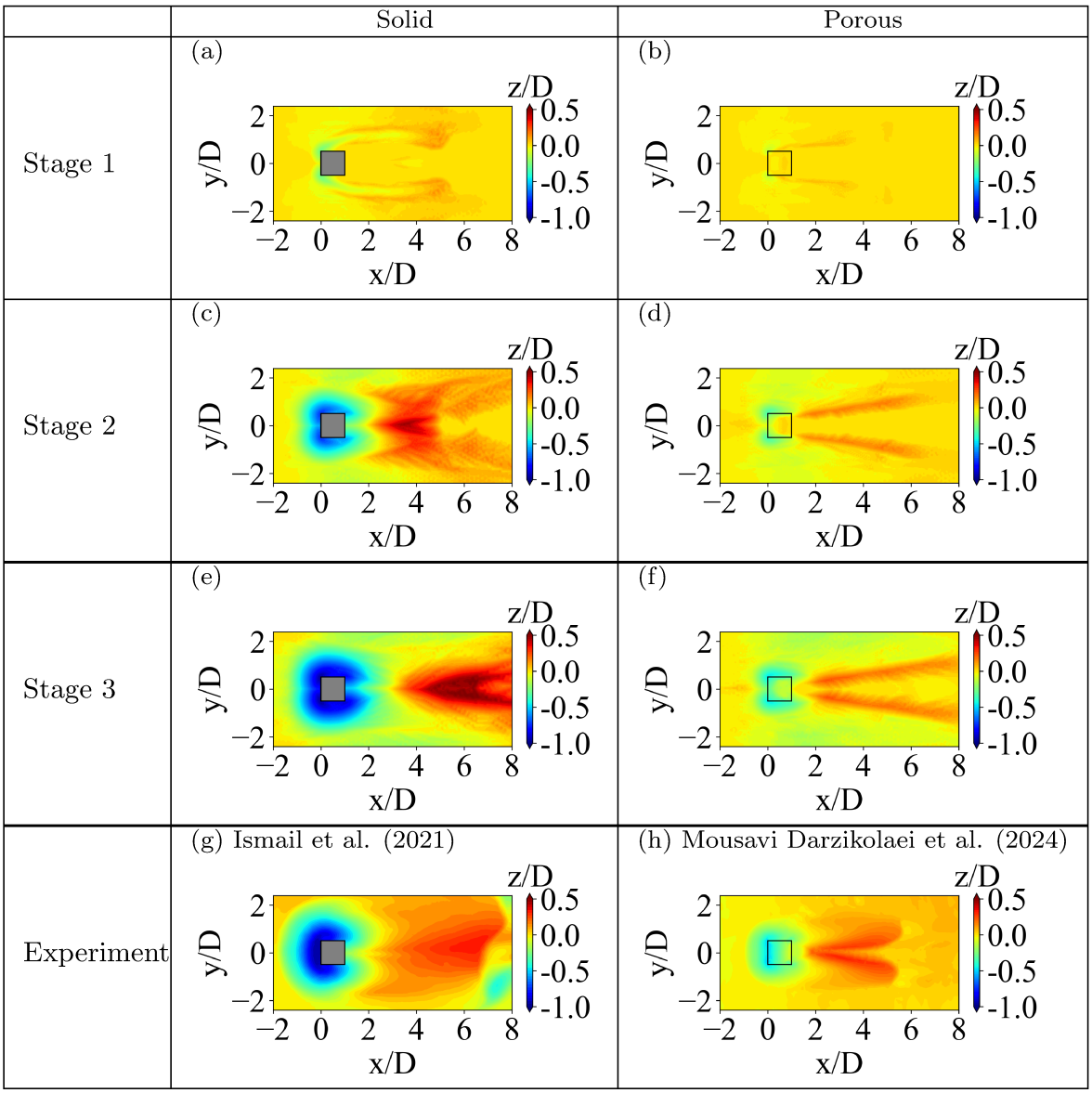

Figure 4.2. Bathymetry contours at different stage of scour and comparison with experiments

reattachment of flow in the downstream wake, causing the horseshoe shape of the scour hole to be less defined compared to the solid structure case. Subsequently, sediment is moved further downstream of the porous structure. The wake vortices and shear layer have larger intensity for the solid case than the porous one. As a result, the two deposition bars merge in the solid case but not in the porous case.

At the equilibrium stage, Figure 4.2 shows that the simulations captured the maximum scour depth for both solid and porous structure cases. The shape and extent of the scour holes are in good agreement between simulations and experiments. Along the streamwise

centerline, the formation of the scour extension is not as pronounced in the simulation compared to the experiment. The extensive erosion around the solid obstruction is driven by more significant blockage effect, intense turbulence and strong vortices. In contrast, the porous structure has a lower impact on the bathymetry.

For the solid case, the maximum deposition bar is around $x/D = 7$ in both the experiment and the simulation. In the porous case, the two deposition bars observed in the experiment are also captured in the simulation. For the porous case, the deposition bar extends further in the streamwise direction than in the experiments. This is likely because the mesh is coarser in this region, and the details of the recirculation of the flow downstream of the deposition bar, which prevent the deposition bar from being washed away, are not captured. The height of the deposition bars for the solid structure is larger in the simulation than in the experiment, and the sediments are more pushed towards the centerline in the simulation. This discrepancy arises because the RANS model cannot capture all the details of the very complex flow field downstream of the structure. For example in experiments, sediment movement in the wake region was observed to move only occasionally and sporadically during the later stage. These seemly random movement of sediment particles is mostly driven by turbulent eddies, which can not be captured by RANS models.

4.2.2 Bathymetric Profiles

The bathymetric evolution is further analyzed with longitudinal profiles on different vertical planes. These vertical planes are are the symmetry plane ($y/D = 0$), the plane along the side edge of structure ($y/D = 0.5$), and the plane at $y/D = 1$ which is half structure size away from the edge. In addition, the laterally averaged bed elevation profiles along the width of the flume are also computed (termed width-averaged profiles). All these profiles from simulations and experiments are plotted in Figure 4.3.

For the solid case on the symmetry slice, the maximum scour depth at the initial stage occurs at $x/D = 0$, which is at the upstream base of the structure. Changes in both scour and deposition are negligible at Stage 1 ($t \approx 500$ s) on the symmetry slice (Figure 4.3-a). However, erosion on the edge slice ($y/D = 0.5$) is more noticeable (Figure 4.3-c). This is because the scour starts around the upstream corners. As time progresses, the maximum scour on the symmetry slice and the edge slice remains near the upstream front face of the solid pier. For the $y/D = 1.0$ slice which is half a structure size away from the structure, the maximum scour depth starts at $x/D \simeq 1$ (Figure 4.3-e), which is the location close to the downstream face of the structure. Interestingly, as time

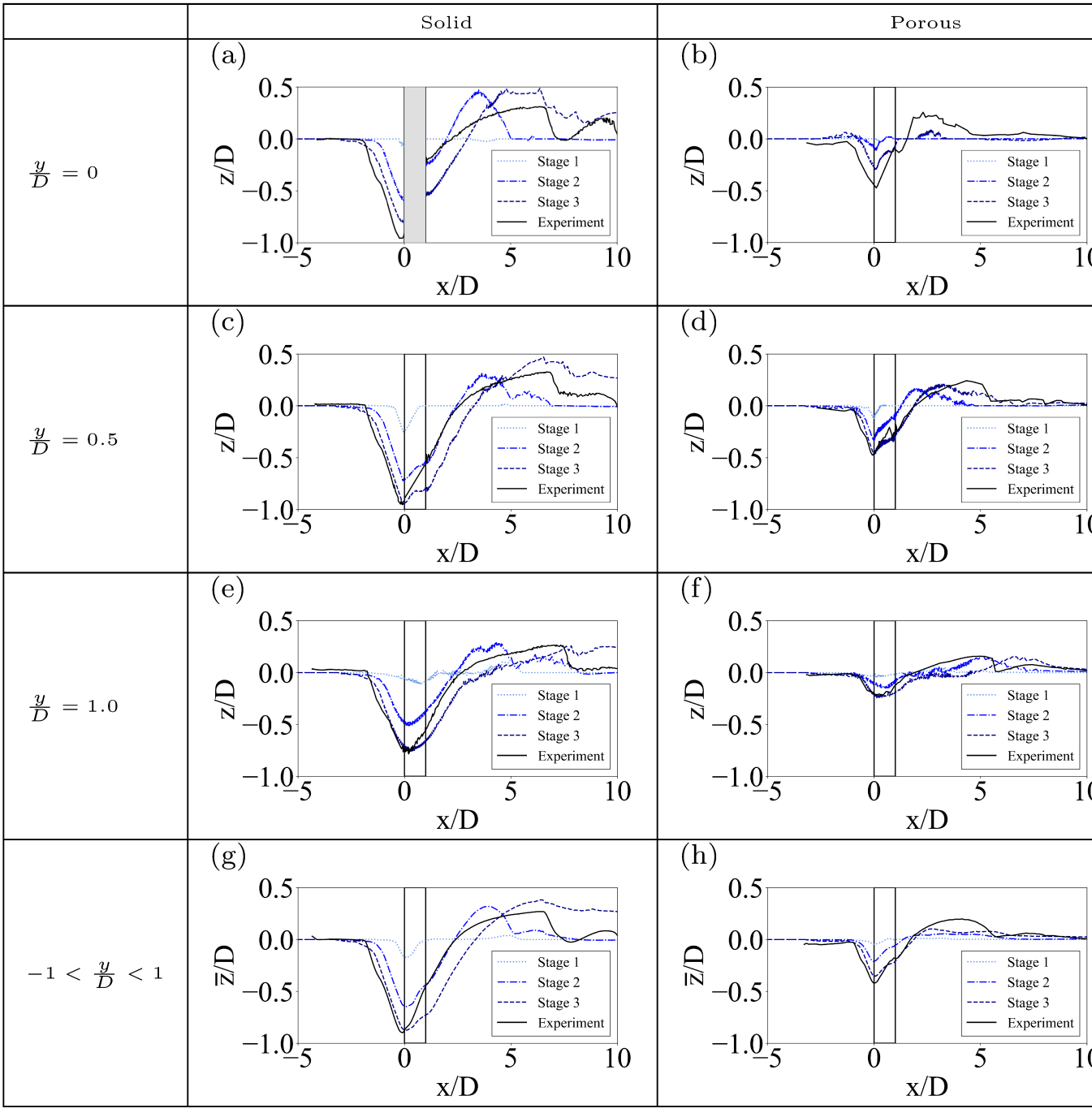

Figure 4.3. Longitudinal bathymetry profiles on different vertical planes.

progresses, the max scour depth on this profile move upstream.

At the equilibrium stage, on the edge slice ($y/D = 0.5$), the depth of scour in the simulation closely matches with the experiment on the upstream side (Stage 3). However, the scour hole downstream is overestimated for the solid case. On the $y/D = 1$ slice, the simulation also matches the maximum scour depth observed in the experiments.

For all three profiles on the three slices, the deposition bar behind the solid structure moves downstream over time. The deposition peak location x/D is within the range of 5 to 7 for $y/D = 0$, 6 for $y/D = 0.5$, and 8 for $y/D = 1$.

For the porous case on the symmetry slice, the maximum scour depth occurs at $x/D = 0$ at all stages. The evolution of scour within the ELJ is also visible. Two local minima can be seen on this slice: one at $x/D = 0$ and another closer to the downstream face of the ELJ at $x/D = 1$. The existence of two local minima is unique for the porous case.

On the edge slice ($y/D = 0.5$), the maximum scour depth is at the front face, similar to the solid case. From Stage 2 to equilibrium, the deposition bar moves downstream. On the $y/D = 1$ slice, the maximum scour depth location migrates from the front face to the downstream face of the porous structure. At equilibrium, on the symmetry slice, both the deposition bar height and scour depth are underestimated in the simulation compared to the experiment. Given that two deposition bars were observed from the bathymetry contours in Figure 4.2, this suggests that the locations of the deposition bars are not well simulated in the lateral direction. Nonetheless, the simulation accurately captures the maximum scour depth and scour hole shape on the edge slice ($y/D = 0.5$), and the deposition bar matches better with the experiment. In addition, the maximum scour depth and its location are well captured in the simulation for the porous case on the $y/D = 1$ slice.

The scour depth is underestimated on the symmetry slice for both solid and porous cases, and the deposition bar is not accurately captured due to complex flow features in the wake region. Comparing the solid and porous cases, the scour hole has steeper face in the solid structure and is more rounded in the porous structure. The roundness is due to the less abruptness of the flow blockage effect due to the porous structure. Additionally, the scour hole face appears more steeply inclined in the experiment than in the simulation. Future research needs to investigate whether this is due to the sand slide model and its diffusion parameter used in this work.

The width-averaged longitudinal profiles are also compared in Figure 4.2. The result shows that the profile for the porous case closely matches with the experiment at equilibrium. For the solid structure, the profile aligns well with the experiment upstream

but overestimates the average scour depth downstream. Nonetheless, the width-averaged profiles are in good agreement with experiments and can be used for further analysis, making them suitable for sediment transport analysis to predict scour depth compared with maximum values or on specific slices. Comparing different stages, the maximum averaged scour depth increases, and the average scour hole grows downstream. Initially, deposition occurs around $x/D = 5$, forming a higher deposition bar for the solid structure that moves downstream over time. For the porous structure, the average deposition peak is not pushed downstream as much as in the solid case. Instead, it is more uniformly distributed, with its height increasing over time. This is due to the bleeding flow that blows sediment particles downstream and limits the deposition in the wake.

4.2.3 Wall Shear Stress

4.2.3.1 Spatial Distributions of Wall Shear Stress

In sediment transport, wall shear stress is a proxy for the driving force for sediment particle movement. The *ibScourFoam* computes wall shear stress on the sediment bed at each time step, which can be used to the dynamics of scour evolution. To do this, the amplification factor of wall shear stress, τ/τ_o, is plotted in Figure 4.4. Here, τ_0 is the background wall shear. Both cases simulated in this work is in the clear-water scour regime, which means the background wall shear τ_0 is not capable of moving sediment. The existence of structures locally amplifies the wall shear and cause local scour. In Figure 4.4, different rows correspond to different stages of scour, which are the same as those in in Figure 4.2.

As observed in the beginning of sediment transport (Figure 4.2 a and b), the shear stress for the solid structure is significantly higher at the upstream corner and along the shear layer compared to the porous structure. In the porous case, the amplification factor is more evenly distributed around the structure. At this initial stage, the higher amplification occurs away from the side of the structure around $y/D = \pm\ 1$ for the solid case. For the porous case, the highest amplification factor is right at the edge of the structure and not away from it. This leads to an initial scour hole and deposition extending downstream on both sides as shown in Figure 4.2.

At Stage 2 ($t = 500$ s), the wall shear amplification for the solid case can be seen in zones both adjacent to the structure and in the wake. The higher amplification zone moves closer to the structure and extends toward the center line. This results in the formation of a scour hole closer to the structure, exposing more of the structural surface

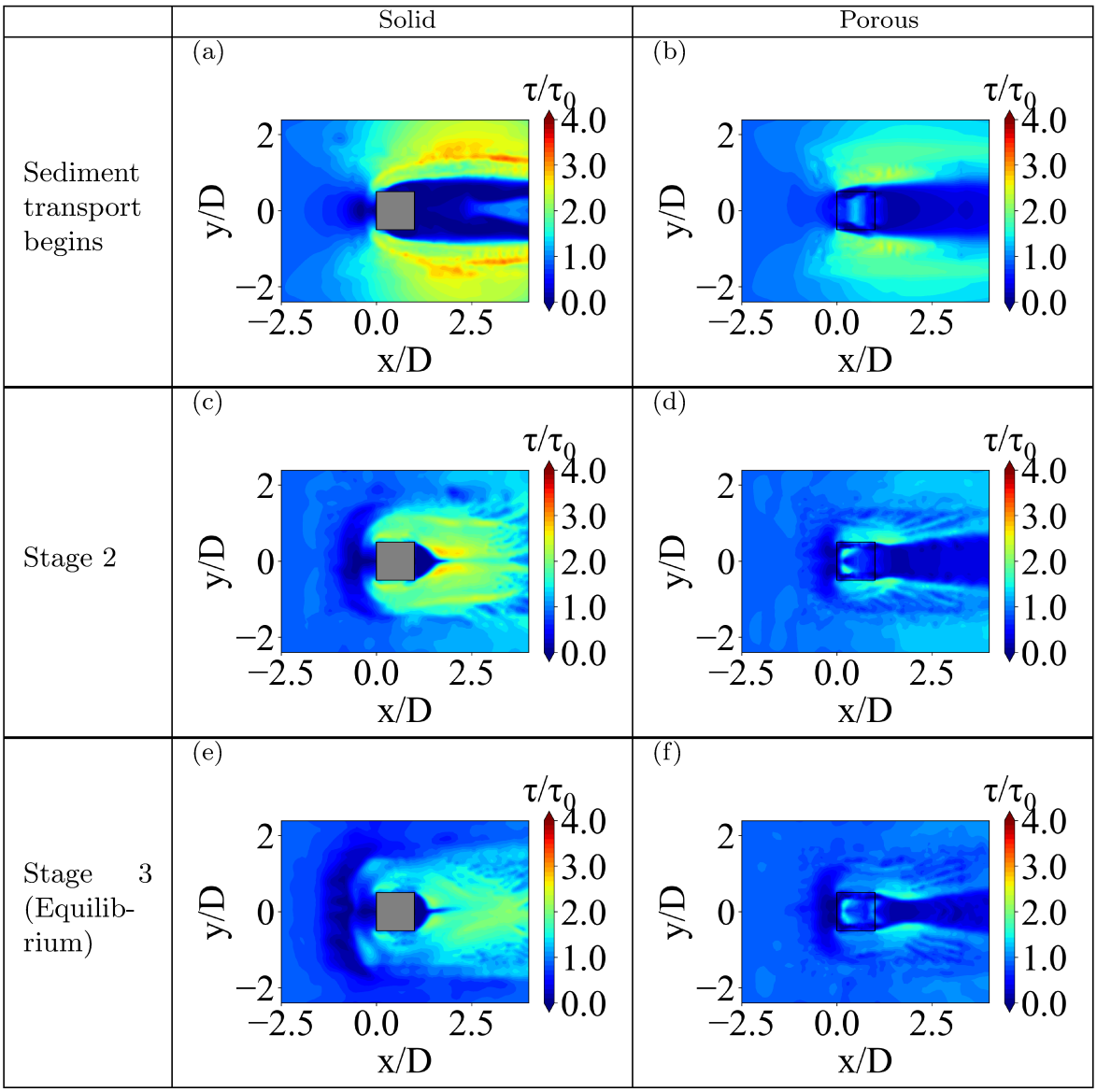

Figure 4.4. Wall shear stress contours on sediment bed.

to the flow. As the amplified WSS extends toward the centerline, a horseshoe-shaped scour hole extending to the downstream side is formed, as seen in the bathymetric contours shown in Figure 4.2.

In contrast, at Stage 2 for the porous structure, the downstream wake area has very low wall shear. Inside the porous structure, two high shear zones can be observed near the corners. The high shear within the structure causes internal erosion and moves sediment particles out of the structure, which was observed in the experiment.

At equilibrium, when the scour hole is fully formed, the wall shear within the scour is

mostly below the critical wall shear and the scour hole development essentially stops. At this stage, the wall shear stress becomes more uniform for both cases. In addition, a zone of zero wall shear can be seen upstream of both structure near x/D = -0.5. For the porous case, high wall shear can be seen only in the deposition areas that results in pushing the deposition towards the centerline in the downstream.

The solid case generates higher shear along the side edges due to greater flow contraction. In contrast, the porous structure allows flow to pass through it, resulting in lower shear stress. Thus, the solid structure creates a more concentrated region of high shear stress, which leads to a pronounced scour pattern. Conversely, the porous structure allows for a more diffused stress distribution, which is the direct evidence that porosity plays a crucial role in reducing localized erosion and promoting a more stable equilibrium state.

4.2.3.2 Statistical Analysis of Wall Shear Stress

In addition to its spatial distributions, statistical analysis was also performed to further analyze the driving force dynamics. Figure 4.5 shows the probability distribution function (PDF) of wall shear amplification at different stages of scour. The statistics was based only on the wall shear inside the scour hole. In the figure, "Stage 0" means the beginning of scour simulation, which is the result of the pre-simulation for hydrodynamics only. The statistics shown here may be only applicable to the cases simulated in this work. Nonetheless, it provides key insights.

For the solid case at Stage 0, the distribution is bi-modal with two distinct peaks: one near $\tau/\tau_0 = 1$ and the second at a higher value around 2.2. This second peak is responsible for moving sediment. As time progresses, the higher peak diminishes, and the distribution gradually shifts towards a single peak near $\tau/\tau_0 = 1$. This indicates that the wall shear stress stabilizes over time and that equilibrium has been reached.

For the porous case, similar behavior is observed with the initial distribution being bi-modal and the second peak that is responsible for erosion diminishing over time. At the equilibrium, the distribution becomes unimodal, with the mode consistently close to $\tau/\tau_0 = 1$ when the scour ceases.

The spread (width) and shape of the PDFs provide valuable insights into the variability of shear stress distribution. As time progresses, the decreasing spread of a PDF indicates a reduction in the variability of wall shear stress. Comparing the porous and solid cases, the porous case exhibits less variability in wall shear stress, meaning that the stress is more evenly distributed, contributing to a more stable and uniform flow within the scour

(a)

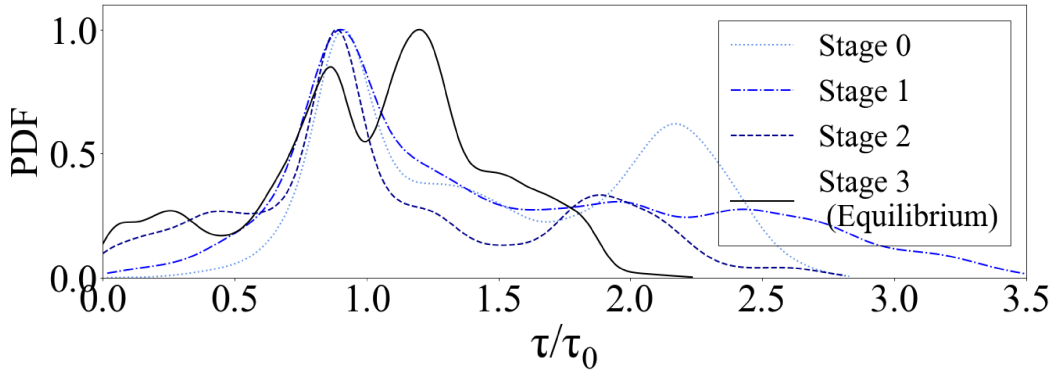

(b)

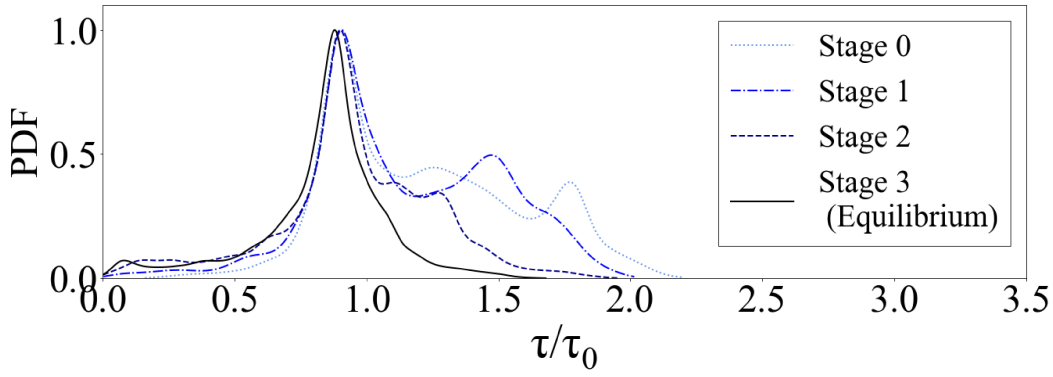

Figure 4.5. Wall shear stress probability distributions: (a) Solid case, (b) Porous case.

hole. At the beginning of the simulation, the bi-modal distribution indicates significant spatial complexity in sediment transport, with varying shear stress values across different regions.

Porosity significantly impacts the shape and evolution of the wall shear stress distribution. In the porous case, the distribution transitions more quickly to a unimodal state, suggesting that porosity facilitates a faster stabilization of wall shear stress. Additionally, the variability of wall shear stress is generally lower in the porous case, as indicated by the narrower PDF. This implies that the wall shear stress is more diffused and uniformly distributed within the scour hole for the porous case.

4.2.4 Temporal Analysis of Scour Development

4.2.4.1 Temporal Evolution of Wall Shear

Wall shear within a scour hole usually decreases with time as the scour approaches equilibrium. Figure 4.6 illustrates the mean Shields number inside scour holes over time for both solid and porous cases. In the figure, the time is made dimensionless with a time scale $t_0 = L/U$ where L is the size of structure and U is the average incoming flow velocity.

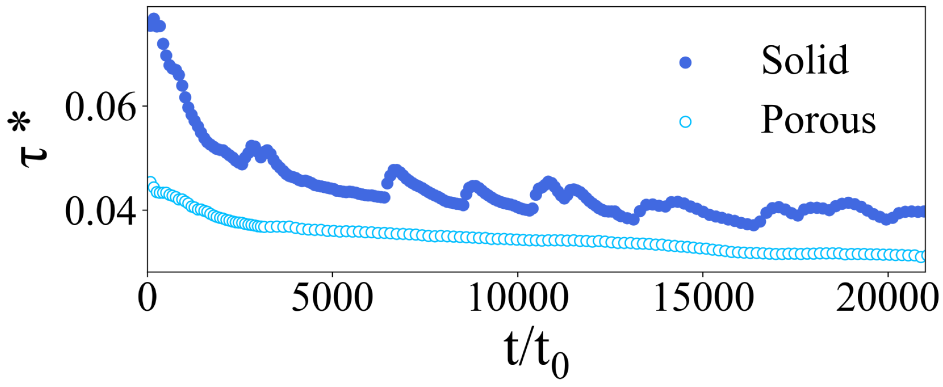

Figure 4.6. Temporal evolution of Shields number inside scour holes.

For the solid case, initial Shields number values are higher, with a general declining trend marked by periodic oscillations. In contrast, the porous structure maintains lower and more stable shear stress values, with a smoother decrease over time. This suggests that the solid case experiences more intense and variable turbulence and wall shear stress within the scour hole compared to the porous case. Upon investigation, the fluctuations are found to be physical in nature rather than due to numerical instability. The scour animation provided in the Supplementary Information shows that for the solid case there are more episodes of sand slide and the collapse of the bed which contribute to these fluctuations.

4.2.4.2 Temporal Evolution of Scour

Figure 4.7 (a) and (b) present the evolution of scour depth and scour volume over time. The scour volume is the amount of the sediment moved out of the scour hole. Both scour depth and volume demonstrate a consistent increase over time. The scour depths are non-dimensionalized by the equilibrium scour depth S_e from experiments in Ismail et al. [2021] and Mousavi Darzikolaei et al. [2024]. While the instantaneous wall shear

shows significant fluctuations for the solid case, its temporal evolution of scour depth and volume is much smoother.

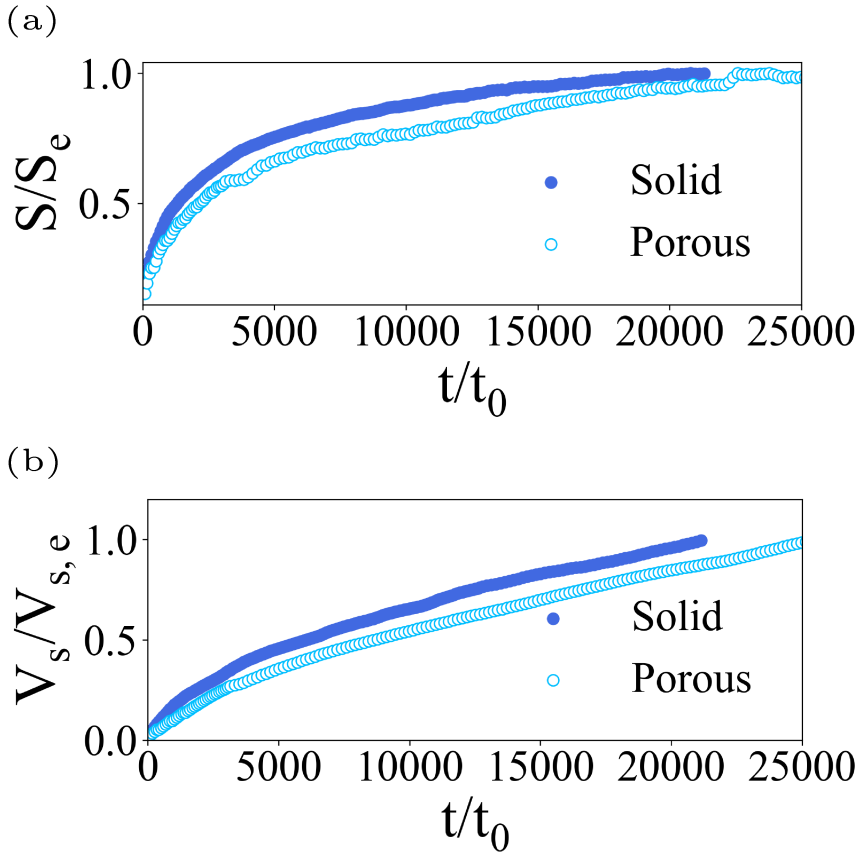

Figure 4.7. Temporal evolution of scour depth and volume.

The trend of the dimensionless scour depth indicates that the initial rate of increase in scour depth for the solid case is faster compared to the porous case. However, both cases approach a dimensionless value of 1 as they reach equilibrium, with the rate of increase diminishing and stabilizing over time. The volume of scour is also lower for the porous case compared to the solid case, highlighting the effect of porosity and bleeding flow on scour formation.

4.2.4.3 Shear Decay Function

As scour develops and the size of the scour hole increases, the flow within the scour hole slows down and the wall shear decreases until its critical value for sediment movement. This decay process of wall shear has been long recognized. Previously, it is effectively impossible to directly derive such shear decay function because wall shear is extremely

hard to measure during experiments. For the first time in this work, the availability of wall shear distribution and scour process makes the derivation of the shear decay function possible. This section shows such derivation.

Figure 4.8 shows the relationship between the Shields number and the scour depth. The relationship demonstrates that as time progresses, the Shields number decreases while the scour depth increases. This inverse relationship occurs because increased scour depth reduces the flow's capacity to transport materials out of the scour hole.

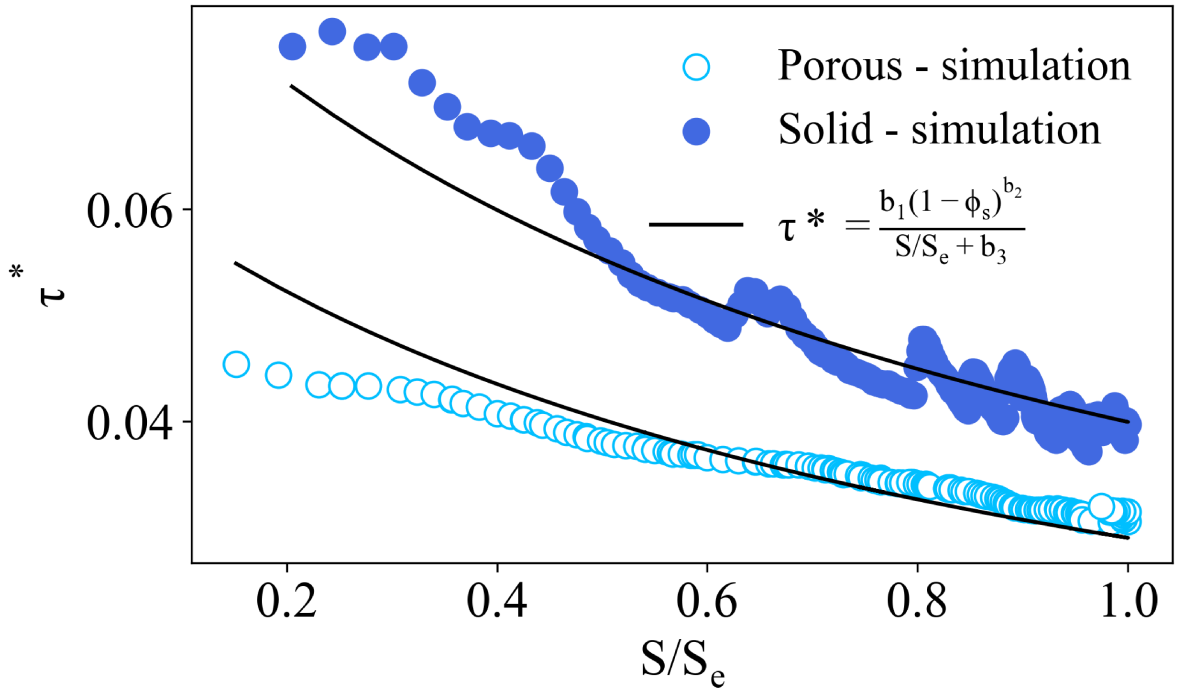

Figure 4.8. The relationship between the Shields number and scour depth.

To model the shear decay and also considering the effect of porosity, a rational function of the following form is proposed:

$$\tau^* = \frac{b_1 \cdot (1-\phi_s)^{b_2}}{\frac{S}{S_e} + b_3} \tag{4.1}$$

where b_1, b_2, and b_3 are fitting coefficients. This mathematical form of the function considers the physics and the asymptotic behavior. As scour reaches equilibrium, i.e., S/S_e approaches 1.0, the Shields number τ^* approaches a constant. The light and blue color markers in Figure 4.8 compare the effects of porosity in the porous and solid simulations. The Shields number is consistently higher in the solid case than in the porous case by a nearly constant multiplier. To capture this difference, a power function

of porosity is incorporated in the numerator of the equation relating the Shields number to scour depth. When porosity is zero (solid case), the multiplier $(1-\phi_s)^{b_2}$ is 1. When porosity is present, the Shields number is reduced by a factor dependent on porosity, which is a nonlinear relationship.

For a more generalized fitting approach, the solid and porous data were combined and a unified formula was sought. The fitting coefficients were derived from the simulation data, resulting in the following values for both cases: $b_1 = 0.07$, $b_2 = 0.74$, and $b_3 = 0.8$. With the fitted coefficients, the proposed shear decay functions for both cases are plotted against the simulation data in Figure 4.8. In general, the fitted shear decay function satisfactorily matches with data.

4.2.4.4 A Theoretical Model for Scour Depth Prediction

The purpose of this section is to provide a simple mathematical model to predict the temporal evolution of scour depth. This model is built upon the shear decay function proposed before and the assumption that the scour hole shape is an inverted cone [Carstens, 1966, Melville, 1975, Yanmaz and Altinbilek, 1991] The conceptual cone-shaped scour hole used in this study is shown in Figure 4.9. For a cone-shaped scour hole, the sediment transport rate Q_s can be calculated by taking the time derivative of the sediment volume transported out of the scour hole as:

$$Q_s = \frac{d(\text{Cone volume})}{dt} = \frac{S\pi}{\tan\phi}\left(\frac{S}{\tan\phi} + D\right)\frac{dS}{dt} \tag{4.2}$$

where S is the scour depth, ϕ is the angle of repose. D represents the length scale of the structure, which is 0.305 m for the ELJ and solid cases in this work. Hence the rate of scour can be written as:

$$\frac{dS}{dt} = \frac{Q_s}{\frac{S\pi}{\tan\phi}\left(\frac{S}{\tan\phi} + D\right)} = f(S) \tag{4.3}$$

The right hand side of the equation can be written as a function $f(S)$ because the sediment transport rate Q_s also depends on the scour depth S. The physical reason behind this is that as the scour depth S increases, the sediment transport rate Q_s gradually decreases. There is a functional relationship between the two. Thus, Eq. 4.3 is a nonlinear ordinary differential equation (ODE) for the scour depth S.

To solve the ODE in Eq. 4.3, we need to express Q_s as a function of scour depth. From the simulations, we have sediment transport rate inside the scour hole at each

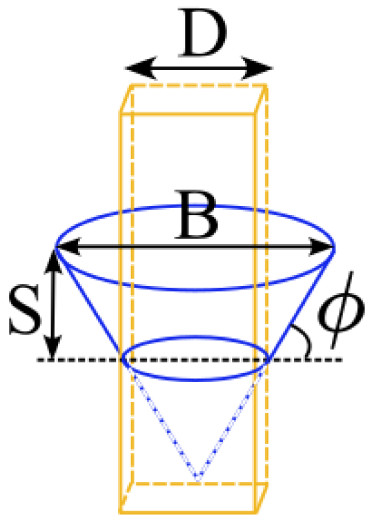

Figure 4.9. Conceptual cone-shaped scour hole.

written time step. At the same time, we adopt the familiar form for sediment transport rate in the literature, i.e., the sediment transport rate as a function of the Shields number has the form of:

$$\frac{Q_s}{\sqrt{RgD}DB} = a_1 \left[\tau^* - \tau_c^*\right]^{a_2} \tag{4.4}$$

where a_1 and a_2 are empirical coefficients. B is the scour hole width which can be approximated as a function of scour depth as:

$$B = \frac{2S + D}{\tan(\phi)} \tag{4.5}$$

We have derived the Shields number as a function of scour depth and porosity in Eq. 4.1, which can be plugged into Eq. 4.4 to yield

$$\frac{Q_s}{\sqrt{RgD}DB} = a_1 \left[\frac{b_1 \cdot (1-\phi_s)^{b_2}}{\frac{S}{S_e} + b_3} - \tau_c^*\right]^{a_2} \tag{4.6}$$

The simulation data for the nondimensionalized scour rate, expressed as $Q_s/(\sqrt{RgD}DB)$, and the dimensionless scour depth are fitted using Eq. 4.6. The result is shown in Figure 4.10. Points for the asymptotic behavior of the sediment transport, equal to zero at equilibrium condition, are also added. Based on Figure 4.10, the black fitted line captures the overall trend and slope of the data points, indicating a good fit for the relationship between sediment transport rate and scour depth. The fitted values of α_1 and α_2 are 0.34 and 2.70, respectively. These values are the same for both the solid and

porous cases, suggesting that they may be applicable across different structure types. This is also an evidence that our formulation in Equation 4.1 to incorporate porosity ϕ_s makes physical sense. If not, α_1 and α_2 will also depend on the porosity, which means they will have different values for the porous and solid cases.

The value of 2.7 for α_2 is also comparable with the result in previous works. The exponent α_2 fitted in Equation 4.4 for the term $(\tau^* - \tau_c^*)^{\alpha_2}$ is equivalent to the exponent used in the sediment number criterion $(N_s^2 - N_{sc}^2)^{5/2}$ in Carstens [1966] and LeFeuvre et al. [1970]. Their exponent value of 5/2 is close to the value of 2.7 found in this work.

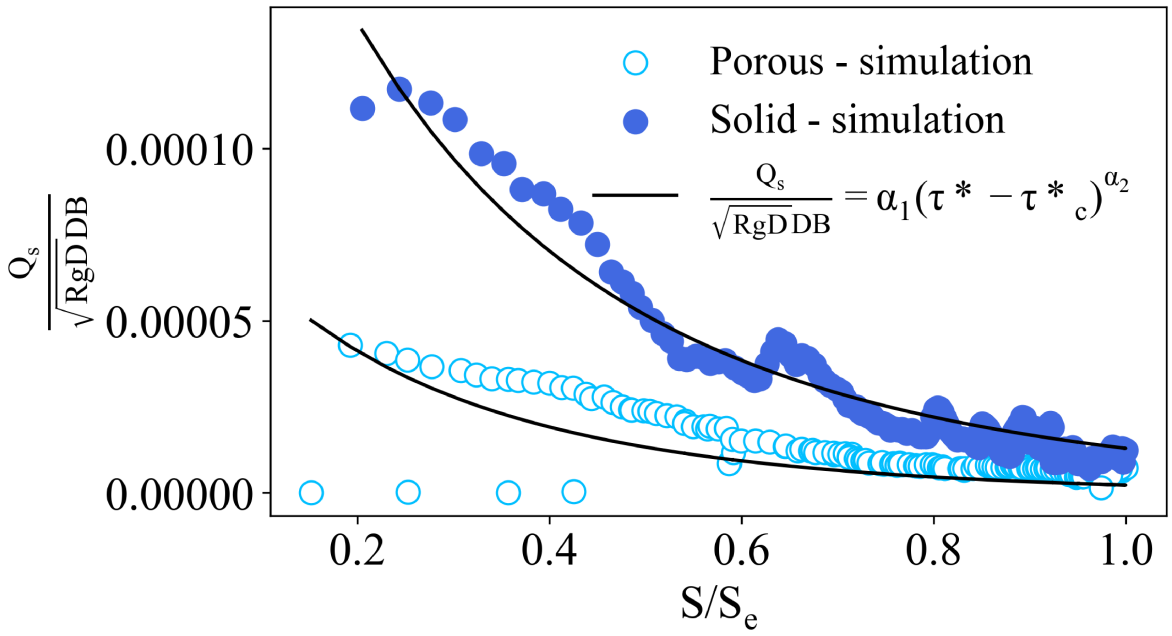

Figure 4.10. Sediment transport rate vs. scour depth.

By substituting Eq. 4.6 into Eq. 4.3 and after some mathematical manipulations, we have:

$$\frac{dS}{dt} = \frac{a_1 \left[\tau^* - \tau_c^*\right]^{a_2} \cdot \sqrt{RgD} DB \tan\phi}{\pi S(\frac{S}{\tan\phi} + D)} \tag{4.7}$$

Further, by substituting the shear decay function defined in Eq. 4.1 into Eq. 4.7, we have:

$$\frac{dS}{dt} = \frac{a_1 \left[\frac{b_1(1-\phi_s)^{b_2}}{\frac{S}{S_e}+b_3} - \tau_c^*\right]^{a_2} \sqrt{RgD} DB}{\pi S(\frac{S}{\tan\phi} + D)} \tag{4.8}$$

Finally, by substituting the width of the scour as a function of scour depth into Eq. 4.8,

we obtain the final form of the nonlinear ODE for S as:

$$\frac{dS}{dt} = \frac{a_1 \left[\frac{b_1(1-\phi_s)^{b_2}}{\frac{S}{S_e}+b_3} - \tau_c^* \right]^{a_2} \sqrt{RgD} D(2S+D)}{\pi S(\frac{S}{\tan\phi} + D)\tan\phi} \tag{4.9}$$

The initial condition for this ODE is $S(t=0) = 0$. The ODE was solved numerically using a Python script implementing the RK45 solver [Virtanen et al., 2020]. The predicted scour depth as a function of time from the simple conceptual model is compared against simulation data in Figure 4.11.

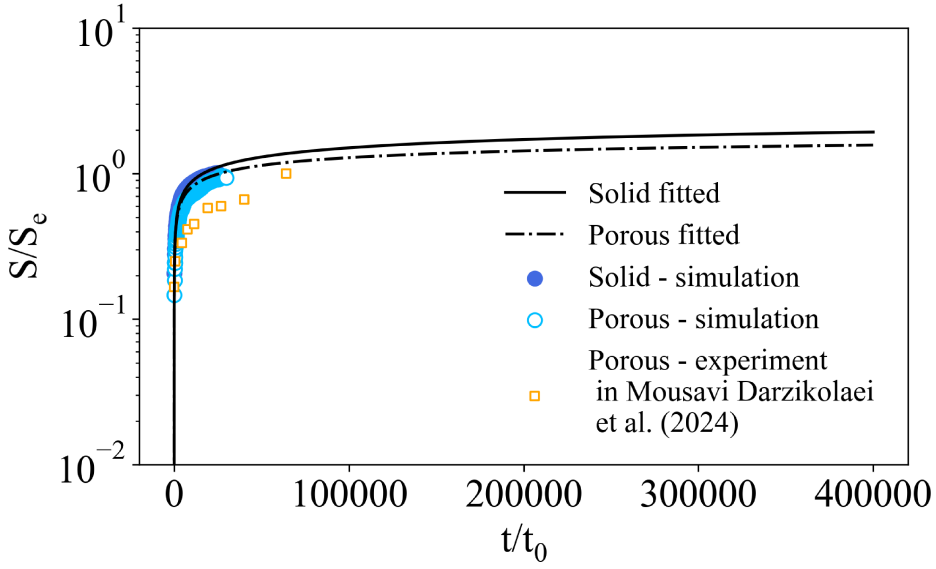

Figure 4.11. Predicted scour depth vs time.

The comparison in Figure 4.11 shows that the mathematical model (depicted by the line) accurately predicts the temporal evolution of scour depth. The model's predictions closely follow the trends of the observed data points in simulations for both the solid and porous cases, indicating a good fit. It is especially encouraging that the simple conceptual model collapses the data for both cases, meaning the single model correctly incorporates the porosity effect. The collapse of the data is due to the fact that the simple model utilizes an accurate shear decay function.

Conclusions

This study provides a comprehensive analysis of sediment transport and scour around solid and porous hydraulic structures using the *ibScourFoam* computational model. The

results demonstrate that structural porosity significantly influences the scour process, leading to reduced wall shear stress and more stable scour profiles. The developed semi-theoretical model for predicting the temporal evolution of scour depth offers a practical tool for engineers, allowing for better design and assessment of hydraulic structures in various environmental conditions. The findings emphasize the importance of considering structural porosity in the design of in-stream structures to mitigate the impact of scour and enhance the longevity and stability of these structures. Future work should focus on refining the shear decay function and further validating the proposed model under different flow and sediment conditions to expand its applicability.

Chapter 5
Scour Around Large Wood with Rootwads: An Experimental and Computational Study

5.1 Introduction

Installing nature-based in-stream structures is a common practice for river restoration. In-stream wood structures, such as large woody debris (LWD), are one example of this practice. LWD includes fallen trees, logs, stumps, root wads, and piles of branches, all of which offer physical and environmental benefits for river restoration projects [Shields Jr and Nunnally, 1984, Abbe et al., 2003, USBR and ERDC, 2016]. These structures create low-velocity regions and deep pools, providing essential shelter, foraging opportunities, and improved temperature conditions for aquatic species. However, the guidelines for designing and installing these structures are often case-specific, and gaps remain in our understanding of the fluid dynamics and bathymetric features around large wood structures with realistic geometry. Gaining this knowledge is crucial for enhancing habitat diversity [Collins and Montgomery, 2002].

Previous researches mostly focused on the flow and scour around "gray" infrastructures such as bridge piers and pipelines [Akoz, 2012, Sumer et al., 2002, Liang et al., 2005], . Very limited studies exist on the understanding of the more complex dynamics around large wood structures in river environments. Unlike bridge piers and pipelines, large wood structures introduce additional variables, such as varying length and flow blockage, burial and submergence ratios, and shape complexities. Studies on horizontally bedded cylinders, such as those in mining and pipeline applications, offer valuable insights that

can be relevant to understanding flow and sedimentation around cylindrical logs in rivers to some extent [Wilkens and Richardson, 2007, Hatton et al., 2007, Menzel et al., 2013, Morrison and Leder, 2018, Song et al., 2022a]. For example, as scour progresses along a pipeline, the surrounding sand may fail, causing the pipeline to sink into the bed [Sumer et al., 2001]. Similarly, Schalko and Nepf [2024] found that when logs are vertically mobile, some may become buried, diminishing their impact on bathymetric heterogeneity. Their study also highlighted how the overall morphological patterns were significantly influenced by the ratio of flow blocked by the log's exposed diameter, a factor that is crucial when considering the design and placement of large wood structures in river restoration efforts.

Previous researches also have primarily focused on simplified cylindrical logs, leaving the influence of more complex shapes, such as those with rootwads, largely unexplored. Song et al. [2022a] studied the effect of shape complexity on flow and scour around submerged cylindrical objects. They found that the tapered head and slender body of an object, compared to a cylinder, result in weaker contraction flow, leading to a smaller scour hole. When simple cylindrical logs are positioned on the bed, their single diameter determines whether they are submerged or emergent, which in turn affects whether downflow, sweeping flow above or flow acceleration on the two ends dominates the scouring process. Complexity also arises when part of the log, such as the rootwad, is submerged while another part is emergent, or when the degree of submergence varies along its length. This variation complicates the resulting flow and sediment transport dynamics.

LWD consists of individual pieces and jams, often formed around rootwads [Martin et al., 2016]. However, studies have often simplified trees into cylindrical logs to study hydraulics [Wilcox et al., 2006, Schalko et al., 2021a] or resistance effects [Reichl et al., 2005, Allen and Smith, 2012, Lai and Tullos, 2014], overlooking the key component of rootwads, which are usually porous and complex in nature.

In river engineering practices, logs are often used as stream deflectors. Pagliara et al. [2015a] and Pagliara et al. [2015b] studied the effects of log deflectors and branch deflectors on flow and sediment transport, showing that blocking part of the channel accelerates flow through the constricted region, creating circulation zones and scour pools downstream. To some limited extent, several studies have investigated the rootwad effect [Zhang et al., 2020c,a, Ravazzolo et al., 2022]. For example, Zhang et al. [2020a] examined bank erosion potential due to in-stream logs, showing that logs with rootwads can increase contracted velocity and potential bank erosion, although their study did

not consider erodible beds. Other researchers have also highlighted the importance of rootwads on bank erosion. For instance, Zhang et al. [2020c] showed that the rootwad of a fallen tree significantly alters flow and sediment dynamics, providing insights that in riparian environments, fallen trees can cause scour and bank erosion. Previous work showed that factors such as near-bank velocity, backwater rise, and wake interference are influenced by the blockage ratio and the distance between the log and the bank.

Previous research on the importance of rootwad consideration when modeling fallen logs has addressed some aspects of rootwad complexity, particularly focusing on flow. However, erodible beds evolve due to flow alterations around in-stream structures, with logs causing flow acceleration and sediment entrainment, resulting in scour pools and low-velocity zones where sediment deposits form bars and islands [Cherry and Beschta, 1989, Abbe and Montgomery, 1996, Dixon, 2016, Daniels and Rhoads, 2003]. These morphology change can then alter the flow dynamics as well, as seen in Schalko and Nepf [2024] for cylindrical logs.

Erodible-bed experiments in flumes such as those in Schalko and Nepf [2024] for single logs and Ismail et al. [2021] for porous engineered log jams are very valuable, but time consuming. Many previous researches have resorted to computational models as a powerful tool, which can provide detailed information about flow at very fine scales. For example, studies have used large eddy simulation (LES) to analyze realistic in-stream structures, such as rock weirs [Kang et al., 2016, Zeng et al., 2021], and to investigate coherent flow structures. However, conducting LES for real river restoration structures requires extensive computing resources. As an affordable alternative, simple one-dimensional (1D) models and increasingly depth-averaged two-dimensional (2D) models are used in practice. However, these models simplify the flow and scour processes, which are inherently three-dimensional (3D). To fully capture the important dynamics, this work adopted a 3D computational model which can simulate both flow and sediment transport.

The objective of this study is to bridge the gap in understanding the complex interactions between flow and sediment transport around complex in-stream river restoration structures, with an emphasis on the effects of porosity and shape complexity. By employing advanced computational techniques and flume experiments, we aim to investigate these processes around large wood structures featuring a porous rootwad and compare the findings with those around simple cylindrical logs, as illustrated in Figure 5.1.

When a structure, such as a log, is placed in the flow, several characteristic flow features emerge (see Figure 5.1). The flow contracts and deflects around the sides of

the log, leading to the formation of horseshoe vortices at the front, as well as lee-wake vortices behind the log. Sweeping flow occurs over the top of the log, and depending on the degree of erosion, jet-like flow may emerge from underneath the log. The flow dynamics is significantly altered when a porous rootwad is added to the end of the log. The rootwad introduces extra blockage into the flow. This will likely lead to further flow contraction between the rootwad and the channel banks. Rootwad is often porous and bleed flow can happen, which will modify the horse-show vortices and wake region. The inclusion of the porous rootwad is expected to have a pronounced effect on the erosion patterns.

This work seeks to shed light on the physical sediment transport mechanisms around large wood structures by addressing two fundamental questions:

- What impact does a porous rootwad have on flow and sediment transport compared to a single cylindrical log?
- To what extent must the geometry of these structures be resolved in numerical models to accurately capture flow and bathymetric features, and how are the results affected if the porous rootwad is omitted or simplified?

To address the first question, we conducted two flume experiments: one using a single log and another using a log with a rootwad. Flow velocity fields and equilibrium morphology between the two experiments were measured and compared.

To address the second question, we performed four simulations coupling flow and sediment transport using the 3D *ibScourFoam* model [Song et al., 2022c]: one for a simplified single log (SL), one with the fully resolved porous rootwad (PRW), one with the rootwad represented as a solid shape (SRW), and one where the rootwad is modeled using a simple porosity model (PM).

The structure of this paper is as follows: First, the flume experiments are described and the numerical model is introduced. The result section includes the measurement data and analysis, simulation results, and findings. Finally, this paper is concluded with some discussions.

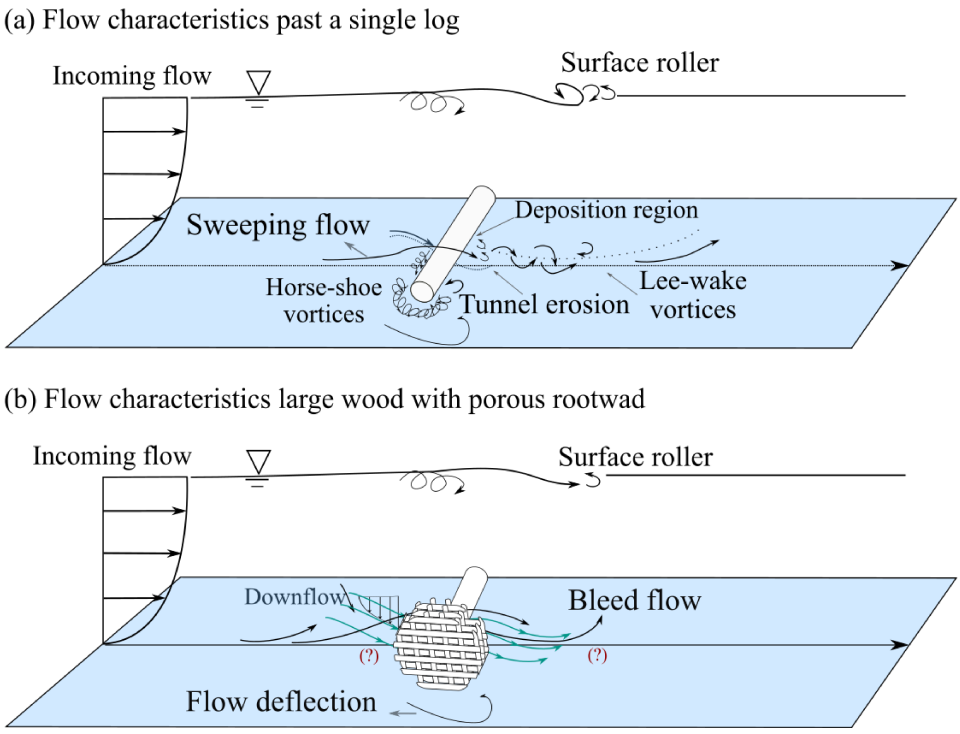

Figure 5.1. Flow characteristics past a solid log and a log with porous rootwad.

5.2 Methodology

5.2.1 Flume Experiments

The flume experiments were conducted in a recirculating flume, testing two large wood models. Details of the flume setup used in this research are shown in Figure 5.2. The goal of the experiments was to identify the distinct flow and morphological patterns between an individual log without a rootwad and one with an idealized porous rootwad. River restoration practices typically position these logs along channel walls. Therefore, one single log and one log with a porous rootwad were placed on the side of the flume, perpendicular to the incoming flow. The large wood models considered in this research partially span the channel and touch only one bank, mimicking a type of wood structure commonly used in natural flood management [Lo et al., 2021].

The size of these logs was chosen based on the minimum dimensions recommended by USBR and ERDC [2016] for large wood consisting of a rootwad and trunk. They suggest that the rootwad diameter should be at least equal to the bankfull discharge depth, the trunk diameter should be at least half of the bankfull discharge depth, and the trunk length should be at least 25 percent of the bankfull width. In our controlled

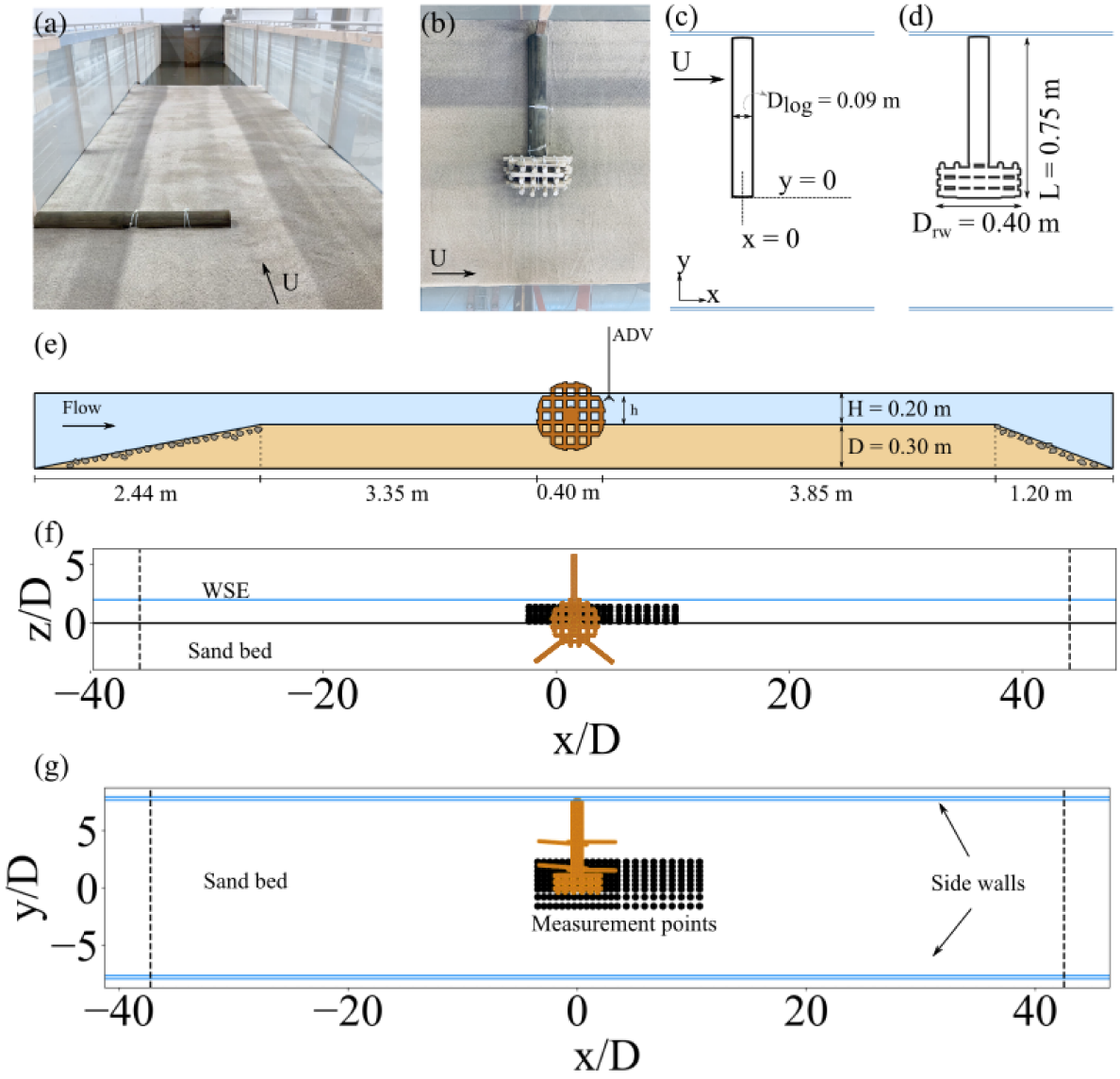

Figure 5.2. Flume experiments: (a) Single log exprimental model (b) Single log with porous rootwad exprimental model, (c) Schematic plan view of single log details, (d) Schematic plan view of single log with porous rootwad details, (e) Schematic side view of the experimental flume.

flume experiment where there is no floodplain, the bankfull width is considered as the width of the flume itself.

The trunks of the logs were made of a wooden circular log with a diameter of $D = 0.095$ m and a length of $L = 0.75$ m for the individual log and $L = 0.6$ m for the log with the rootwad. The total length of the logs was the same in both cases. The porous rootwad had a length of $L_{rw} = 0.15$ m and was constructed from a stack of wooden dowels to mimic the porosity in the rootwad. The dowels used in the porous rootwad have a

diameter of $D_D = 0.0254$ m. The stack of dowels is secured in place using plastic ties. The edges of the stacked dowels are cut to a disk shape with a diameter of $D_{rw} = 0.4$ m. The total volume of the rootwad, constructed in a disk shape, is 0.0201 m^3, while the total solid volume, represented by the solid dowels, is 0.0056 m^3. This results in a solid volume fraction of 0.28 and a volumetric porosity of $\phi_v = 0.72$ for the rootwad. Another important metric for characterizing the porous nature of the rootwad is the surface porosity, which is defined as the percentage area on the upstream surface which is open to flow. For the surface porosity calculations, the frontal area of the solid part is 0.0392 m^2, and the frontal area of the cross-section is 0.0644 m^2, giving a surface porosity of $\phi_s = 0.39$.

The circulating hydraulic flume is equipped with a pump that has a maximum flow rate of 240 l/s. The flume measures 15.24 m in length, 1.52 m in width, and 0.91 m in depth (Figure 5.2-c), with a slope set to $S_0 = 0.00075$. To minimize turbulence in the incoming flow within the test reach, a reservoir is positioned downstream, and a flow straightener is placed upstream. The flume's glass side walls allow for clear observation throughout the experiment. Additionally, the flume is outfitted with instruments capable of taking horizontal, lateral, and vertical measurements.

The bed of the flume is composed of poorly graded medium sand, with a median sediment size of $D_{50} = 0.67$ mm and a gradation coefficient $\sigma_g = 1.27$. Although riverbed sediment is typically heterogeneous, we used uniform sand to isolate and understand key physical processes without introducing additional variables. The depth of the sand bed is 0.305 m. To ensure a gradual transition from the rigid bed to the erodible bed and to facilitate fully developed flow, two sloped transition zones covered with cobblestones were constructed upstream and downstream of the erodible bed.

Before each test, the structures were placed in the bed, the sand bed was leveled, and the flume was slowly filled with water to a depth of $H = 0.2$ m above the sand bed, ensuring no disturbance to the bed before the tests began. The schematic view of the flume initial condition is shown in Figure 5.2-e.

Initially, the trunks and rootwad were half-buried in the flat, erodible sand bed. In both cases, the trunks were fully submerged, while part of the rootwad remained emergent. The rootwad was positioned away from the wall, with the side of the trunk attached to the side wall using a wooden stud. To secure the structure's position, a cradle made of two wooden crosses was used to anchor the log trunks on the bed surface. In field applications, logs are often similarly anchored with boulders for stability.

The coordinates of the logs and the flume experiments are shown in Figure 5.2-f.

The centerline of the flume is designated as the y-axis origin, while the center of the structure's lateral cross-section is considered the x-axis origin.

The chosen inlet discharge ensures that scour occurs locally around the structures, keeping sediment transport within the clear-water scour regime. The inlet flow is selected to produce an applied Shields number slightly below the critical Shields number, thereby preventing sediment movement due to shear stress in areas away from the structure. During each experiment, the pump discharge was gradually increased and adjusted to achieve the desired flow.

To accurately determine the mean velocity and water depth, a combination of the Chezy equation and trial-and-error is used, ensuring that the Shields number remains below the critical threshold. The applied Shields number θ, as defined in Shields [1936], is given by:

$$\theta = \frac{u_*^2}{RgD_g} \tag{5.1}$$

where u_* is the shear velocity, $R = 1.65$ is the submerged specific gravity and D_g is characteristic grain size. The critical Shields number for the sand used in the experiments is estimated at $\theta_c = 0.016$ [Brownlie, 1981, Parker et al., 2003].

To ensure clear-water scour conditions and accommodate the minimum size of large wood structures based on river restoration practices, the target inlet mean velocity and water depth were set at $U = 0.25$ m/s and $H = 0.2$ m, respectively. The hydraulic conditions for the experiments are summarized in Table 5.1. The Reynolds number and Froude number are calculated as $Re_H = U_0 H/\nu = 5 \times 10^4$ and $Fr_H = U_0/\sqrt{gH} = 0.18$, where U_0 is the averaged incoming velocity, H is the flow depth above the sand bed, ν is the kinematic viscosity, and g is the gravitational acceleration. The Reynolds number based on the length scale of rootwad diameter is $Re_{RW} = 10^5$.

The vertical profiles of inlet velocity were measured using an Acoustic Doppler Velocimeter (ADV) at a point 1 meter upstream of the structures. A laterally averaged velocity for each depth was calculated, and the profile was fitted to the logarithmic law:

$$\frac{u}{u_*} = 2.5 \ln\left(\frac{30z}{k_s}\right) \tag{5.2}$$

From this fitting, the Nikuradse equivalent sand roughness (k_s) and the friction velocity (u_*) were determined. The resulting inlet velocity profile is shown in Figure 5.3. The obtained values are $k_s = 0.0004$ m and $u_* = 0.0112$ m/s. The Shields parameter calculated with these values is $\theta = 0.014$, below the critical value of 0.016, confirming the clear-water scour regime.

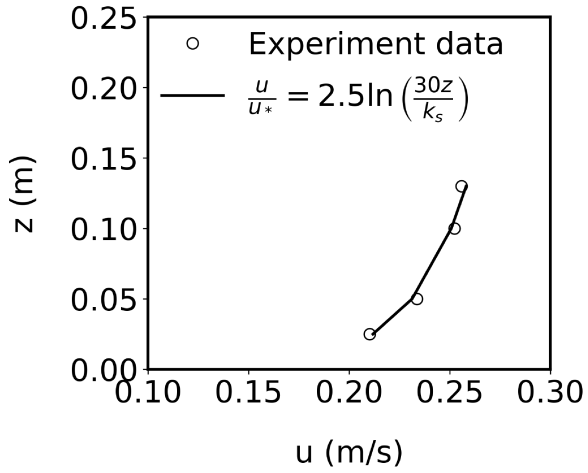

Figure 5.3. Logarithmic fit to upstream undisturbed inlet velocity profile

Table 5.1. Summary of test conditions of experiment cases

	Case 1	Case 2
Structure	Single log	Log with porous rootwad
Location	Side	Side
$\phi_{V,RW}$	-	0.72
$\phi_{S,RW}$	-	0.39
$U_{ave,in}$ (m/s)	0.25	0.25
H (m)	0.2	0.2
Q_{in} (m^3/s)	0.07	0.07
Fr_H	0.18	0.18
Re_H	50,000	50,000
Re_{RW}	100,000	100,000

Once the sand bed reached an equilibrium state, where any changes in bathymetric patterns were negligible, velocity measurements were taken using a Nortek Vectrino Plus Acoustic Doppler Velocimeter (ADV). Data quality is ensured by adjusting the ADV measurement properties based on the recommendations from García et al. [2005], including optimizing signal-to-noise ratios.

To capture the 3D velocity near the rootwad and identify flow features, measurements were taken in three vertical slices at lateral coordinates of $y/D = -0.8$, $y/D = 0.66$, and $y/D = 1.86$, where y is the distance from the origin, which runs through the centerline of the flume, and D is the diameter of the log. Velocity was measured at five depths: $z/D = 0.157$, $z/D = 0.315$, $z/D = 0.63$, $z/D = 1.05$, and $z/D = 1.36$, covering the longitudinal range of $x/D = -3.6$ to $x/D = 8.9$ for the vertical slices. Additionally, one horizontal slice at mid-depth of the flow was measured to complement the vertical

measurements, covering the longitudinal range of $x/D = -3.6$ to $x/D = 10.5$ and the lateral range of $y/D = -1.6$ to $y/D = 2.3$. The coordinates of the measurement points are shown in Figure 5.2(f and g).

5.2.2 Computational Modeling Setups

Four numerical experiments were conducted using the *ibScourFoam* model, with flow and sediment transport coupled in all simulations. For turbulent flow modeling, the RANS approach was adopted and the $k-\omega$ SST-SAS model was utilized. The erosion process was modeled using an immersed boundary method, based on the algorithm developed in Xu and Liu [2017] and Song et al. [2022b]. The model was developed with the open source computational modeling platform OpenFOAM [OpenFOAM Foundation, 2018]. In the numerical experiments, a background mesh was used to solve the flow, while the erodible bed was represented as an immersed boundary. Further details on the immersed boundary method and the *ibScourFoam* solver can be found in Song et al. [2022a,b].

The numerical simulations included the following: one single log (SL), one log with a fully resolved porous rootwad (PRW), one log with a solid rootwad (SRW), and a log with a porosity modelled rootwad (PM). In the SRW case, the rootwad existed. However, the porous nature of the rootwad was ignored. In the PM case, instead of resolving all the geometric details of the rootwad, it was simplified as a porous media and its effect to the flow is through the additional drag term in the flow momentum equations.

The size and geometry of these logs in the computational modeling were designed to replicate those in the flume experiments. For the fully resolved cases (SL, PRW, and SRW), the geometries of the structures were used to generate the background mesh. For the porosity model case (PM), the rootwad region within the background mesh was marked. The additional flow resistance due the porous media was only applied to that region. The porous media flow resistance follows the Darcy-Forchheimer formula, which accounts for both viscous and inertial resistance, which has the form of:

$$\frac{\partial \overline{u}_i}{\partial t} + \frac{\partial (\overline{u}_i \overline{u}_j)}{\partial x_j} = -\frac{1}{\rho}\frac{\partial \overline{p}}{\partial x_i} + \frac{\partial}{\partial x_j}\left[(\nu + \nu_t)\frac{\partial \overline{u}_i}{\partial x_j}\right] + S_i \tag{5.3}$$

where $\overline{u}_i$ is the Reynolds-averaged velocity component in the i-th direction, and x_j is the spatial coordinate in the j-th direction. ρ is water density, and $\overline{p}$ is the Reynolds-averaged pressure. ν is the kinematic viscosity of the fluid and ν_t is the turbulent eddy viscosity.

S_i is the additional resistance to model porous region, which is defined as

$$S_i = -\left(\nu_t d + \frac{1}{2}|\overline{u_j}|f\right)\overline{u_i} \tag{5.4}$$

According to Van Gent [1996], the Darcy (D) and Forchheimer (F) coefficients can be calculated as follows:

$$d = \alpha\frac{(1-n)^2}{n^3}\frac{1}{D_{50}^2} \tag{5.5}$$

$$f = 2\beta\frac{1-n}{n^3}\frac{1}{D_{50}} \tag{5.6}$$

Here, n represents the porosity, and D_{50} is the characteristic length scale of the grain in porous media. In our model, D_{50} is defined as the characteristic length scale of the dowels, which is 0.0254 m. The coefficients α and β need to be calibrated for specific porous media. We tested different combinations of coefficient values as reported in Jensen et al. [2014] ($\alpha = 1000$, $\beta = 1.1$), Van Gent [1996] ($\alpha = 200$ and $\beta = 2$). These values were calibrated by comparing velocity field results with experimental data and the fully resolved rootwad case. For our simulations, we selected $\alpha = 1000$ and $\beta = 1.1$. The volumetric porosity was set to $n = \phi_v = 0.72$, resulting in $d = 321,910.5$ and $f = 64.5$. These values are also consistent with those chosen in the work of Xu and Liu [2017], which provided the best results among different combinations of α, β, and D_{50}.

For all cases, the background mesh was utilized to solve the hydrodynamic equations over a period of 50 seconds (about 10 flow through times), ensuring that the flow reached a fully developed state. Subsequently, the sediment computation was initiated and continued in parallel with the hydrodynamics until the bed reached equilibrium. The detailed setup and parameters of each simulation domain are presented in Table 5.2 and Figure 5.4. In the computational model, the upstream distance from the logs in the domain was set to $7D$, while the downstream distance was set to $20D$. The width of the simulated channel was approximately $16D$, matching the width of the experimental flume as shown in Figure 5.4. The flow depth was set to $H = 2.1D$, and the bottom sand bed extended to z = -$3D$, as defined in the background mesh. The total cell count of the background mesh was approximately 6.11 million, 6.07 million, 5.77 million, and 5.96 million for the simulation cases SL, PRW, PM, and SRW, respectively. In all cases, the mesh resolution was consistent, with refinement near the objects and the observed scour region in the experiments.

To accelerate the simulation and utilize the fact that the morphological change is a

much slower process than hydrodynamics, a common practice in scour modeling is to use a morphological factor. In this work, a morphological factor with a value in the range of 200 and 1000 was used. The morphological factor was manually adjusted during the simulation to ensure numerical stability. For all the four simulations, the simulation time was in the range of 230 s to 350 s, which corresponds to real time of about 37 hours to 45 hours.

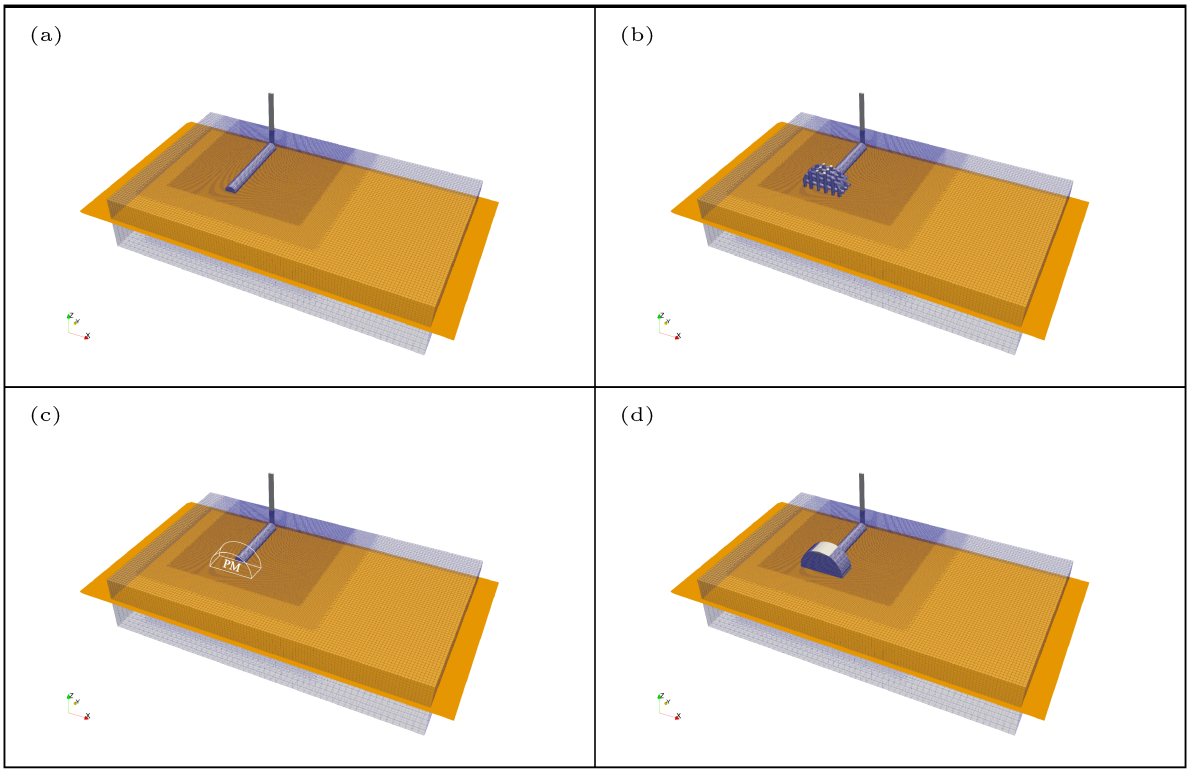

Figure 5.4. Computational setup: (a) single log without rootwad (SL), (b) porous rootwad (PRW), (c) porosity model for rootwad (PM), (d) solid rootwad (SRW).

The boundary conditions for the channel bottom, sidewalls, and log model structures were defined as wall boundaries. To properly model the near-wall flow dynamics, the wall function as described by Song et al. [2022a] was used. The free surface was set as a free-slip rigid lid. The maximum y^+ near the wall and the structure was 100, while the maximum immersed y^+ near the structure was approximately 17.

Table 5.2. Summary of conditions for simulation cases

Parameter	SL	PRW	PM	SRW
$U_{ave,in}(m/s)$	0.25	0.25	0.25	0.25
$H(m)$	0.2	0.2	0.2	0.2
α, β	-	-	1000, 1.1	-
RW Diameter (D_{rw})	-	0.4	0.4	0.4
Trunk Diameter (D)	0.095	0.095	0.095	0.095
ϕ_s (m)	-	0.391	-	0
ϕ_v (m)	-	0.721	-	0
Cell counts (million)	6.11	6.07	5.77	5.96
k_s (m)	0.0004	0.0004	0.0004	0.0004
D_{50} (mm)	0.67	0.67	0.67	0.67
θ_c	0.016	0.016	0.016	0.016
Core counts	40	40	40	40
Time steps	0.005	0.005	0.005	0.005
Simulated time (s)	290	350	265	230
Real time (hr)	39	39	45	37

5.3 Results

5.3.1 Experimental Results and Observations

5.3.1.1 Flow Velocity Field at Equilibrium

To investigate the variability of flow resulting from rootwad placement compared to a simple cylindrical log, we visualized velocity contours based on ADV point measurements. These measurements were taken at three vertical slices and one horizontal slice, as shown in Figure 5.5. The x and z coordinates of the rootwad are indicated in the right column for the vertical slices. On the vertical and horizontal slices, Figures 5.5 (d), (f), and (h) are partially blocked by the rootwad. However, on the slice at $y/D = 1.87$ (Figures 5.5 (b)), where the flow is not obstructed by the rootwad, its influence on the velocity field is still evident.

Velocity reduction behind large wood structures can promote fine material accumulation and provide shelter for aquatic species. As shown in Figures 5.5(a) and (b), velocity reduction extends further downstream of the trunk region for the single log (SL) compared to the porous rootwad (PRW), though the PRW shows greater vertical reduction.

Sweeping flow over the log is evident on the vertical slices at $y/D = 1.87$ and $y/D = 0.67$ for the SL case (Figures 5.5a and c), as well as in the horizontal slice

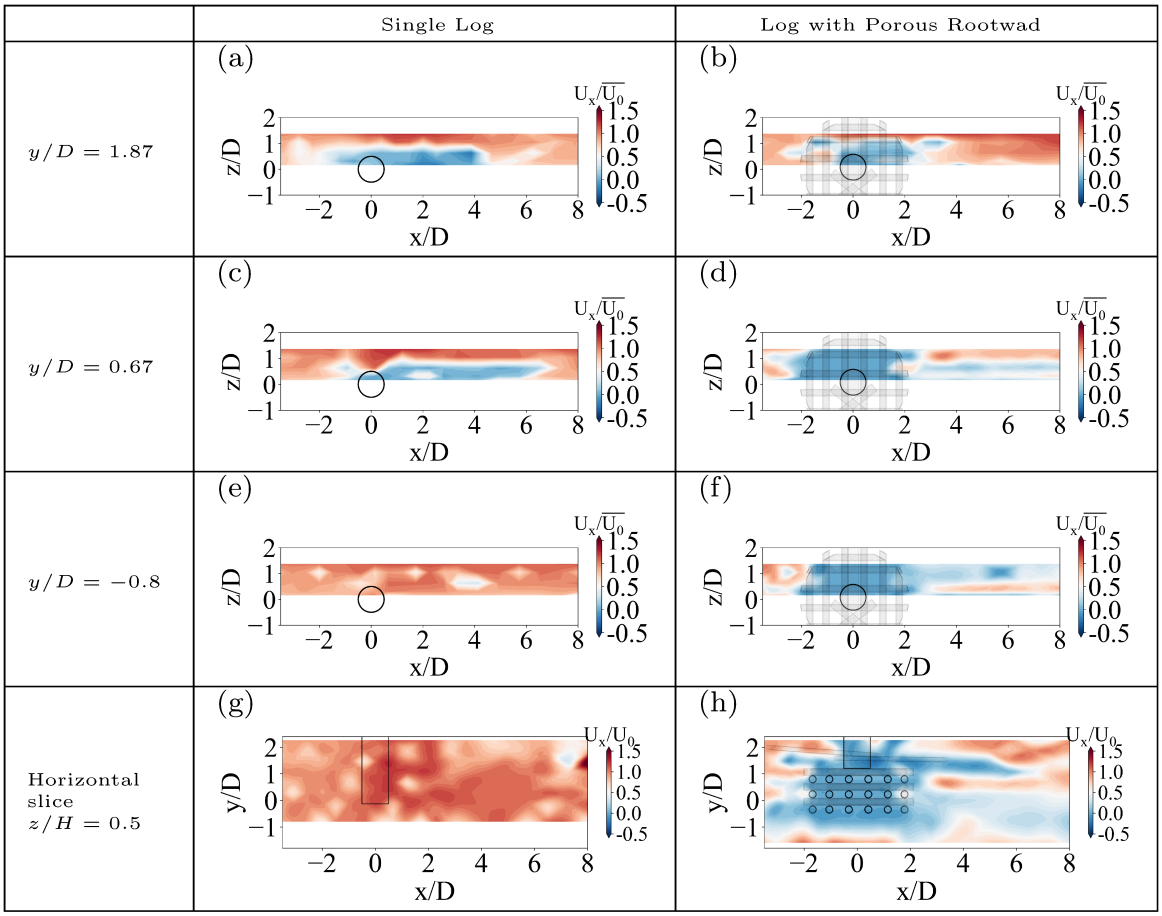

Figure 5.5. Experimental results of vertical and horizontal velocity contours for the single log and the log with a porous rootwad.

(Figure 5.5g). For the PRW case, this sweeping flow is only visible on the $y/D = 1.87$ slice.

PRW exhibits a longer reduced velocity downstream at $y/D = -0.8$ and $y/D = 0.67$ and a wider shear layer compared to the SL case. On the $y/D = -0.8$ slice, while the SL case shows a velocity close to or slightly higher than the incoming flow, indicating minor contraction, the PRW case shows reduced velocity, with contraction occurring further in the free shear region, pushing the shear layer downstream. This extension is also evident on the horizontal slice.

The highly porous rootwad region has a significant impact, which is lost when the rootwad is excluded. The bleeding flow through the rootwad reduces the length of the low-velocity region in the vicinity of the wall where the trunk of the rootwad is attached. On the other hand, it enhances the velocity reduction in the free shear layer. It reduces

the sweeping flow over the log and increases the contraction flow zone around the end. The downflow is more pronounced with the rootwad, and the overall reduced velocity wake region is more significant for the log with the rootwad. Additionally, the flow reattachment to the bed is disrupted by the bleeding flow through the porous rootwad.

5.3.1.2 Equilibrium Bathymetry

The equilibrium bathymetry offers valuable insights into the processes driving local sediment transport around the structures. To achieve this, experiments must be conducted long enough for erosion and sediment transport around the structures to stabilize. In this work, each experiment took more than 96 hours to reach equilibrium.

Photos of the equilibrium bed after draining the water from the flume for both experiments are shown in Figure 5.6. For the single log case, a primary scour hole is evident at the upstream end of the log, propagating laterally and exposing a significant portion of the log's length. This scour hole also extends upstream. Additionally, a secondary scour hole is visible downstream of the log, indicating recirculation of the sweeping flow from upstream. This is further evidenced by some deposition observed just downstream of the log. In the case of the log with porous rootwad, a horseshoe scour hole has exposed the upstream face and sides of the rootwad to the flow, while part of the rootwad remains buried downstream. There is also a scour hole beneath the trunk of the log with porous rootwad, indicating jet-like flow under the trunk. In the single log case, this flow was not strong enough to fully expose the trunk.

To better quantify the erosion process, the bathymetric surfaces were captured using a scanner that employs the Structure-from-Motion (SfM) technique. The scans are shown in Figure 5.7(a) and (b). The bed surface elevation contours from the scanned bed are plotted and are shown in Figure 5.7 (c) and (d). The comparison between the scoured beds in the two experiments shows significant differences.

For the single log case, the main horse-shoe scour hole is located at the edge of the log and upstream. This is due to horse-shoe vortices forming at the edge. Tunnel erosion also occurred, exposing the edge of the log and part of the supporting cradles. However, it did not result in significant jet-like flow erosion beneath the log due to the blocking effect of a deposition bar just downstream of the log. The log remains partially buried on the downstream side and is not fully exposed to the flow. Two shallower scour hole extends downstream from $x/D = 1.25$ to $x/D = 7.5$. This is due to the sweeping flow that recirculates and erodes the bed, also carrying sediment that is deposited downstream of the log. The two downstream scour holes are connected. The primary scour hole

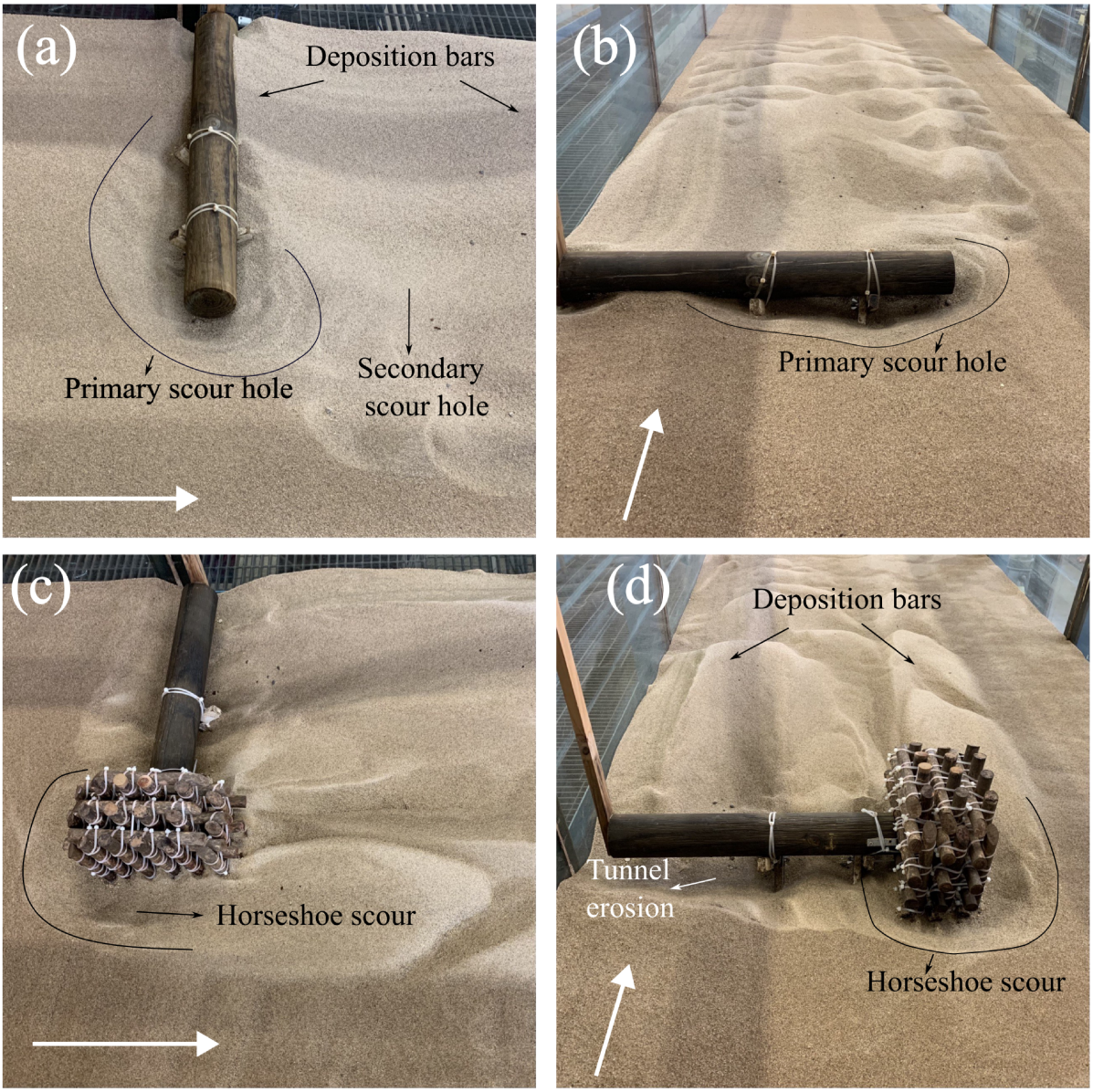

Figure 5.6. Equilibrium bed morphology for the two experiments: (a) side view of the single log, (b) front view of the single log, (c) side view of the log with porous rootwad, and (d) front view of the log with porous rootwad.

extends downstream for a distance equal to one log diameter, while the secondary scour hole reaches up to 9 log diameters downstream. The lateral deposition bar extends from the mid-length of the log towards the side wall. The eroded materials are then picked up by the lee-wake vortices and deposited downstream of the secondary scour hole.

For the log with porous rootwad case shown in Figure 5.7 (d), a horse-shoe shaped scour hole is observed due to the downflow upstream of the emergent rootwad and the

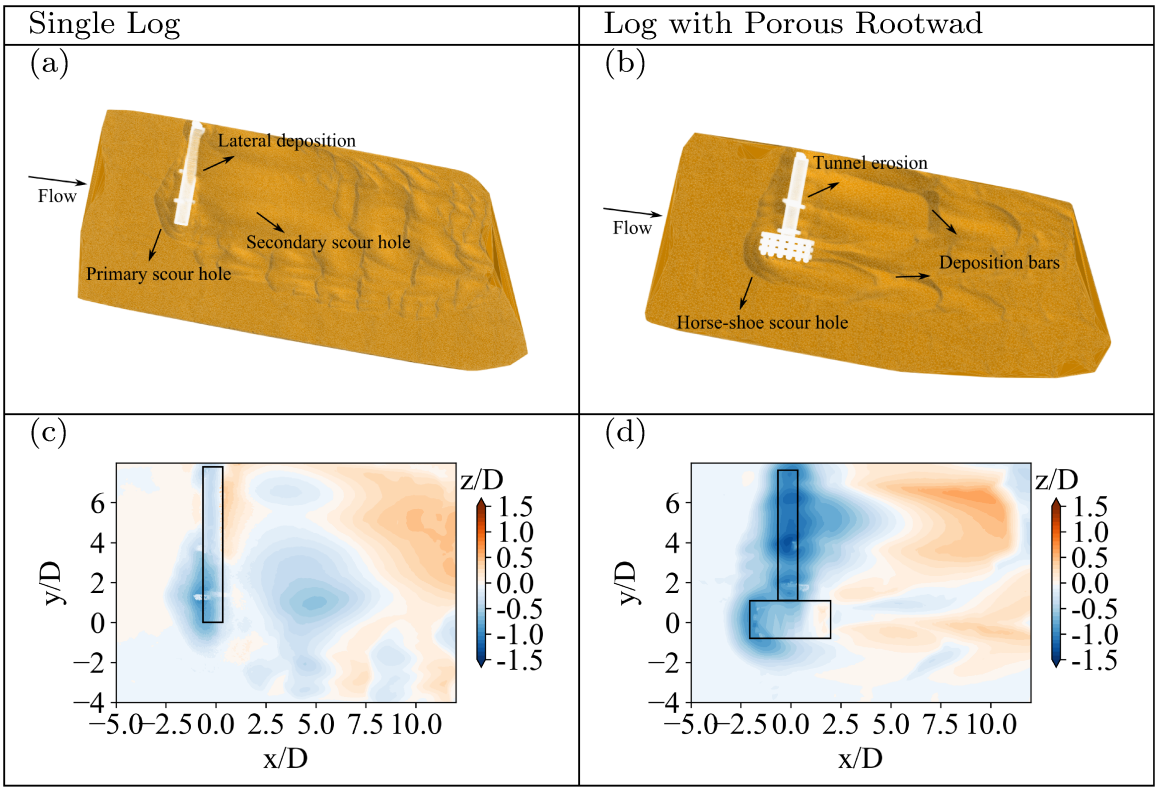

Figure 5.7. Experimental results of equilibrium bathymetry: (a) and (b) are bathymetry scans, (c) and (d) are bathymetry contours.

formation of horse-shoe vortices around the upstream edge of the porous rootwad. Both sides and the upstream face of the rootwad are exposed to the flow. Tunnel erosion also occurred, extending beneath the log, exposing the cradles, and continuing through until the wall. Unlike the single log case, where a scour hole resulting from sweeping flow recirculation might be expected downstream of the trunk, the presence of the porous rootwad appears to interrupt this process. Instead, a band of erosion is observed, which is diverted toward the wall, likely due to the shear layer generated by the rootwad. The deposition pattern also differs, with two deposition bars forming downstream of PRW, separated by the erosion band. Both deposition bars are attached to and initiated from the trailing edges of the rootwad. Similar to the single log case, the highest point of deposition is pushed toward the wall. The footprint of the horseshoe-shaped scour extends from x/D = -2.5 to 2.5 downstream, while the tunnel erosion stretches from x/D = 1 to 5. The erosion band downstream of the rootwad extends from the trailing edge of the rootwad to x/D = 12.5.

5.3.2 Numerical Results

5.3.2.1 Flow Validation

Computational simulations provide a more comprehensive view of the flow dynamics and sediment transport near the large woods. To validate the model, we first compared the fully resolved porous rootwad simulation results to experimental measurements. The velocity results for the porous rootwad (PRW) case at equilibrium, compared with the averaged velocity measured from flume experiments, are shown in Figure 5.8. The longitudinal velocity profiles at $y/D = 1.86$ at different water depths are presented in Figures 5.8(a) to (d). The spanwise velocity profiles at $z = 10$ cm, corresponding to half the depth or $z/D = 1.05$, and at three different streamwise x coordinates are shown in Figure 5.8(e).

The comparison of longitudinal velocity profiles shows that, simulation captures the downflow in the upstream region of large wood. Downstream, closer to the structure and at mid-depth, the simulation results align more closely with the experiments compared to the deposition region and areas closer to the water surface. For the lateral velocity profiles, the simulations successfully captured the velocity reduction in the wake region and the recovery to the incoming average velocity in the shear layers. The velocity in the shear layer is also close to the experimental values. Overall, the comparison is reasonable, with discrepancies likely due to the use of RANS equations and coarse meshes, which may not fully capture smaller-scale coherent flow structures.

5.3.2.2 Flow Simulation Results

One advantage of simulations over experiments is the ability to examine the velocity field even in areas close to the structure or inside the porous rootwad, where ADV measurements cannot access or capture the velocity field. Additionally, simulations allow us to analyze the velocity field across the entire domain with high resolution, which would be a daunting task to achieve through measurements alone. In fact, many experimental studies provide velocity profiles at discrete coordinates, while simulations offer more continuous and detailed results across the entire domain. Hence, simulated velocity contours are examined to better understand the physical processes governing flow around large wood structures and to compare different representations of rootwads.

The streamwise velocity contours on three vertical planes are shown in Figure 5.9. These planes correspond to three spanwise locations: one in the unobstructed free stream region, one passing through the center of the rootwad, and one passing through the

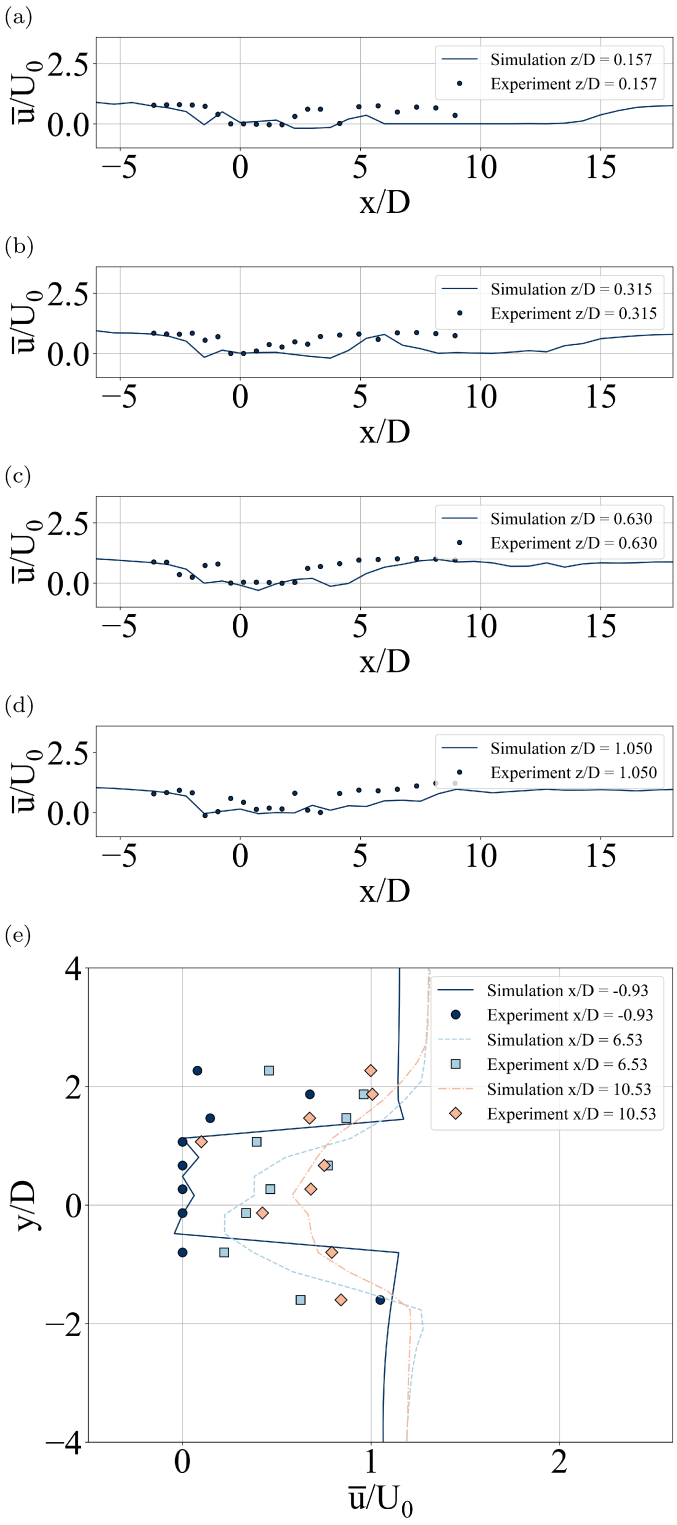

Figure 5.8. Computer model validation with streamwise velocity: (a) Longitudinal profile at $y/D = 1.86$ and $z/D = 0.157$, (b) Longitudinal profile at $y/D = 1.86$ and $z/D = 0.315$, (c) Longitudinal profile at $y/D = 1.86$ and z/D =0.63, (d) Longitudinal profile at $y/D = 1.86$ and z/D =1.05, and (e) Spanwise profiles at $z/D = 1.05$ and three different x locations.

center of the trunk where no rootwad is present.

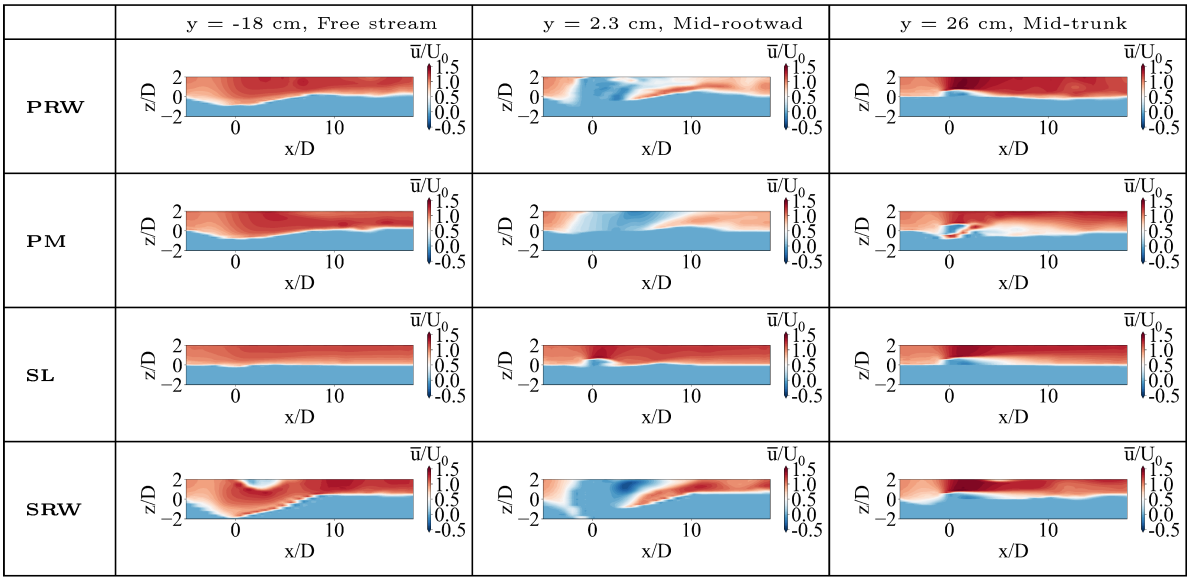

Figure 5.9. Streamwise velocity contours on vertical planes

On the plane in the free stream region (first column in Figure 5.9), velocity acceleration is observed in all cases. The least acceleration occurs in the single log (SL) case, while the most acceleration is seen in the solid rootwad (SRW) case. The results for the porosity model (PM) are also close to those of the fully resolved rootwad case. In the solid rootwad case, the effect of the rootwad blockage is evident in the velocity reduction in the wake region. This reduction is particularly noticeable near the downstream face of the rootwad and extends toward the water surface, as seen on the free stream slice.

The middle column in Figure 5.9 shows vertical planes that pass through the center of the rootwad. In the SL case, a small region of velocity reduction is observed in both the downflow and wake regions, along with velocity acceleration above the log. In other areas, the flow remains mostly uniform and close to the incoming velocity. In the other three cases where the rootwad is represented, the velocity field shows more disturbances. In Figure 5.9, for the fully resolved PRW case, velocity reduction occurs both in the downflow upstream of the rootwad and downstream in the wake. The downflow effect is more pronounced in the SRW case compared to the PRW case, while it is slightly less pronounced in the PM case. In the rootwad wake, velocity reduction occurs closer to the water surface, while near the bed, velocity acceleration is observed. The effect of bleeding flow through the rootwad increases flow variability in the wake region for the PRW case compared to the SRW and PM cases. This bleeding flow in the fully resolved PRW case also attenuates velocity reduction in the rootwad wake compared to

the SRW and PM cases. In the SRW case, the reduced velocity in the wake region is more significant and contains reversed flow near the water surface, indicated by dark blue contours. In contrast, the PRW case exhibits positive bleeding flow in this region, shown by red contours. The velocity acceleration near the bed is higher in the PRW case compared to the PM case but lower than in the SRW case. This same order applies to the longitudinal extent of the velocity acceleration downstream of rootwads. The final plane is located at the midpoint of the trunk, where there is no rootwad obstruction. In this region, the wake length for the PRW case is smaller than in all other cases. The velocity acceleration above the trunk is greater in the third column of Figure 5.9 compared to the first column, due to the constrained flow area between the wall and the rootwad. The downflow in the SL case is similar to that in the PRW case, both of which are influenced by the bed morphology, as these two cases share similar features.

For the SRW case, downflow is observed inside the scour hole upstream of the log. The PM case uniquely captures the tunnel velocity field beneath the log. This tunneling effect results in a downstream velocity deceleration, which extends more than $10D$ into the wake region.

Wake characteristics can be better understood by investigating the flow at horizontal planes. Hence, the streamwise time-averaged velocity contours on horizontal planes at different flow depths are shown in Figure 5.10. For the three cases with a rootwad (PRW, PM, and SRW), at a depth closer to the bed ($z = 5\,\text{cm}$), two regions of velocity reduction are evident: one due to the presence of the trunk and the other due to the rootwad. These regions are separated by a shear layer that originates at the junction of the rootwad and the trunk. Both of SRW and PM cases underestimated this shear layer. For the PM case it is likely due to the jet-like flow beneath the log. In the SRW case, the trunk wake is similar to PRW case with negative velocity. At this depth, the SL case shows one reduced-velocity region only downstream of the trunk, characterized by a wider wake than the other cases.

At mid-depth ($z = 10\,\text{cm}$), shown in the second column of Figure 5.10, velocity reduction is observed downstream of the trunk, close to the wall, and downstream of the rootwad in the PRW case. The wake of the trunk is narrower in the PRW case than in the PM case but wider than in the SRW case. The trunk wake is the widest for the SL case. The rootwad wake velocity is also more variable, with the higher velocity of the bleeding flow through the PRW rootwad being noticeable. This is likely due to wake vortices at the scale of the dowels or rootwad elements the PRW case, while the wake vortex is larger in the SRW case. In the PM case, the rootwad wake velocity values are reduced

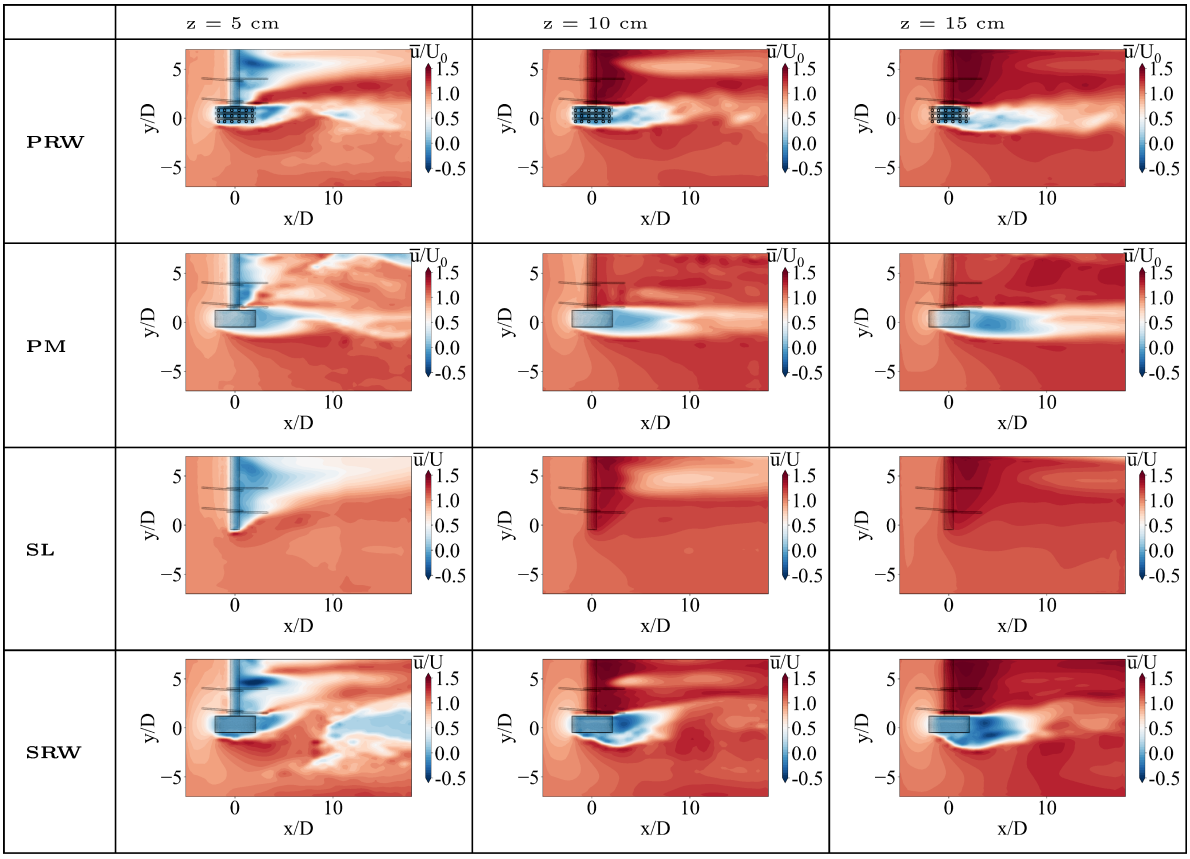

Figure 5.10. Streamwise velocity contours in horizontal planes

but remain uniform. For the SL case, no velocity disruption is observed in this region as there is no rootwad present. In the SRW case, negative velocity values indicate more flow diversion toward the free stream region, with flow recirculation observed toward the wall from the rootwad. The length of the wake in the PRW case is shorter than in the PM case but longer than in the SRW case, likely due to the deposition bar downstream of the rootwad that confines the wake region for both the PRW and SRW cases.

Comparing the third column with the previous ones, the primary distinction lies in the wake region generated by the log trunk blockage, which extends further downstream near the bed, exhibiting limited influence at greater depths. The rootwad wake's velocity deficit is more pronounced and persists longer near the water surface, particularly in the fully resolved case. At mid-depth and above, the velocity above the trunk is higher in both the SRW and PRW cases compared to the PM case, where some flow passes beneath the trunk (Figure 5.9). This was also observed in the experiment.

5.3.2.3 Longitudinal Profiles of Equilibrium Bathymetry

Figure 5.11 presents the longitudinal profiles of equilibrium bathymetry for different representations of the rootwad models and the corresponding experimental results. The elevations in the fully resolved porous rootwad model (PRW) and single log model (SL) closely match the experimental values along the slice passing through the rootwad edge (y = -2 cm). In contrast, the SRW model overestimates the scour depth at this location, while the porosity model (PM) underestimates it. A different pattern is observed along the slice passing through the trunk (y = 26 cm), where the PM model performs better, since it captured the tunneling effect beneath the log.

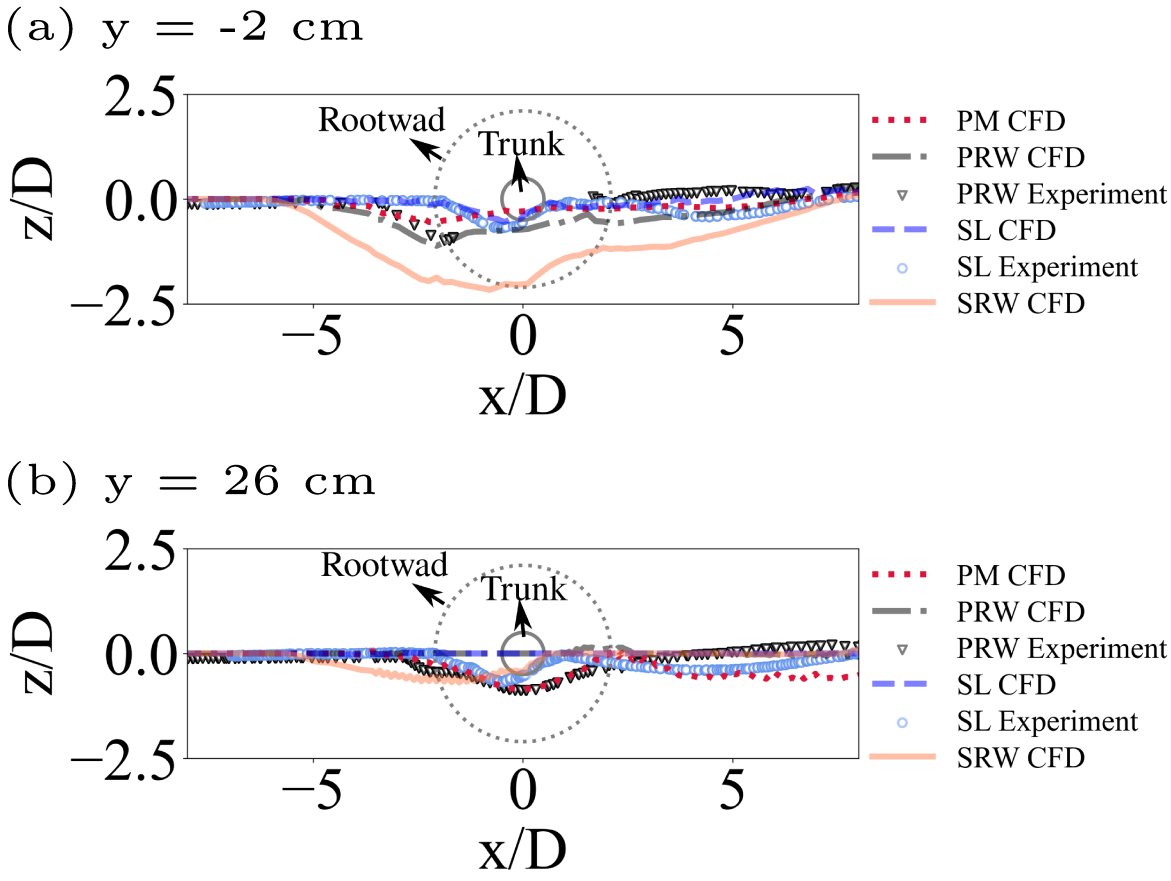

Figure 5.11. Bathymetric profiles at two representative lateral coordinates: (a) y = 26 cm, and (b) y = -2 cm.

5.3.2.4 Simulated Scour Evolution

By examining the temporal evolution of both flow and scour, we can better understand the physical processes related to large wood at different stages of bed erosion, from the initiation of sediment motion to equilibrium. The simulated scour process at three different stages of scour is shown in Figure 5.12.

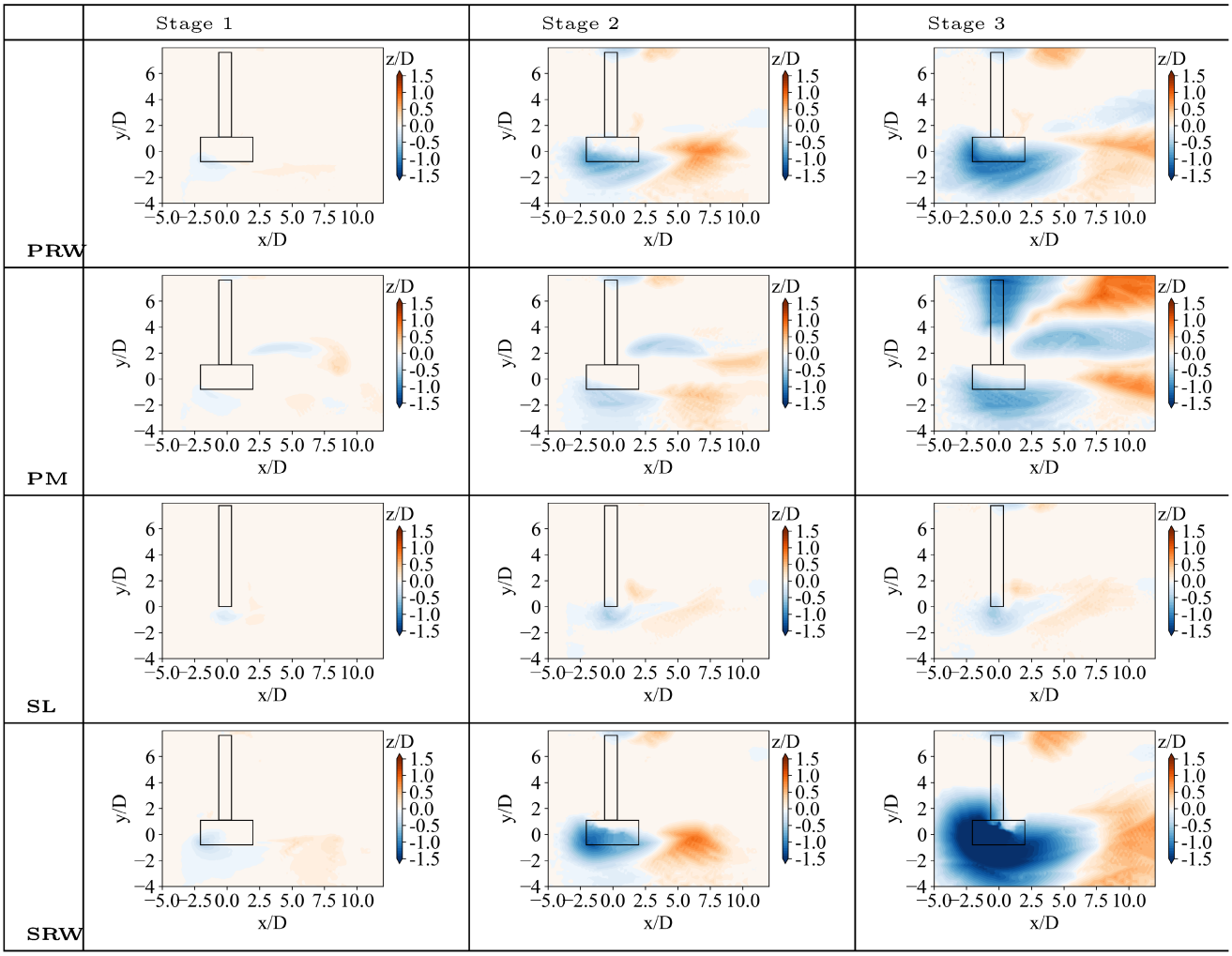

Figure 5.12. Evolution of erosion on immersed boundary

In all four cases, scour is initiated by flow contraction near the ends of the objects: the edge of the rootwad in the PRW, PM, and SRW cases, and the outer edge of the log in the SL case. In the PM case, a scour hole also begins to form at the junction of the rootwad and the trunk.

In the second stage, the scour holes from stage 1 deepen and expand. As the scour holes deepen, more eroded sediments are deposited at the trailing edge of the scour. The

shape of the scour at the ends of the rootwads and in the contraction flow region is similar for the SRW, PRW, and PM cases, although the SRW case shows deeper scour. In the SL case, the scour hole forms at the edge of the log and extends downstream, with two separated deposition bars on its sides. The laterally growing deposition bar in the SL case is similar to the one observed in the experiment. This deposition bar forms immediately behind the structure due to flow recirculation, which is interrupted by the rootwad in the other cases.

In stage 3, unlike the experiment, no scour occurred beneath the trunk in the PRW case. The main deposition bar and scour hole were captured in the contraction region, though only half of the horseshoe-shaped pattern observed in the experiment was replicated. However, the maximum scour depth was accurately captured. For the SRW case, the pattern is the same, but the maximum scour depth is overestimated. The PM case differed significantly, with a jet-like flow near the ends close to the wall, accelerating erosion beneath the trunk and around the cradles. In the PM case, two deposition bars were separated by a region of negative depth relative to the flatbed. In the PRW and SRW cases, scour did not occur beneath the structure but was driven by contraction velocity and horseshoe vortices at the structure's ends. In the SL case, the scour hole remained near the end, with deposition localized around the log. The deposition bars that were separated in stage 2 of the SL case merged in the downstream of the scour hole.

One limitation of the *ibScourFoam* model used in this work is it cannot capture the seepage flow. Seepage flow typically occurs due to a pressure difference that causes the flow to pick up a mixture of sand and water, pushing the sediment beneath the structure and forming a jet similar to those observed under pipelines Sumer et al. [2002]. Due to this limitation, the scour mechanism, even the jet-like flow under the PM case trunk is all through contraction scour.

From the simulation results, each representation of the rootwad demonstrated distinct patterns of scour and deposition as erosion progressed. The PRW case effectively captured the scour depth at the end of the structure, while the SRW case represented the same scour shape but overestimated the depth by more than 50 percent. The SL case, on the other hand, underestimated the scour depth at the ends. The PM case showed an advantage by capturing both the scour depth and a jet-like flow beneath the structure; however, it also produced an unrealistic scour depth originating from the junction of the rootwad and trunk.

Wall shear stress on the sediment bed plays a crucial role in linking flow characteristics

with scour formation. The wall shear stress at different stages of the scour process for all simulated cases is shown in Figure 5.13. The wall shear stress in these figures is nondimensionalized by the incoming wall shear stress on a flat bed. The maximum amplification of wall shear stress occurs at the ends of the structures in the contracted flow region. At the beginning of scour, the wall shear stress is amplified at the ends of the logs. This amplification extends downstream up to $x/D = 10$. In cases where the rootwad is represented, the lateral expansion of wall shear stress is more pronounced towards the free stream region. For the SL case, the wall shear stress amplification diminishes in the free stream region, which explains why erosion is negligible in this case.

In the second stage, wall shear stress at the ends and in the contraction flow region are significantly lower for the PM and SL cases. However, in the SRW and PRW cases, wall shear stress at these locations is still high. Areas with low wall shear stress, which are mostly downstream of the trunk, correspond to regions with no erosion in all cases except for the PM case. At the final third stage, amplified wall shear stress in the scour hole diminishes for the PRW and SRW cases, slowing the vertical and lateral expansion of scour. In the PM case, new region of amplified wall shear stress emerges leading to the lateral expansion of the scour and the removal of sediment from beneath the trunk. In the final stage for the PRW case, the amplified wall shear stress primarily affects eroding the downstream face of the scour hole, moving the deposition region further downstream. In the SRW case, amplified wall shear stress is still observed in the shear layer, resulting in sediment transport within the deposition area and pushing it further downstream. The SRW model tends to overestimate wall shear stress, leading to deviations from the scour patterns observed in the porous rootwad case.

The temporal evolution of scour depth S in the scour hole, sediment transport rate Q_s and the Shields number θ are shown for the four cases in Figure 5.14. In Figure 5.14 (b), the vertical axis represents the dimensionless sediment transport rate, denoted as $Q_s/(\sqrt{RgD_g}D_gB)$, where R is the relative submerged density of sediment, D_g is the characteristic sediment grain size, and B is the width of the scour, approximated as $B = (2 \cdot S_{\max} + D)/\tan(\phi)$, where ϕ is the angle of repose, $S_{\max}$ represents the maximum scour depth and D is the length scale of structure. In the SL case, the scour depth reaches equilibrium faster than in the other cases. For the PRW and SRW cases, the temporal evolution of scour depth is similar, which is reflected in both the temporal evolution of scour depth and sediment transport rate. In the PM case, the temporal evolution of scour reveals the formation of a second scour hole under the large wood, driven by accelerated flow underneath. This results in two distinct erosion phases: one leading to

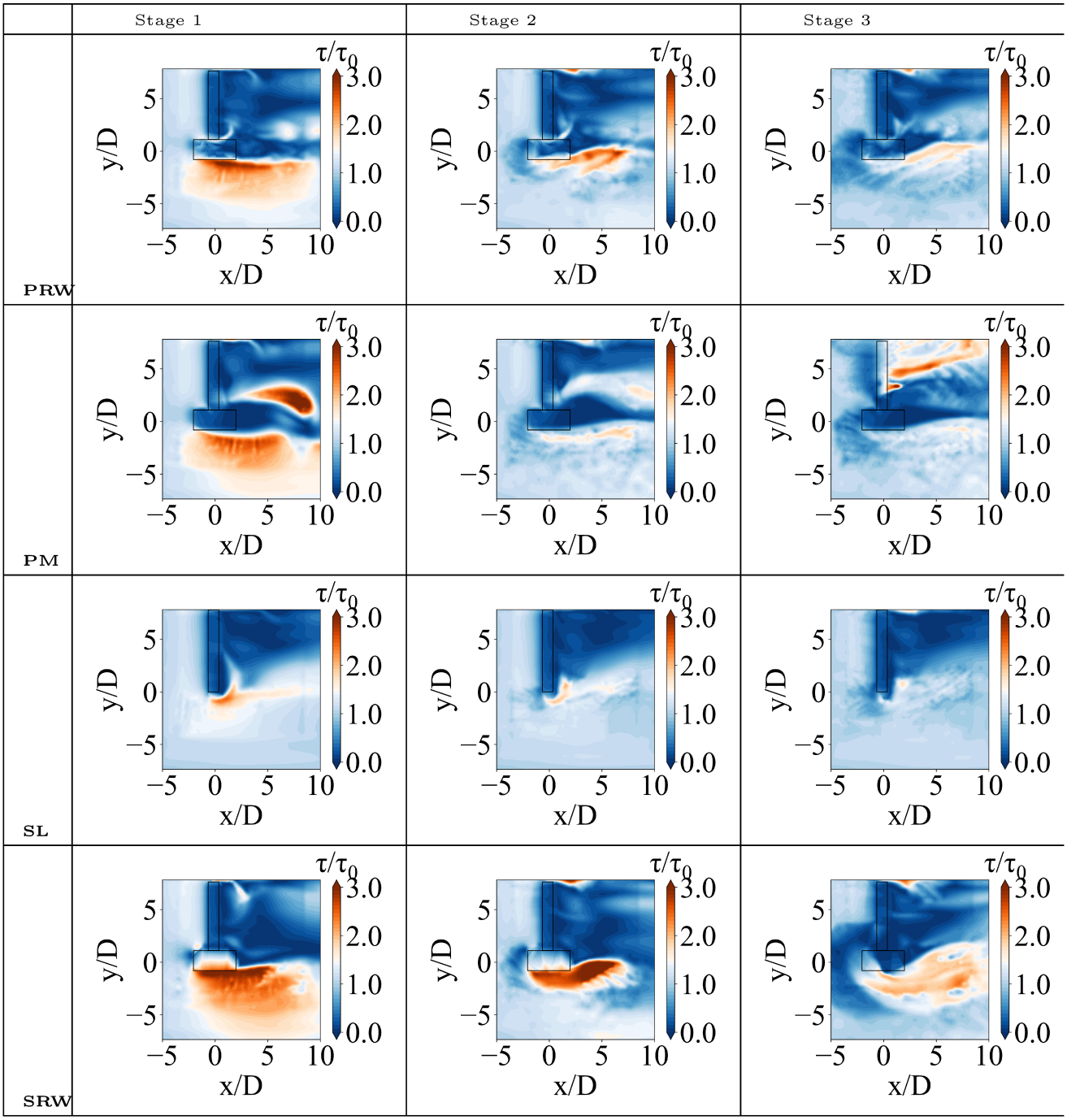

Figure 5.13. Evolution of bed shear stress.

the horse-shoe scour at the log's end, which stabilizes over time, and another forming a new scour hole away from the rootwad. This process is reflected in the simulated time history of sediment transport rate and Shields number, where an initial decline is followed by a new peak, indicating the development of the second scour hole.

In general, shear stress, i.e., the Shields number, decreases at the scour hole gets larger. Eventually, the shear stress falls below its critical value and the scour reaches equilibrium. This process is known as shear decay. Overall, shear decay is effectively captured in all cases, which is crucial for understanding scour depth formation. The evolution of the Shields number is similar in both the SRW and PRW cases, with scour depth concentrated at the log ends. However, the SRW case overestimates the scour depth, as seen in the bathymetry contours in Figure 5.12. In the SL case equilibrium depth of scour achieved faster than the cases with a rootwad.

Investigating the simulation and experimental results revealed a significant impact of adding a rootwad compared to the single log case. Even a highly porous rootwad replacing part of the solid single log led to increased contraction-induced erosion and eliminated downstream scouring due to flow separation.

The temporal evolution of morphology, along with bathymetry and shear stress contours, shows that the driving processes of erosion change as the scour deepens. Initially, flow acceleration at the log ends triggers sediment motion. As the scour deepens, horseshoe vortices intensify, driving further erosion until they reach a point where they no longer deepen the scour, indicating a shift in the scouring mechanism.

Both the porous rootwad (PRW) and single log (SL) simulations accurately captured the scour depth derived from accelerated flow. However, the porosity model (PM) was less effective in predicting this accelerated flow scour but performed well in modeling tunneling beneath the trunk. The SRW model was the least accurate overall. Therefore, results from the porosity model (PM) and the solid model (SRW) should be used with caution. For accurate results in the contraction region, the fully resolved model is preferred. However, if tunneling is the main concern, the porosity model can be more used.

5.4 Conclusions

In this study, we examined the hydrodynamics and sediment transport around large wood structures with porous rootwads. We conducted flume experiments and coupled flow-sediment transport simulations to analyze scour and deposition patterns, focusing

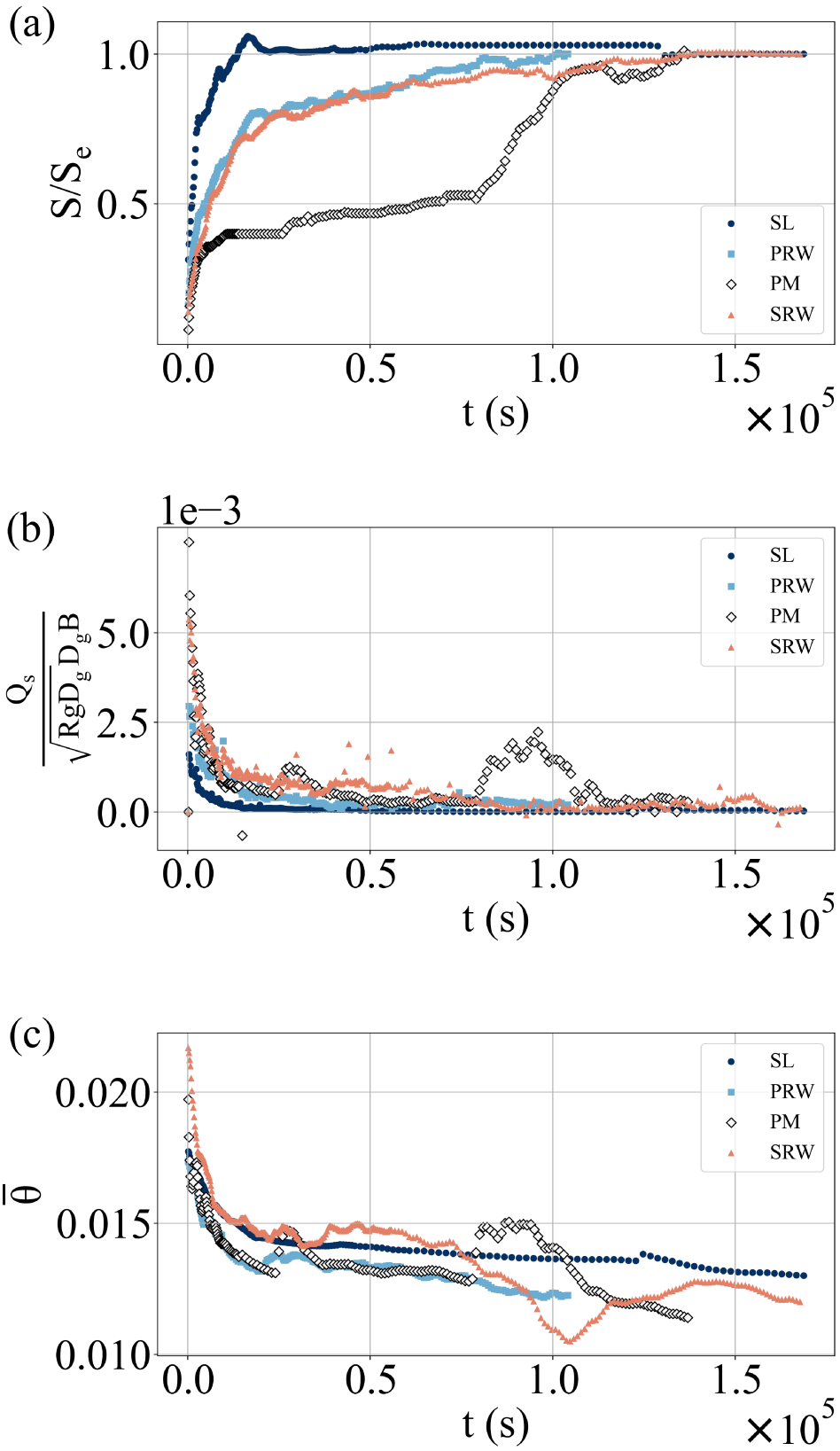

Figure 5.14. Temporal evolution of (a) scour depth, (b) sediment erosion rate, (c) average Shields number.

on the impact of different rootwad representations.

We compared large wood with porous rootwads to single logs without rootwads. We modeled rootwads using solid, fully resolved porous, and porosity model approaches. The flow results from simulations with porous rootwads matched the experimental results.

Both the SL and PRW models accurately captured the erosion observed in their respective experiments in the contraction zones near the structure's edge, where the scour was most pronounced. Both the experiments and simulations showed increased flow variability and more pronounced erosion compared to the single log case.

In the single log experiments, some sediment was deposited back onto the log, partially burying it. This phenomenon is not observed in the rootwad cases. Understanding this is crucial because the presence of large wood in the flow enhances flow variability. If the single log becomes buried in the bed, it may no longer contribute to flow variability, diminishing its ecological value and other benefits.

Key differences in flow dynamics, such as contraction velocity, wake shear layer, sweeping flow over the trunk, and bleeding flow through the structure, contributed to flow and sediment transport variations. In the single log case, the primary scour mechanisms are horseshoe vortices at the edge and downstream erosion due to sweeping flow. The presence of an emergent rootwad enhanced contraction-induced scour, while bleeding flow reduced sweeping flow circulation.

The representation of the rootwad in simulation also significantly affected the sediment transport results. The solid rootwad produced the largest scour hole, followed by the fully resolved porous rootwad, the porosity model, and finally, the single log. As the bed evolves, the driving mechanism behind scour changes. The PM model is unique in capturing the erosion and flow beneath the trunk, consistent with experimental observations. The addition of tunnelling scour alters the temporal evolution of scour. However, in the contraction region, the PRW case performed better than other models in capturing the scour depth around the porous rootwad.

Chapter 6
Summary of Contributions, Conclusions, and Future Work

6.1 Introduction

Nature-based river restoration solutions are becoming increasingly popular due to their ecological benefits and potential to promote biodiversity. Nature-based river restoration solutions, such as engineered log jams and large woody debris, are porous and have complex geometries, making them different from simplified solid structures. Due to the bleeding flow through these porous structures, flow and scour around them differ significantly from impervious, solid structures. Scour, a critical process for the stability of in-stream infrastructure such as bridge piers, can provide favorable ecological conditions in the case of nature-based solutions by influencing sediment transport patterns. Thus, a systematic investigation on critical flow characteristics that govern flow and sediment transport around porous structures is essential for the success of river restoration practices.

This research advanced the frontier of our knowledge on the physical processes associated with nature-based river restoration solutions by the means of flume experiments, computational modeling and physics-based analysis. This chapter summarizes the key findings and results of the research. Additionally, it discusses the limitations of the current work and proposes several directions for future research.

6.2 Key Findings and Results

In this work, turbulent flow and sediment transport around in-stream nature-based solutions for river restoration were investigated. Most previous research focused on

understanding turbulent flow around simple, solid geometries without considering porosity. However, porous structures introduce additional complexity due to the bleeding flow through pore spaces, which impacts the flow and sediment transport features around them. This dissertation explored these complexities.

Laboratory flume experiments with scaled restoration structures were conducted to understand both engineered in-stream restoration structures, such as ELJs and solid piers, as well as naturally formed ones, like LWDs. These experiments, along with detailed analyses of the resulting data, helped quantify the hydrodynamics and morphodynamics around these structures. The experimental results revealed fundamental differences in flow dynamics and bathymetric characteristics depending on the porosity of the structures. New concepts for evaluating the scour response of porous structures were introduced, including the consideration of both volumetric and surface porosities. This approach accounts for the flow entering the structure, as well as the intricate interaction between the flow and the varied element configurations within the structure. Equilibrium bathymetry measurements, along with available literature data, were used to provide new, modified scour estimation equations. The applicability of these equations was tested against a rare field data. A saturation growth curve was developed to model the temporal evolution of scour around porous structures. The experimental data were used to validate computational models, ensuring their correctness and accuracy.

State-of-the-art computing technology was used to resolve the complex geometries of river restoration structures and investigate the effects of porosity and geometric complexity on flow and sediment transport. The high-fidelity 3D model produced smooth wall shear stress distributions, essential for accurately capturing erosion processes around and within ELJs and LWDs with root wads. The model's accuracy enabled the development of new physical and semi-theoretical scour equations. Hence, this dissertation successfully achieved an understanding of the effect of porosity on flow velocity, coherent flow structures, and key factors driving erosion. In addition to understanding maximum scour depth, the research presented insight into the temporal evolution of erosion. Scour estimation equations that incorporate porosity were developed.

This work also highlights the significant impact of rootwads on flow patterns and bathymetry compared to simple cylindrical logs. Different representations of root wads were evaluated in coupled computations of flow and sediment transport around large woody debris (LWDs) to assess their hydraulic impact. The experiments and simulations revealed increased flow variability and more pronounced erosion in the presence of root wads compared to the single log case. The rootwad interfered with lateral sediment

deposition and burial, and the ecological implications are provided. In the single log case, primary scour mechanisms included horseshoe vortices and downstream erosion due to sweeping flow. In contrast, an emergent rootwad enhanced contraction-induced scour, while bleeding flow reduced the sweeping flow's circulation.

One of the significant findings of this research is the critical influence of rootwad representation in simulations on sediment transport results. The comparison of fully resolved porous rootwad, the porosity model, and finally, the single log in terms of capturing bathymetric features was performed. The pros and cons of each methodology were analyzed.

6.3 Conclusions

This study considered two types of nature-based structures: large woody debris and engineered log jams . The key conclusions are as follows:

- The bleeding flow through porous ELJs led to reduced contraction velocity and turbulence production, resulting in less prominent bathymetric features as porosity increased. Scour becomes more localized around structures with increased porosity, with noticeable changes in the shape of scour and deposition patterns. Existing guidelines for scour estimation of solid structures need to be updated by incorporating the correction factor equation derived in this study to accurately capture the effect of porosity. Both volumetric and surface porosities are critical for accurately estimating scour around complex porous structures, as they account for flow entering the structure and the intricate interactions with internal configurations. These insights contribute to a more precise understanding of sediment transport in porous systems.

- The successful implementation of a three-dimensional computational model enabled accurate simulation of the complex interactions between flow and sediment transport around both solid and porous hydraulic structures. The results revealed significant differences in flow dynamics and scour patterns between ELJs and solid piers, highlighting the crucial role of porosity. Through accurate simulations of flow and sediment transport around ELJs, including smooth wall shear stress distributions, the study provided physics-based equations for scour estimation. With the assumption that the scour can be approximated as a truncated inverted cone, where the base corresponds to the length scale of the structure, shear stress

and sediment transport data from the simulations were used to develop these new equations.

- The impact of rootwads in the application of LWDs was thoroughly investigated through both experiments and simulations. Results showed that the inclusion of rootwads significantly increased flow variability and intensified erosion compared to the simpler case of a single log without a rootwad. In the simulations, various representations of porous rootwads were tested, with the solid rootwad generating the largest scour hole, followed by the fully resolved porous rootwad, the porosity model, and finally, the single log. As the bed evolved, the driving mechanisms behind scour shifted, highlighting the dynamic nature of these processes. Both the PRW and PM models successfully captured the contraction mechanism contributing to scour formation, aligning with observations from PRW experiments, while the SL case also accurately reflected the counterpart experimental results.

The findings from this research can inform the design and implementation of nature-based solutions (NBS) for river restoration, ensuring greater stability and longevity of these structures.

6.4 Limitations of the Research and Future Work Opportunities

In this study, suspended sediment load was not considered, as the flume experiments were conducted in a clear-water regime where bed-load transport was the dominant mode of sediment movement. However, in real-world scenarios, suspended sediments can play a significant role in sediment transport processes. Future research could incorporate suspended sediment transport to provide a more comprehensive understanding of sediment dynamics and further enhance the capabilities of current models.

For the modeling, a rigid-lid approximation was used, as the experiments showed that water surface variations were minimal. However, this approach may not be applicable in cases with highly variable water surface changes. In such instances, improvements are needed, and a method such as Volume of Fluid (VoF) can be employed to accurately capture the free surface dynamics.

Further research could also explore field applications using two-dimensional (2D) models. In practice, 2D depth-averaged models are more feasible and cost-effective.

Currently, three-dimensional modeling is only aspirational for practitioners due to high computational cost. For 2D models, it is a common sense that their assumptions and simplifications may not be fully applicable to porous river restoration structures. A thorough evaluation of the limitations and applicability of 2D models for these scenarios would be beneficial. For example, a 3D model-informed 2D modeling approach can be explored.

Bibliography

T Abbe. Conceptual design guidelines: Application of engineered logjams, 2006.

Tim Abbe and Andrew Brooks. Geomorphic, engineering, and ecological considerations when using wood in river restoration. *Stream Restoration in Dynamic Fluvial Systems: Scientific Approaches, Analyses, and Tools*, 194:419–451, 2011.

Tim Abbe, George Pess, David R Montgomery, and Kevin L Fetherston. 17. integrating engineered log jam technology into river rehabilitation. *Restoration of Puget Sound Rivers*, 443, 2003.

Tim Abbe, Mike Hrachovec, and Steve Winter. Engineered log jams: Recent developments in their design and placement, with examples from the pacific northwest, usa. *Reference Module in Earth Systems and Environmental Sciences. Netherlands: Elsevier. https://doi. org/10.1016/B978-0-12-409548-9.11031-0, accessed August*, 7:2020, 2018.

Timothy B Abbe and David R Montgomery. Large woody debris jams, channel hydraulics and habitat formation in large rivers. *Regulated Rivers: research & management*, 12 (2-3):201–221, 1996.

Jochen Aberle and Juha Järvelä. Flow resistance of emergent rigid and flexible floodplain vegetation. *Journal of Hydraulic Research*, 51(1):33–45, 2013.

Anu Acharya. *Experimental study and numerical simulation of flow and sediment transport around a series of spur dikes*. The University of Arizona, 2011.

Stephen Addy and Mark Wilkinson. An assessment of engineered log jam structures in response to a flood event in an upland gravel-bed river. *Earth Surface Processes and Landforms*, 41(12):1658–1670, 2016.

M Sami Akoz. Investigation of vortical flow characteristics around a partially buried circular cylinder. *Ocean engineering*, 52:35–51, 2012.

Jeffrey B Allen and David L Smith. Characterizing the impact of geometric simplification on large woody debris using cfd. *International Journal of hydraulic engineering*, 1(2): 1–14, 2012.

Miriam Altmann, Davide Vanzo, Daniel Valero, and Isabella Schalko. A simple approach to simulate logjams in two-dimensional hydrodynamic models. *Journal of Hydraulic Engineering*, 150(4):06024002, 2024.

George Annandale, Steven Smith, et al. Calculation of bridge pier scour using the erodibility index method. Technical report, Golden Associates, 2001.

LA Arneson, LW Zevenbergen, PF Lagasse, PE Clopper, et al. Evaluating scour at bridges. Technical report, National Highway Institute (US), 2012a.

Lisa A. Arneson, Lori W. Zevenbergen, Peter F. Lagasse, and Paul E. Clopper. *Evaluating Scour at Bridges (HEC-18)*. Hydraulic Engineering Circular No. 18. Federal Highway Administration, Washington, D.C., 5th edition edition, 2012b.

CÜNEYT Baykal, B Mutlu Sumer, David R Fuhrman, Niels Gjøl Jacobsen, and Jørgen Fredsøe. Numerical simulation of scour and backfilling processes around a circular pile in waves. *Coastal Engineering*, 122:87–107, 2017.

AA Beheshti and Behzad Ataie-Ashtiani. Experimental study of three-dimensional flow field around a complex bridge pier. *Journal of engineering mechanics*, 136(2):143–154, 2010.

Sean J Bennett, Weiming Wu, Carlos V Alonso, and Sam SY Wang. Modeling fluvial response to in-stream woody vegetation: Implications for stream corridor restoration. *Earth Surface Processes and Landforms: The Journal of the British Geomorphological Research Group*, 33(6):890–909, 2008.

Sean J Bennett, S Mohammad Ghaneeizad, Michael S Gallisdorfer, Donghua Cai, Joseph F Atkinson, Andrew Simon, and Eddy J Langendoen. Flow, turbulence, and drag associated with engineered log jams in a fixed-bed experimental channel. *Geomorphology*, 248:172–184, 2015.

Emily S Bernhardt, Margaret A Palmer, JD Allan, G Alexander, Katie Barnas, Shane Brooks, J Carr, Stephen Clayton, Clifford Dahm, Jennifer Follstad-Shah, et al. Synthesizing us river restoration efforts, 2005.

Andrew P Brooks, Tim Abbe, T Cohen, N Marsh, S Mika, A Boulton, T Broderick, D Borg, and I Rutherfurd. *Design guideline for the reintroduction of wood into Australian streams*. Land & Water Australia Canberra, 2006.

B Brørs. Numerical modeling of flow and scour at pipelines. *Journal of hydraulic Engineering*, 125(5):511–523, 1999.

William R Brownlie. Prediction of flow depth and sediment discharge in open channels. 1981.

Benoît Camenen, Magnus Larson, and Atilla Bayram. Equivalent roughness height for plane bed under oscillatory flow. *Estuarine, Coastal and Shelf Science*, 81(3):409–422, 2009.

Marion R Carstens. Similarity laws for localized scour. *Journal of the Hydraulics Division*, 92(3):13–36, 1966.

Jacques Chabert. Etude des affouillements autour des piles de ponts. *Rep. Natl. Hydraul Lab., Chatou*, 1956.

Yunxiang Chen, Roman A DiBiase, Nicholas McCarroll, and Xiaofeng Liu. Quantifying flow resistance in mountain streams using computational fluid dynamics modeling over structure-from-motion photogrammetry-derived microtopography. *Earth Surface Processes and Landforms*, 44(10):1973–1987, 2019.

Zhengbing Chen, Alejandra Ortiz, Lijun Zong, and Heidi Nepf. The wake structure behind a porous obstruction and its implications for deposition near a finite patch of emergent vegetation. *Water Resources Research*, 48(9), 2012.

J Cherry and RL Beschta. Coarse woody debris and channel morphology: a flume study 1. *JAWRA Journal of the American Water Resources Association*, 25(5):1031–1036, 1989.

Yee Meng Chiew. *Local scour at bridge piers*. PhD thesis, ResearchSpace@ Auckland, 1984.

Sandra Clark-Kolaks. Aquatic habitat enhancement plan for the placement of natural and artificial habitats in indiana's reservoirs. *Indiana Department of Natural Resources, Indiana*, 2015.

Stephen E Coleman, Christine S Lauchlan, and Bruce W Melville. Clear-water scour development at bridge abutments. *Journal of Hydraulic Research*, 41(5):521–531, 2003.

Brian D Collins and David R Montgomery. Forest development, wood jams, and restoration of floodplain rivers in the puget lowland, washington. *Restoration Ecology*, 10(2):237–247, 2002.

Brian D Collins, David R Montgomery, and Andrew D Haas. Historical changes in the distribution and functions of large wood in puget lowland rivers. *Canadian Journal of Fisheries and Aquatic Sciences*, 59(1):66–76, 2002.

George Constantinescu, Alexander Sukhodolov, and Andrew McCoy. Mass exchange in a shallow channel flow with a series of groynes: Les study and comparison with laboratory and field experiments. *Environmental fluid mechanics*, 9:587–615, 2009.

Cathal Cummins, Ignazio Maria Viola, Enrico Mastropaolo, and Naomi Nakayama. The effect of permeability on the flow past permeable disks at low reynolds numbers. *Physics of Fluids*, 29(9):097103, 2017.

Melinda D Daniels and Bruce L Rhoads. Influence of a large woody debris obstruction on three-dimensional flow structure in a meander bend. *Geomorphology*, 51(1-3):159–173, 2003.

Simon James Dixon. A dimensionless statistical analysis of logjam form and process. *Ecohydrology*, 9(6):1117–1129, 2016.

Martin W Doyle, Doug Shields, Karin F Boyd, Peter B Skidmore, and DeWitt Dominick. Channel-forming discharge selection in river restoration design. *Journal of Hydraulic Engineering*, 133(7):831–837, 2007.

Jennifer G Duan, Li He, Xudong Fu, and Quangqian Wang. Mean flow and turbulence around experimental spur dike. *Advances in Water Resources*, 32(12):1717–1725, 2009.

Frank Engelund and Jørgen Fredsøe. A sediment transport model for straight alluvial channels. *Hydrology Research*, 7(5):293–306, 1976.

Cristian Escauriaza and Fotis Sotiropoulos. Reynolds number effects on the coherent dynamics of the turbulent horseshoe vortex system. *Flow, turbulence and combustion*, 86:231–262, 2011.

Robert Ettema, Bruce W Melville, and George Constantinescu. *Evaluation of bridge scour research: Pier scour processes and predictions*. Citeseer, 2011.

Robert Ettema, George Constantinescu, and Bruce W Melville. Flow-field complexity and design estimation of pier-scour depth: Sixty years since laursen and toch. *Journal of Hydraulic Engineering*, 143(9):03117006, 2017.

Felix M Exner. Uber die wechselwirkung zwischen wasser und geschiebe in flusen. *Sitz-Ber. Akad. Wiss. Wien*, 1925.

Vito Ferro. Adv measurements of velocity distributions in a gravel-bed flume. *Earth Surface Processes and Landforms: The Journal of the British Geomorphological Research Group*, 28(7):707–722, 2003.

Elizabeth M Follett and Heidi M Nepf. Sediment patterns near a model patch of reedy emergent vegetation. *Geomorphology*, 179:141–151, 2012.

Michael S Gallisdorfer, Sean J Bennett, Joseph F Atkinson, S Mohammad Ghaneeizad, Andrew P Brooks, Andrew Simon, and Eddy J Langendoen. Physical-scale model designs for engineered log jams in rivers. *Journal of Hydro-environment Research*, 8 (2):115–128, 2014.

Michael S Gallisdorfer, Sean J Bennett, S Mohammad Ghaneeizad, and Joseph F Atkinson. Morphodynamic responses of physical-scale experimental river channels to engineered logjams for stream restoration design. In *River Flow*, pages 2354–2359, 2016.

Carlos M García, Mariano I Cantero, Yarko Niño, and Marcelo H García. Turbulence measurements with acoustic doppler velocimeters. *Journal of Hydraulic Engineering*, 131(12):1062–1073, 2005.

Marcelo Garcia. *Sedimentation Engineering*. American Society of Civil Engineers, mop 110 edition, 2008. doi: 10.1061/9780784408148. URL `https://ascelibrary.org/doi/abs/10.1061/9780784408148`.

Derek G Goring and Vladimir I Nikora. Despiking acoustic doppler velocimeter data. *Journal of hydraulic engineering*, 128(1):117–126, 2002.

Owen T Gorman and James R Karr. Habitat structure and stream fish communities. *Ecology*, 59(3):507–515, 1978.

Mark Steven Gosselin. *The temporal variation of clear water local scour around a single circular cylinder*. University of Florida, 1997.

William L Graf. Dam age control: restoring the physical integrity of america's rivers. *Annals of the Association of American Geographers*, 91(1):1–27, 2001.

Mark E Harmon, Jerry F Franklin, Fred J Swanson, Phil Sollins, SV Gregory, JD Lattin, NH Anderson, SP Cline, NG Aumen, JR Sedell, et al. Ecology of coarse woody debris in temperate ecosystems. *Advances in ecological research*, 15:133–302, 1986.

Kimberly A Hatton, Diane L Foster, Peter Traykovski, and Heather D Smith. Numerical simulations of the flow and sediment transport regimes surrounding a short cylinder. *IEEE Journal of Oceanic Engineering*, 32(1):249–259, 2007.

Zhiguo He, Weiming Wu, and F Douglas Shields Jr. Numerical analysis of effects of large wood structures on channel morphology and fish habitat suitability in a southern us sandy creek. *Ecohydrology: Ecosystems, Land and Water Process Interactions, Ecohydrogeomorphology*, 2(3):370–380, 2009.

Julian CR Hunt, Alan A Wray, and Parviz Moin. Eddies, streams, and convergence zones in turbulent flows. *Studying turbulence using numerical simulation databases, 2. Proceedings of the 1988 summer program*, 1988.

Hassan Ismail, Yuncheng Xu, and Xiaofeng Liu. Flow and scour around idealized porous engineered log jam structures. *Journal of Hydraulic Engineering*, 147(1):04020089, 2021.

Niels G Jacobsen and Jørgen Fredsoe. Formation and development of a breaker bar under regular waves. part 2: Sediment transport and morphology. *Coastal Engineering*, 88:55–68, 2014.

Hrvoje Jasak, Aleksandar Jemcov, Zeljko Tukovic, et al. Openfoam: A c++ library for complex physics simulations. In *International workshop on coupled methods in numerical dynamics*, volume 1000, pages 1–20. IUC Dubrovnik Croatia, 2007.

Bjarne Jensen, Niels Gjøl Jacobsen, and Erik Damgaard Christensen. Investigations on the porous media equations and resistance coefficients for coastal structures. *Coastal Engineering*, 84:56–72, 2014.

Peggy A Johnson and Richard H McCuen. *A temporal, spatial pier scour model*. Number 1319. 1991.

Tswen-Chyuan Jue. Numerical analysis of vortex shedding behind a porous square cylinder. *International Journal of Numerical Methods for Heat & Fluid Flow*, 14(5): 649–663, 2004.

Pierre Y Julien. *Erosion and sedimentation*. Cambridge university press, 2010.

Seokkoo Kang and Fotis Sotiropoulos. Numerical modeling of 3d turbulent free surface flow in natural waterways. *Advances in water resources*, 40:23–36, 2012.

Seokkoo Kang and Fotis Sotiropoulos. Large-eddy simulation of three-dimensional turbulent free surface flow past a complex stream restoration structure. *Journal of Hydraulic Engineering*, 141(10):04015022, 2015a.

Seokkoo Kang and Fotis Sotiropoulos. Numerical study of flow dynamics around a stream restoration structure in a meandering channel. *Journal of Hydraulic Research*, 53(2): 178–185, 2015b.

Seokkoo Kang, Anne Lightbody, Craig Hill, and Fotis Sotiropoulos. High-resolution numerical simulation of turbulence in natural waterways. *Advances in Water Resources*, 34(1):98–113, 2011.

Seokkoo Kang, Craig Hill, and Fotis Sotiropoulos. On the turbulent flow structure around an instream structure with realistic geometry. *Water Resources Research*, 52 (10):7869–7891, 2016.

A Khosronejad, JL Kozarek, P Diplas, C Hill, R Jha, P Chatanantavet, N Heydari, and F Sotiropoulos. Simulation-based optimization of in-stream structures design: rock vanes. *Environmental Fluid Mechanics*, 18:695–738, 2018.

Ali Khosronejad, Seokkoo Kang, Iman Borazjani, and Fotis Sotiropoulos. Curvilinear immersed boundary method for simulating coupled flow and bed morphodynamic interactions due to sediment transport phenomena. *Advances in water resources*, 34 (7):829–843, 2011.

Ali Khosronejad, Seokkoo Kang, and Fotis Sotiropoulos. Experimental and computational investigation of local scour around bridge piers. *Advances in Water Resources*, 37: 73–85, 2012.

Ali Khosronejad, Jessica L Kozarek, Panayiotis Diplas, and Fotis Sotiropoulos. Simulation-based optimization of in-stream structures design: J-hook vanes. *Journal of Hydraulic Research*, 53(5):588–608, 2015.

Hyung Suk Kim, Ichiro Kimura, and Yasuyuki Shimizu. Bed morphological changes around a finite patch of vegetation. *Earth Surface Processes and Landforms*, 40(3): 375–388, 2015.

Hyung Suk Kim, Ichiro Kimura, and Yasuyuki Shimizu. Experimental investigations of scour pools around porous obstructions. *Water*, 8(11):498, 2016.

Mete Koken and George Constantinescu. Flow and turbulence structure around abutments with sloped sidewalls. *Journal of Hydraulic Engineering*, 140(7):04014031, 2014.

Mete Koken and George Constantinescu. Flow structure inside and around a rectangular array of rigid emerged cylinders located at the sidewall of an open channel. *Journal of Fluid Mechanics*, 910:A2, 2021.

J Kollmann, M Vieli, PJ Edwards, K Tockner, and JV Ward. Interactions between vegetation development and island formation in the alpine river tagliamento. *Applied Vegetation Science*, 2(1):25–36, 1999.

Umesh C Kothyari, Ram Chandra J Garde, and Kittur G Ranga Raju. Temporal variation of scour around circular bridge piers. *Journal of Hydraulic Engineering*, 118 (8):1091–1106, 1992.

Ching-Yao Lai and Desirée Tullos. Large wood structures and their effects on the flow field in mountain rivers. *River Research and Applications*, 30(4):529–539, 2014.

Yong G Lai, Xiaofeng Liu, Fabián A Bombardelli, and Yalan Song. Three-dimensional numerical modeling of local scour: A state-of-the-art review and perspective. *Journal of Hydraulic Engineering*, 148(11):03122002, 2022.

T Lazzarin, G Constantinescu, H Wu, and DP Viero. Fully developed open channel flow over clusters of freshwater mussels partially buried in a gravel bed. *Water Resources Research*, 60(8):e2023WR035594, 2024.

Pier Giuseppe Ledda, Lorenzo Siconolfi, Francesco Viola, François Gallaire, and Simone Camarri. Suppression of von kármán vortex streets past porous rectangular cylinders. *Physical review fluids*, 3(10):103901, 2018.

Albert R LeFeuvre, Hilmi D Altinbilek, and Marion R Carstens. Sediment-pickup function. *Journal of the Hydraulics Division*, 96(10):2051–2063, 1970.

F Lepori, D Palm, E Brännäs, and B Malmqvist. Does restoration of structural heterogeneity in streams enhance fish and macroinvertebrate diversity? *Ecological applications*, 15(6):2060–2071, 2005.

William L'Hommedieu, Desirée Tullos, and Julia Jones. Effects of an engineered log jam on spatial variability of the flow field across submergence depths. *River Research and Applications*, 36(3):383–397, 2020.

Jiaze Li, Nicolas Claude, Pablo Tassi, Florian Cordier, Andrés Vargas-Luna, Alessandra Crosato, and Stéphane Rodrigues. Effects of vegetation patch patterns on channel morphology: A numerical study. *Journal of Geophysical Research: Earth Surface*, 127 (5):e2021JF006529, 2022.

Dongfang Liang, Liang Cheng, and Fangjun Li. Numerical modeling of flow and scour below a pipeline in currents: Part ii. scour simulation. *Coastal engineering*, 52(1): 43–62, 2005.

Xiaofeng Liu and Marcelo H García. Three-dimensional numerical model with free water surface and mesh deformation for local sediment scour. *Journal of waterway, port, coastal, and ocean engineering*, 134(4):203–217, 2008.

Bridget Livers, Katherine B Lininger, Natalie Kramer, and Alicia Sendrowski. Porosity problems: Comparing and reviewing methods for estimating porosity and volume of wood jams in the field. *Earth Surface Processes and Landforms*, 45(13):3336–3353, 2020.

Ho Wen Lo, Mark Smith, Megan Klaar, and Clare Woulds. Potential secondary effects of in-stream wood structures installed for natural flood management: A conceptual model. *Wiley Interdisciplinary Reviews: Water*, 8(5):e1546, 2021.

RB Manners and MW Doyle. A mechanistic model of woody debris jam evolution and its application to wood-based restoration and management. *River Research and Applications*, 24(8):1104–1123, 2008.

Rebecca B Manners, MWm Doyle, and MJ Small. Structure and hydraulics of natural woody debris jams. *Water Resources Research*, 43(6), 2007.

Derek J Martin, Robert T Pavlowsky, and Carol P Harden. Reach-scale characterization of large woody debris in a low-gradient, midwestern usa river system. *Geomorphology*, 262:91–100, 2016.

Andrew McCoy, George Constantinescu, and Larry Weber. Exchange processes in a channel with two vertical emerged obstructions. *Flow, turbulence and combustion*, 77: 97–126, 2006.

Andrew McCoy, George Constantinescu, and Larry Weber. A numerical investigation of coherent structures and mass exchange processes in channel flow with two lateral submerged groynes. *Water resources research*, 43(5), 2007.

Andrew McCoy, George Constantinescu, and Larry J Weber. Numerical investigation of flow hydrodynamics in a channel with a series of groynes. *Journal of Hydraulic Engineering*, 134(2):157–172, 2008.

Bruce W Melville. *Local scour at bridge sites*. PhD thesis, researchspace@ auckland, 1975.

Bruce W Melville. Pier and abutment scour: integrated approach. *Journal of hydraulic Engineering*, 123(2):125–136, 1997.

Bruce W Melville and Yee-Meng Chiew. Time scale for local scour at bridge piers. *Journal of Hydraulic Engineering*, 125(1):59–65, 1999.

Bruce W Melville and Stephen E Coleman. *Bridge scour*. Water Resources Publication, 2000.

Bruce W Melville and DM Dongol. Bridge pier scour with debris accumulation. *Journal of Hydraulic Engineering*, 118(9):1306–1310, 1992.

Bruce W Melville and Arved J Raudkivi. Flow characteristics in local scour at bridge piers. *Journal of Hydraulic Research*, 15(4):373–380, 1977.

Peter Menzel, Tom Rückborn, and Alfred Leder. Flow and scour around cylindrical objects in laboratory experiments. In *2013 MTS/IEEE OCEANS-Bergen*, pages 1–8. IEEE, 2013.

Adam Thomas Merook. Laboratory assessment of scour evolution around engineered logjams in gravel bed rivers. Master's thesis, University of Tennessee, Knoxville, TN, 2018. URL `https://trace.tennessee.edu/utk_gradthes/5071`.

Helen E Morrison and Alfred Leder. Sediment transport in turbulent flows with the lattice boltzmann method. *Computers & Fluids*, 172:340–351, 2018.

Azadeh Mousavi Darzikolaei, Juanna Crowe Curran, and Xiaofeng Liu. flow and sediment transport around porous engineered log jams: An experimental study. *Journal of Hydraulic Engineering*, 2024.

Valentine Muhawenimana, Catherine AME Wilson, Jelena Nefjodova, and Jo Cable. Flood attenuation hydraulics of channel-spanning leaky barriers. *Journal of Hydrology*, 596:125731, 2021.

S Müller, EM Follett, P Ouro, and CAME Wilson. Influence of channel-spanning engineered logjam structures on channel hydrodynamics. *Water Resources Research*, 58(12):e2022WR032111, 2022.

Stephanie Müller, Catherine AME Wilson, Pablo Ouro, and Joanne Cable. Experimental investigation of physical leaky barrier design implications on juvenile rainbow trout (oncorhynchus mykiss) movement. *Water Resources Research*, 57(8):e2021WR030111, 2021.

Heidi M. Nepf. Flow and transport in regions with aquatic vegetation. *Annual Review of Fluid Mechanics*, 44(1):123–142, 2012. doi: 10.1146/annurev-fluid-120710-101048. URL `https://doi.org/10.1146/annurev-fluid-120710-101048`.

Vladimir I Nikora and Derek G Goring. Adv measurements of turbulence: Can we improve their interpretation? *Journal of hydraulic engineering*, 124(6):630–634, 1998.

Andrew Norris, Michael Hutchison, David Nixon, Jenny Shiau, and Andrew Kaus. Fish attractors in impoundment fisheries: A best practice guideline. *State of Queensland*, 2021.

Giuseppe Oliveto and Willi H Hager. Temporal evolution of clear-water pier and abutment scour. *Journal of Hydraulic Engineering*, 128(9):811–820, 2002.

Nils RB Olsen and Hilde M Kjellesvig. Three-dimensional numerical flow modeling for estimation of maximum local scour depth. *Journal of Hydraulic Research*, 36(4): 579–590, 1998.

OpenFOAM OpenCFD. The open source computational fluid dynamics (cfd) toolbox, 2014.

OpenFOAM Foundation. *OpenFOAM v5 User Guide*. OpenFOAM Foundation, 2018. `https://cfd.direct/openfoam/user-guide`.

Stefano Pagliara, Leila Hassanabadi, and Sahameddin Mahmoudi Kurdistani. Clear water scour downstream of log deflectors in horizontal channels. *Journal of Irrigation and Drainage Engineering*, 141(9):04015007, 2015a.

Stefano Pagliara, Leila Sagvand Hassanabadi, and Sahameddin Mahmoudi Kurdistani. Log-vane scour in clear water condition. *River Research and Applications*, 31(9): 1176–1182, 2015b.

Margaret A Palmer, Holly L Menninger, and Emily Bernhardt. River restoration, habitat heterogeneity and biodiversity: a failure of theory or practice? *Freshwater biology*, 55: 205–222, 2010.

AN Papanicolaou, P Diplas, CL Dancey, and M Balakrishnan. Surface roughness effects in near-bed turbulence: Implications to sediment entrainment. *Journal of Engineering Mechanics*, 127(3):211–218, 2001.

Gary Parker, Carlos M Toro-Escobar, Michael Ramey, and Stuart Beck. Effect of flood-water extraction on mountain stream morphology. *Journal of Hydraulic Engineering*, 129(11):885–895, 2003.

Diego Ravazzolo, Gabriel Spreitzer, J Tunnicliffe, and Heide Friedrich. The effect of large wood accumulations with rootwads on local geomorphic changes. *Water Resources Research*, page e2021WR031403, 2022.

P Reichl, Kerry Hourigan, and Mark Christopher Thompson. Flow past a cylinder close to a free surface. *Journal of Fluid Mechanics*, 533:269–296, 2005.

Everett V Richardson and Peter F Lagasse. *Stream stability and scour at highway bridges*. ASCE Publications, 1999.

JR Richardson and EV Richardson. Bridge scour evaluation. In *Sedimentation engineering: Processes, measurements, modeling, and practice*, pages 505–542. 2008.

Joshua J Roering, James W Kirchner, and William E Dietrich. Evidence for nonlinear, diffusive sediment transport on hillslopes and implications for landscape morphology. *Water Resources Research*, 35(3):853–870, 1999.

A Roulund, B Mutlu Sumer, J Fredsoe, and Jess Michelsen. 3-d numerical modeling of flow and scour around a pile. In *Proc. First Intl Conf. on Scour of Foundations*, pages 17–20, 2002.

Andreas Roulund, B Mutlu Sumer, Jørgen Fredsøe, and Jess Michelsen. Numerical and experimental investigation of flow and scour around a circular pile. *Journal of Fluid mechanics*, 534:351–401, 2005.

Isabella Schalko and Heidi M Nepf. Enhanced flow variability and morphological changes through individual wood placements on a gravel bed. *Geomorphology*, 453:109135, 2024.

Isabella Schalko, Carmen Lageder, Lukas Schmocker, Volker Weitbrecht, and RM Boes. Laboratory flume experiments on the formation of spanwise large wood accumulations: Part ii—effect on local scour. *Water Resources Research*, 55(6):4871–4885, 2019a.

Isabella Schalko, Carmen Lageder, Lukas Schmocker, Volker Weitbrecht, and Robert M Boes. Laboratory flume experiments on the formation of spanwise large wood accumulations: I. effect on backwater rise. *Water Resources Research*, 55(6):4854–4870, 2019b.

Isabella Schalko, Virginia Ruiz-Villanueva, Fiona Maager, and Volker Weitbrecht. Wood retention at inclined bar screens: Effect of wood characteristics on backwater rise and bedload transport. *Water*, 13(16):2231, 2021a.

Isabella Schalko, Ellen Wohl, and Heidi M Nepf. Flow and wake characteristics associated with large wood to inform river restoration. *Scientific reports*, 11(1):1–12, 2021b.

Haoyin Shan, James R Pagenkopf, Chen Li, Nasi Zhang, Daniel Pastrich, Otto Wiblishauser, Chao Huang, Kornel Kerenyi, et al. Nextscour case study: The lafayette avenue bridge over the saginaw river in bay city, michigan. Technical report, United States. Federal Highway Administration. Office of Research . . . , 2023.

Hsieh Wen Shen, Yoshiaki Agawa, and Susumu S Karaki. Time variation of bed deformation near bridge piers. 1965.

Albert Shields. Anwendung der aehnlichkeitsmechanik und der turbulenzforschung auf die geschiebebewegung. *PhD Thesis Technical University Berlin*, 1936.

Fletcher Douglas Shields Jr and Nelson R. Nunnally. Environmental aspects of clearing and snagging. *Journal of Environmental Engineering*, 110(1):152–165, 1984.

David L Smith, Jeffrey B Allen, Owen Eslinger, Miguel Valenciano, John Nestler, and R Andrew Goodwin. Hydraulic modeling of large roughness elements with computational fluid dynamics for improved realism in stream restoration planning. *Stream Restoration in Dynamic Fluvial Systems: Scientific Approaches, Analyses, and Tools*, 194:115–122, 2011.

Steven P Smith and George W Annandale. Scour in erodible rock ii: Erosive power at bridge piers. In *North American Water and Environment Congress & Destructive Water*, pages 1349–1357. ASCE, 1997.

Yalan Song, Yuncheng Xu, and Xiaofeng Liu. Physically based sand slide method in scour models based on slope-limited diffusion. *Journal of Hydraulic Engineering*, 146 (11):04020074, 2020.

Yalan Song, Seyedeh Azadeh Mousavi Darzikolaei, and Xiaofeng Liu. Scour and burial of underwater unexploded ordinances (uxos): An experimental and computational investigation. *Ocean Engineering*, 258, 2022a.

Yalan Song, Yuncheng Xu, Hassan Ismail, and Xiaofeng Liu. Scour modeling based on immersed boundary method: A pathway to practical use of three-dimensional scour models. *Coastal Engineering*, 171:104037, 2022b.

Yalan Song, Yuncheng Xu, Hassan Ismail, and Xiaofeng Liu. Scour modeling based on immersed boundary method: A pathway to practical use of three-dimensional scour models. *Coastal Engineering*, 171:104037, 2022c.

Philippe Spalart and Steven Allmaras. A one-equation turbulence model for aerodynamic flows. In *30th aerospace sciences meeting and exhibit*, page 439, 1992.

Gabriel Spreitzer, Jon Tunnicliffe, and Heide Friedrich. Large wood (lw) 3d accumulation mapping and assessment using structure from motion photogrammetry in the laboratory. *Journal of Hydrology*, 581:124430, 2020a.

Gabriel Spreitzer, Jon Tunnicliffe, and Heide Friedrich. Porosity and volume assessments of large wood (lw) accumulations. *Geomorphology*, 358:107122, 2020b.

Gabriel Spreitzer, Jon Tunnicliffe, and Heide Friedrich. Effects of large wood (lw) blockage on bedload connectivity in the presence of a hydraulic structure. *Ecological Engineering*, 161:106156, 2021.

Oscar Suaznabar, Zhaoding Xie, Roger T Kilgore, Sven Leon, Daniel Pastrich, Christoph Zuelow, Chao Huang, Kornel Kerenyi, et al. Applying engineered logjams and dolosse for streambank stabilization. Technical report, United States. Federal Highway Administration. Office of Infrastructure . . . , 2021.

B Mutlu Sumer, Christoffer Truelsen, T Sichmann, and Jørgen Fredsøe. Onset of scour below pipelines and self-burial. *Coastal engineering*, 42(4):313–335, 2001.

B Mutlu Sumer et al. *The mechanics of scour in the marine environment*. World Scientific, 2002.

NIT Nooksack Indian Tribe. South Fork Nooksack Hutchinson Reach Restoration Phase 1. `https://srp.rco.wa.gov/project/360/17986`, 2015. Accessed: 2022-16-7.

Frank J Triska. Role of wood debris in modifying channel geomorphology and riparian areas of a large lowland river under pristine conditions: A historical case study: With 7 figures and 4 tables in the text. *Internationale Vereinigung für theoretische und angewandte Limnologie: Verhandlungen*, 22(3):1876–1892, 1984.

Desirée Tullos and Cara Walter. Fish use of turbulence around wood in winter: physical experiments on hydraulic variability and habitat selection by juvenile coho salmon, oncorhynchus kisutch. *Environmental biology of fishes*, 98:1339–1353, 2015.

USBR and ERDC. National large wood manual: Assessment, planning, design, and maintenance of large wood in fluvial ecosystems: Restoring process, function, and structure. 2016.

USBR, ERDC (Bureau of Reclamation, US Army Engineer Research, and Development Center). National large wood manual: Assessment, planning, design, and maintenance of large wood in fluvial ecosystems: restoring process, function, and structure. 2016.

Marcel Roland Alexander Van Gent. Wave interaction with permeable coastal structures. In *International Journal of Rock Mechanics and Mining Sciences and Geomechanics Abstracts*, volume 6, page 277A, 1996.

Leo C Van Rijn. Sediment pick-up functions. *Journal of Hydraulic engineering*, 110(10): 1494–1502, 1984.

Arthur Clifford Veatch. *Geology and underground water resources of northern Louisiana and southern Arkansas*. US Government Printing Office, 1906.

Pauli Virtanen, Ralf Gommers, Travis E Oliphant, Matt Haberland, Tyler Reddy, David Cournapeau, Evgeni Burovski, Pearu Peterson, Warren Weckesser, Jonathan Bright, et al. Scipy 1.0: fundamental algorithms for scientific computing in python. *Nature methods*, 17(3):261–272, 2020.

Peter M. Vitousek, Harold A. Mooney, Jane Lubchenco, and Jerry M. Melillo. Human domination of earth's ecosystems. *Science*, 277(5325):494–499, 1997.

Terry Waddle. Phabsim for windows user's manual and exercises. Technical report, US Geological Survey, 2001.

Nicholas P Wallerstein, Carlos V Alonso, Sean J Bennett, and Colin R Thorne. Distorted froude-scaled flume analysis of large woody debris. *Earth Surface Processes and Landforms: The Journal of the British Geomorphological Research Group*, 26(12): 1265–1283, 2001.

Chen Wang, Xiong Yu, and Fayun Liang. A review of bridge scour: mechanism, estimation, monitoring and countermeasures. *Natural Hazards*, 87:1881–1906, 2017.

Kevin A Waters and Joanna Crowe Curran. Effects of an emergent vegetation patch on channel reach bathymetry and stability during repeated unsteady flows. *Water Resources Research*, 52(11):9066–9085, 2016.

Andrew C Wilcox, Jonathan M Nelson, and Ellen E Wohl. Flow resistance dynamics in step-pool channels: 2. partitioning between grain, spill, and woody debris resistance. *Water Resources Research*, 42(5), 2006.

David C Wilcox. Formulation of the kw turbulence model revisited. *AIAA journal*, 46 (11):2823–2838, 2008.

David C Wilcox et al. *Turbulence modeling for CFD*, volume 2. DCW industries La Canada, CA, 1998.

Roy H Wilkens and Michael D Richardson. Mine burial prediction: A short history and introduction. *IEEE Journal of Oceanic Engineering*, 32(1):3–9, 2007.

Ellen Wohl, Natalie Kramer, Virginia Ruiz-Villanueva, Daniel N. Scott, Francesco Comiti, Angela M. Gurnell, Herve Piegay, Katherine B. Lininger, Kristin L. Jaeger, David M. Walters, et al. The natural wood regime in rivers. *BioScience*, 69(4):259–273, 2019.

Yuncheng Xu and Xiaofeng Liu. Effects of different in-stream structure representations in computational fluid dynamics models—taking engineered log jams (elj) as an example. *Water*, 9(2):110, 2017.

Oral Yagci, Isilsu Yildirim, Mehmet Furkan Celik, Vasileios Kitsikoudis, Zaide Duran, and VS Ozgur Kirca. Clear water scour around a finite array of cylinders. *Applied Ocean Research*, 68:114–129, 2017.

Fan Yang, Lili Qu, Guoqiang Tang, and Lin Lu. Local scour around a porous surface-piercing square monopile in steady current. *Ocean Engineering*, 223:108716, 2021.

Yifan Yang, Bruce W Melville, Graham H Macky, and Asaad Y Shamseldin. Temporal evolution of clear-water local scour at aligned and skewed complex bridge piers. *Journal of Hydraulic Engineering*, 146(4):04020026, 2020.

A Melih Yanmaz and H Do g ˘ an Altinbilek. Study of time-depenbent local scour around bridge piers. *Journal of Hydraulic Engineering*, 117(10):1247–1268, 1991.

Yi-Xuan Zeng, Hassan Ismail, and Xiaofeng Liu. Flow decomposition method based on computational fluid dynamics for rock weir head-discharge relationship. *Journal of Irrigation and Drainage Engineering*, 147(8):04021030, 2021.

Nuosha Zhang, Ian Rutherfurd, and Marco Ghisalberti. Effect of instream logs on bank erosion potential: a flume study with a single log. *Journal of Ecohydraulics*, 5(1):43–56, 2020a.

Nuosha Zhang, Ian Rutherfurd, and Marco Ghisalberti. Effect of instream logs on bank erosion potential: a flume study with a single log. *Journal of Ecohydraulics*, 5(1):43–56, 2020b.

Nuosha Zhang, ID Rutherfurd, and Marco Ghisalberti. The effect of instream logs on bank erosion potential: a flume study with multiple logs. *Journal of Ecohydraulics*, 5 (1):57–70, 2020c.

Kang Zhou, Jennifer G Duan, and Fabián A Bombardelli. Experimental and theoretical study of local scour around three-pier group. *Journal of Hydraulic Engineering*, 146 (10):04020069, 2020.

Lijun Zong and Heidi Nepf. Vortex development behind a finite porous obstruction in a channel. *Journal of Fluid Mechanics*, 691:368–391, 2012.

Vita

Seyedeh Azadeh Mousavi Darzikolaei

Azadeh Mousavi Darzikolaei is a PhD candidate in Civil Engineering at Penn State University, specializing in hydraulic modeling and nature-based solutions for river restoration. Born in Sari, Iran, her passion for hydraulics was deeply influenced by her childhood experiences near the Caspian Sea and Tajan River. Azadeh holds a Master's degree in Water and Hydraulic Structures Engineering from Sharif University of Technology, where she studied environmental fluid mechanics and flow around vegetation. Her PhD research, funded by U.S. National Science Foundation, focuses on the hydrodynamics and sediment transport around large woody debris, with a particular emphasis on the effects of porosity and shape complexity on flow and turbulence.

Education

- 2020-2024 PhD (Major) — Pennsylvania State University, USA
  Civil Engineering
- 2020-2024 PhD (Minor) — Pennsylvania State University, USA
  Computational Science
- 2016-2019 MSc — Sharif University of Technology, Iran
  Hydraulic Engineering
- 2011-2015 BSc — Babol Noshirvani University of Technology, Iran
  Civil Engineering